High Performance Germanium-based Anode Materials for Lithium-ion and Sodium-ion Rechargeable Batteries

by

Behdokht Farbod

A thesis submitted in partial fulfillment of the requirements for the degree of

Master of Science

in

Materials Engineering

Department of Chemical and Materials Engineering
University of Alberta

Abstract

In this thesis the electrochemical performance of germanium nanowires (GeNWs) as anode for lithium-ion batteries (LIBs) and tin-germanium-antimony (Sn-Ge-Sb) thin films as anode for sodium-ion batteries (NIBs) have been investigated.

Scientific literature shows a substantial study-to-study variation in the electrochemical lithiation performance of "1-D" nanomaterials such as Si and Ge nanowires or nanotubes. In chapter 2 of this thesis, we varied the vapor-liquid-solid (VLS) growth temperature and time, resulting in nanowire arrays with distinct mass loadings, mean diameters and lengths, and thicknesses of the parasitic Ge films that are formed at the base of the array during growth. When all the results were compared, a key empirical trend to emerge was that increasing active material mass loading drastically degraded the electrochemical performance. For instance, GeNWs grown for 2 minutes at 320 °C (0.12 mg cm^{-2} mass loading, 34 nm mean nanowire diameter, 170 nm parasitic film thickness) had a reversible capacity of 1405 mAh g^{-1}, a cycle 50 coulombic efficiency (CE) of 99.9%, a cycle 100 capacity retention of 98%, and delivered ~ 1200 mAh g^{-1} at 5C. To contrast, electrodes grown for 10 minutes at 360°C (0.86 mg cm^{-2}, 115 nm, 1410 nm) retained merely 5.6% of their initial capacity after 100 cycles, had a CE of 96%, and delivered ~ 400 mAh g^{-1} at 5C. Using TOF-SIMS we are the first to demonstrate marked segregation of Li to the current collector interface in planar Ge films that are 300 and 500 nm thick, but not in the 150 nm specimens. FIB analysis shows that the cycled higher mass loaded electrodes develop more SEI and interfacial cracks near the current collector. A comparison with the state-of-the-art scientific literature for a range of Ge - based nanostructures shows that our low mass loaded

GeNWs are highly favorable in terms of the reversible capacity at cycle 1 and cycle 100, steady-state cycling CE and high-rate capability.

Chapter 3 provides the first report on several compositions of ternary Sn-Ge-Sb thin film alloys for application as sodium ion battery (aka NIB, NaB or SIB) anodes, employing Sn50Ge50, Sb50Ge50 and pure Sn, Ge, Sb as baselines. Sn33Ge33Sb33, Sn50Ge25Sb25, Sn60Ge20Sb20 and Sn50Ge50 all demonstrate promising electrochemical behavior, with Sn50Ge25Sb25 being the best overall. This alloy has an initial reversible specific capacity of 833 $mAhg^{-1}$ (at 85 mAg^{-1}), and 662 $mAhg^{-1}$ after 50 charge - discharge cycles. Sn50Ge25Sb25 also shows excellent rate capability, displaying a stable capacity of 381 $mAhg^{-1}$ at a current density of 8500 mAg^{-1} (~ 10C). A survey of published literature indicates that 833 $mAhg^{-1}$ is among the highest reversible capacities reported for a Sn-based NIB anode, while 381 $mAhg^{-1}$ represents the most optimum fast charge value. HRTEM shows that Sn50Ge25Sb25 is a composite of 10 - 15 nm Sn and Sn-alloyed Ge nanocrystallites that are densely dispersed within an amorphous matrix that also contains localized "buffering" nanoporosity. Comparing the microstructures of alloys where the capacity significantly exceeds the rule of mixtures prediction to those where it does not, leads us to hypothesize that this new phenomena originates from the Ge(Sn) that is able to sodiate beyond the 1:1 Na:Ge ratio reported for the pure element. Combined TOF-SIMS, EELS TEM and FIB analysis demonstrates substantial Na segregation within the film near the current collector interface that is present as early as the second discharge, followed by cycling - induced delamination from the current collector.

Keywords: Ge, nanowire, thin film, Li segregation, SEI, TEM, FIB, TOF-SIMS, sodium ion battery NIB NaB SIB, lithium ion battery LIB, anode, Sn, Sb, Ge, thin film

Preface

Chapter 2 of this thesis has been submitted to Journal of Materials Chemistry A on 20 May 2014, as Farbod B., Cui K., Kupsta M., Kalisvaart W. P., Memarzadeh E., Kohandehghan A., Zahiri B., and Mitlin D. "Array Geometry Dictates Electrochemical Performance of Ge Nanowire Lithium Ion Battery Anodes", Manuscript ID: TA-ART-07-2014-003805.

Chapter 3 of this thesis has been published as Farbod B., Cui K., Kalisvaart P., Kupsta M., Zahiri B., Kohandehghan A., Memarzadeh E., Li Z., Luber E. J., and Mitlin D., "Anodes for Sodium Ion Batteries based on Tin - Germanium - Antimony Alloys", ACS Nano, 2014, 8, 4415–4429.

I was responsible for the data collection, integration, and analysis, and also the manuscript composition. Prof. David Mitlin was the supervisory author and was involved with concept formation and manuscript composition.

Dedication

I dedicate this thesis to the ones who mean the world to me:

To my mom and dad, who taught me to trust in god, believe in hard work, and never give up;

To my lovely sisters, my kind brothers, my beautiful niece, and my wonderful friends;

To my love, Arash, for being a friend, a loving husband, and a real supporter to me. Love you and thanks for being in my life and for making me happy.

Acknowledgement

This work could not be accomplished without help of others. I would like to thank my supervisor, Prof. David Mitlin, for giving me the valuable opportunity of working with him as a graduate student. I truly appreciate his deep knowledge, his friendly supports and his great guidance during my research. I would also like to thank everyone in Mitlin Group for their unconditional help and friendship; Many thanks to Peter Kalisvaart, Elmira Memarzadeh, Tyler Stephenson, Chris Holt, Zhi Li, Xuehai Tan, Brian Olsen, Beniamin Zahiri, and Alireza Kohandehghan.

I would like to thank all technicians and staff members of the Chemical and Materials Engineering Department, National Institute for Nanotechnology, National Research Council, Science Centennial Centre for Interdisciplinary Science, and Cross-Cancer Institute at University of Alberta; Special thanks to Mrs. Lily Laser, the Graduate Administrative Assistant, who was always there for all of graduate students. Her unconditional help and kindness would never be forgotten; Special thanks to Martin Kupsta, Technical Officer at National Research Council, for his friendly support and assistance. I wish him success in his life and career.

I also thank all of my other friends for their ethereal support, and my family for giving me all the support I needed.

Table of Contents

List of Tables

List of Figures

1. Introduction

Energy is the lifeblood of modern society. Global warming, finite fossil-fuel supplies and city pollution arouse the need of renewable energy and electric transportation. There is a prompt need to design electrical energy storage systems to balance supply with demands and to use the plug-in hybrid electric vehicles or electric vehicles. Numerous energy storage solutions such as mechanical, magnetic, chemical storage, etc., are being recently investigated. Therefore, as we want to store energy in order to restore it as electricity, the most attractive path is to convert chemical energy into electrical energy, as they both share a common carrier, namely the electron. Batteries are electrochemical storage devices that ensure such conversions to occur in a reversible way, respectively. For this purpose, lithium- ion batteries (LIBs) can be significantly important. [1-6] Due to their high energy density and long cycle life, LIBs have been extensively used in portable electronic devices such as computers, tablets, cell-phones, and etc. However, they still suffer from some problems which need to be overcome in order to be used broadly and practically in stationary energy storage and electric vehicles. [2,3,6-8] For instance, the energy density and the driving range they provide cannot compete with liquid fuels yet. [9] Thus, increasing energy and power densities, improving safety, and lowering the cost of ion batteries is highly required. [2,8,10]

1.1. Batteries

Typically batteries need a driving force to accept electrons or to give them away between two electrodes. This driving force is usually the difference in oxidation or reduction potentials. These electrodes have metallic current collectors to let the electrons flow from the external circuit to the electrodes. This flow results in the generation of a useful work, which could be power of a portable device such as a cellular phone or an electric vehicle. An ionically conducting and electronically insulating electrolyte is used in batteries to physically and electronically separate these two electrodes. To separate them mechanically and also to prevent short-circuits, a separator, usually a piece of glass, cellulose, or polymer fibers is used. The electrode with stronger reducing potential gives electrons away and becomes oxidized and is called the negative electrode (anode). Lithium as the strongest reductant on the periodic table has a standard reduction potential of -3.04 V. Positive electrode (cathode), on the other hand, is the electrode which accepts the electrons from the negative electrode and becomes reduced. [11]

During discharge, negative electrode oxidizes and at the same time positive electrode reduces. The oxidation and reduction processes are accompanied by giving up and accepting electrons, respectively. This electron transfer process will continue until the potential difference between cathode and anode becomes too low. At this point, the cell is fully discharged. [12,13] The change from electronic current to ionic current occurs at the electrode/electrolyte interface and is controlled by Faraday's Law, the relationship between the equivalent quantities of chemical reactants and electrical charge.

Batteries mainly come in two types: primary batteries (non-rechargeable batteries) and secondary batteries (rechargeable batteries). In rechargeable batteries, an opposite current is

applied and electrons are pumped from the positive to the negative electrode to raise the potential difference for further discharge. This process is known as charging step. During charging, the positive active material is oxidized therefore produces electrons and then electrons are taken to the negative electrode and finally the negative active material will be reduced. In fact, oxidation and reduction occurs in the positive and negative sides of battery during charging, respectively, and vice versa upon discharging. While redox reactions take place and electrons travel through the external circuit between negative and positive sides, to balance the battery electronically, cations transfer between electrodes inside the electrolyte as well. [14]

Due to their high gravimetric, volumetric energy densities and design flexibility, Li-based batteries are the dominant type of secondary batteries amongst the various existing technologies. [13] Owing to the light-weight lithium containing compounds and a non-aqueous electrolyte these batteries can be lighter with less taken space and also a larger voltage range can be used between two electrodes. The energy density is related to this voltage range and a large voltage will yield a higher energy density. In addition, these batteries can recharge more quickly than other types of batteries, because of their superior power densities. [15,16]

1.1.1. Lithium-ion Batteries

Lithium batteries are characterized by the transfer of Li ions and electrons in order to balance the charge. Most of the commercial rechargeable LIBs are based on graphite, in which LiC_6 will be formed after fully lithiation and will result in a maximum theoretical specific capacity of 372 mAh/g. [17,18] Upon graphite reduction during charging step, Li intercalation into

carbon structure takes place when ions insert between graphene sheets and an intercalated compound is formed. Once it occurs, Li^+ de-intercalate from the graphite host structure and dissolve into the electrolyte. [19] Figure 1.1 illustrates schematic of processes happening during charge and discharge in a typical Li-ion battery with graphite anode and a lithium metal oxide ($Li_{1-x}CoO_2$) cathode.

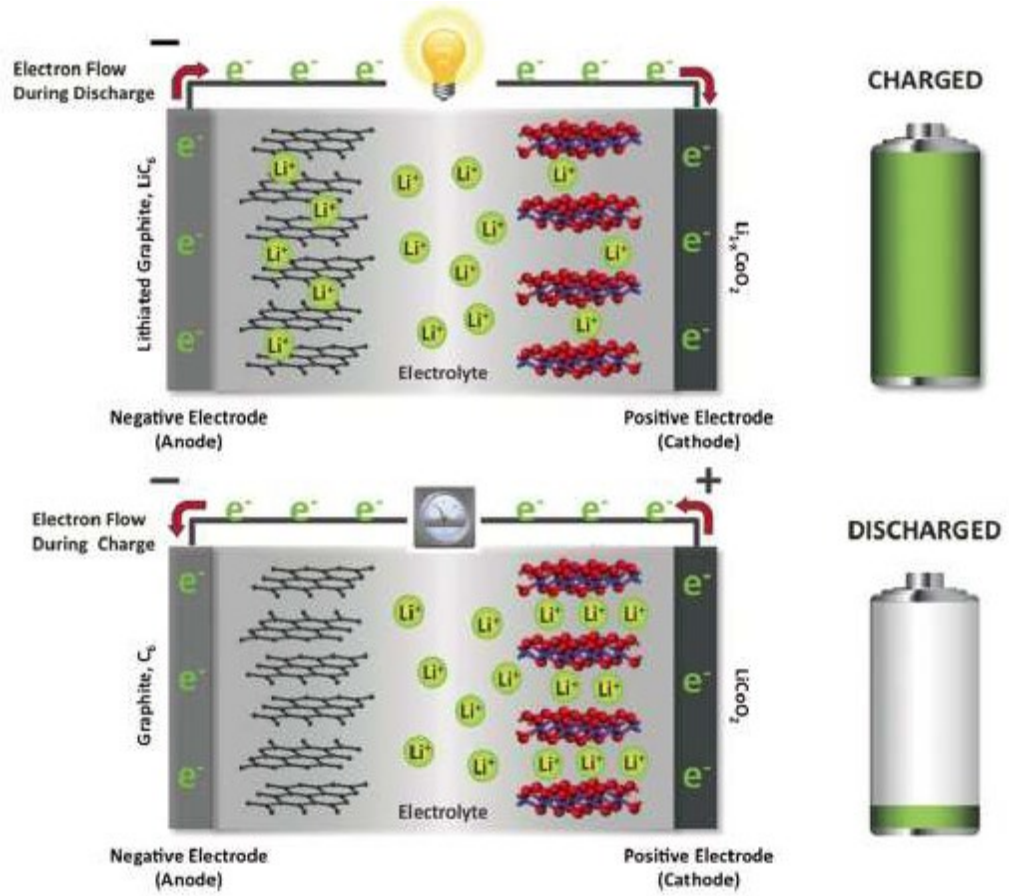

Figure 1.1. Schematic demonstration of electrons and Li^+ transfers during charge and discharge steps. [19]

1.1.1.1. Important parameters for evaluating battery electrode materials

I. Voltage

In Li-ion batteries, the voltage of a battery is equivalent to the difference in lithium's chemical potential in each electrode. At cell's open circuit state, in which cell is not discharged yet, the voltage between two electrodes equals to:

$$V_{oc} = \frac{-[\mu_{Li}^{(+)} - \mu_{Li}^{(-)}]}{nF} \quad (1)$$

In this equation, n is the stoichiometric number of electrons involved in the reaction, F is the Faraday's constant, and ($\mu_{Li}^{(-)}$) and ($\mu_{Li}^{(+)}$) are the chemical potentials of Li in the anode and cathode, respectively. At the cell's fully charged state, $\mu_{Li}^{(-)} > \mu_{Li}^{(+)}$ and therefore the voltage is positive. Upon closing the circuit, Li^+ ions transfer from anode with higher chemical potential to cathode with lower chemical potential, resulting in current flow. Upon discharging, the change of lithium chemical potential in each electrode can be expressed by the Nernst equation:

$$\mu_i = \mu_i^{\circ} + RT\ln a_i \quad (2)$$

Where, μ_i° is the chemical potential of species i in its standard state, a_i is the activity of species, T is the temperature and R is the ideal gas constant (8.315 J/mol.K). Because the activity of a species is equal to its effective concentration, the Nernst equation shows that the chemical potential and therefore the voltage changes as a function of the concentration of Li in each electrode. Typically the potential change is monitored over time and as a regard, the capacity can be defined from the potential-time relation.

Typically lithium reacts with a metal or alloy in three different ways; solid-solution reaction, addition reaction, and displacement or conversion reaction. [20] The first two reactions can be used when lithium ions are added in reactant phase (M), which might be element or a compound, without displacing components from the reactant; $Li + xM \rightarrow LiM_x$. This reaction, depending on whether a phase transformation occurs in the reactant M during insertion of lithium ions into the structure, might be a solid-solution and addition reactions. If a phase change occurs from M to LiM_x, it is referred to an addition reaction. For instance, because of the very low solubility of Li in crystalline Si, Ge, Al and Sn, lithium insertion/extraction in in these elements are addition reactions. In displacement reaction, on the other hand, lithium reacts with one component of the reactant, while the other component, which could be active or inactive towards lithium, is displaced or extruded from the reactant; $Li + xMN_y \rightarrow LiM_x + xyN$.

The importance of a voltage curve in understanding the electrochemical reactions of a material can be explained using Gibbs phase rule, the equation of which is:

$$F = C - P + 2 \tag{3}$$

In Gibbs phase rule, F is the number of degree of freedom, C is the number of independent components and P is the number of phases in the system. The degree of freedom, F, determines the number of thermodynamic parameters which define the system and its related properties, for example the chemical potential and thus, voltage. For a solid-solution reaction, the degree of freedom is three. As the electrochemical reactions are measured at specific temperature and pressure, therefore only one parameter is required to define the system. Since lithium is added to the system, its concentration in LiM_x changes during the reaction. So the concentration of lithium in LiM_x could be the final parameter. Thus, at constant temperature and pressure and

where only one phase exists, the potential varies with the lithium concentration in LiM_x. In this case, the voltage profile has a sloping shape. For an addition reaction in a binary system, the chemical potential is two degree of freedom. As a result, at constant temperature and pressure, no parameter is left to define the system. In this case, the potential is independent of the lithium concentration and the voltage profile is a constant plateau. For a displacement reaction in a ternary Li-M-N system in which three phases exist, the equilibrium potential is independent of the lithium concentration.[20]

II. Capacity

Capacity is the amount of charge that can be stored in the active material. It is usually reported in terms of gravimetric or volumetric specific capacity, which is normalized by the amount of active material in the electrode structure or by the size of material. Volumetric specific capacities can be used where the size of the battery is more important than its weight. Capacities of batteries are often reported in the units of ampere-hours per gram (Ah/g), which represents the charge as an ampere is a Coulomb/sec. For LIBs, if the stoichiometry of the lithiated material, Li_xA is known, the capacity of that material can be calculated. The gravimetric capacity (specific capacity), C_G, and volumetric capacity, C_v, can be calculated as follows:

$$C_G = \frac{1000xF}{3600M_w} \text{ mAh/g} \quad (4)$$

$$C_v = \rho C_G \text{ Ah/L or mAh/cm}^3 \quad (5)$$

Where F is Faraday's constant (9.64853×10^4 C), and M_w and ρ are the molecular weight and density, respectively, of the host material A, and x is the amount of Li in Li_xA,

One of the important parameters in batteries is coulombic efficiency (CE), which is utilized to determine how much the redox reactions are reversible, and is defined as the discharge capacity over charge capacity (equation (6)). In the case of LIBs, for example, coulombic efficiency is the ratio of gained capacity on delithiation over the obtained capacity in lithiation.

$$\text{CE (\%)} = \frac{C_{G,D}}{C_{G,C}} \times 100 \tag{6}$$

CE lower than 100% means that some charge is lost and used for processes other than the reversible lithiation/delithiation reactions. Typically first cycle coulombic efficiency is lower than that of subsequent cycles because of the formation of solid-electrolyte interface (SEI), which is formed due to electrolyte decomposition on the electrode surface and irreversible trapping of Li in the host material. In the first cycle, some of lithium ions are trapped inside the host structure and cannot be released and take apart in subsequent redox reactions, which is known as irreversible capacity. The SEI formation leads to active material surface passivation, which consequently causes an increase in the coulombic efficiency in subsequent cycles. [12]

III. Energy density

Considering the specific capacity of a material and the average potential at which the reaction with lithium occurs, V, the specific energy, E, can be calculated as follows:

$$E = VC_G \tag{7}$$

The gravimetric energy density or specific energy is typically reported in units of Wh/kg while the volumetric energy density is reported in Wh/L. Equation (7) indicates that increaseing

the specific capacity or the voltage can increase the energy of a battery. When considering only the active materials of the cathode and anode, the energy densities of ~560 Wh/kg are obtained for $LiCoO_2$, $LiMn_2O_4$, or $LiFePO_4$ against graphite. However, considering the weight of electrolyte, separator, current collectors, and other inactive components used in battery results in a energy density 50- 70% lower than the theoretical one. [21] Although specific capacity is an important parameter, voltage should be also considered when looking for a new electrode to use in a battery. Voltage is an important parameter because if potential changes dramatically during the lithiation/delithiation process, the energy density will also change. In fact, the high specific capacities of some electrode materials are resulted from their poor voltage characteristics.

IV. Power

The power of a battery is dependent on the magnitude of the current drained during the discharge. Indeed, the larger the current is, the higher the IR losses and polarization effects are. Batteries are typically measured at different currents. "C" rates are used to identify the currents used in galvanostatic (constant current) measurements. The term C over a number (e.g. C/10) refers to charge and discharge rate in battery characterizations, where C means the electrode's full capacity, and the number corresponds to how many hours it takes for battery to be fully charged or discharged. 1C, for example, is defined as the amount of current needed to fully discharge the battery in one hours. This can be calculated from the theoretical capacity, C_G, and the mass of available material, m:

$$1C = mC_G \tag{8}$$

1.1.1.2. Germanium as anode for LIBs

Germanium (Ge) is analogous to Si and fully lithiated $Li_{22}Ge_5$ offers a high theoretical capacity of 1624 $mAhg^{-1}$, which is 45% of that of $Li_{22}Si_5$, but still approximately four times greater than that of conventional graphite. [22] Compared to Si, Ge has some advantages, which makes it a promising candidate for LIB anode materials. Ge has higher intrinsic electronic conductivity due to its smaller band gap (0.6 eV) compared to that of Si (1.1 eV) and exhibits a 400 times higher diffusivity of lithium (Li) than Si at room-temperature, indicating high rate capability demonstrated up to 1000C. [23-27] Ge also undergoes less volume change during lithiation/delithiation rather than Si. Additionally, in contrast to Si, Ge does not form stable oxide on its outermost layers. [24-27] The presence of native oxide on the surface of electrodes usually reduces the overall specific capacity, because of its reaction with lithium during the initial cycle, which leads to the formation of Li_2O and results in a large irreversible capacity for the first cycle. [23]

Despite the huge capacity, the fully lithiated $Li_{22}Ge_5$ undergoes a volume change of 370% during the lithium insertion and extraction leading to high internal stress, pulverization, and loss of electrical contact in bulk electrodes. [18,28] To facilitate strain relaxation and improve the electrode conductivity, many strategies have been recently utilized using Nanostructured materials, [17,27,29-31] nanocomposites, [26,32,-34] and thin films. [18,24,35-37] Due to the large surface-to-volume ratio, nanomaterials are expected to accommodate the large volume change during lithiation/delithiation process without structural degradation and thereby enhance the cycling performance. [38] Moreover, due to their high interfacial contact area of nanostructured materials

with electrolyte, they can improve the cycling stability by introducing short lithium diffusion distances within the electrode speeding up the charge/mass transport. [39]

I. Advantages of Ge nanowire morphologies

Amongst different nanosized morphologies, one-dimensional (1D) nanowires are considered to be more attractive due to their small diameter and 1D conductivity, which allows facile volume expansion in both radial and axial direction without pulverization. They also enhance efficient charge transport, both for electrons from the current collector and Li ions from the electrolyte. [40] Figure 1.2 illustrates the schematic of morphological changes occurring in these kinds of anodes during electrochemical cycling. As could be seen, the thin films and particles are more prone to pulverize compared to NWs during cycling, resulting in poor transport of electron as indicated by arrows. In contrast, germanium nanowires (GeNWs) can more easily accommodate large volume changes during lithium insertion and extraction with capacities near theoretical capacities. [17]

Various synthetic methods for GeNWs have been recently explored, such as thermal co-evaporation, [29] solution-liquid–solid (SLS) growth, [26] vapor-solid-solid (VSS) growth, [41,42] and etc. However, most synthetic approaches for the growth of GeNWs are based upon a vapor-liquid–solid (VLS) mechanism, using chemical vapor deposition (CVD) of a gas-phase precursor. [43-47] Using GeNWs as an anode material grown directly on a metal current collector by VLS growth mechanism have significant benefits, such as the contribution of each nanowire to the capacity because of their electrical connection to the metallic current collector and no need of binders or conducting additives which add extra weight. [39]

As mentioned before, one of the most effective ways to prepare semiconducting GeNWs with controllable diameters and lengths is the bottom-up approach VLS chemical vapor deposition. In the VLS mechanism (Figure 1.3) the reactants are introduced via the vapor phase and dissolve into the catalyst to form a molten alloy of the catalyst and reactant species. Super-saturation of the molten droplet by Ge leads to nucleation and axial growth of a nanowire. [48] Therefore, the VLS growth can be divided to three main steps (i) the gaseous Ge precursor, commonly germane (GeH_4), being cracked at the surface of the catalyst droplet. [49] GeH_4 decomposition occurs during two steps: (1) $GeH_4 \rightarrow GeH_2 + H_2$ and (2) $GeH_2 \rightarrow Ge + H_2$. The released Ge then gets incorporated into the droplet. (ii) it diffuses in the liquid phase, and (iii) crystallizes at the liquid–solid interface (L-S interface). [49]

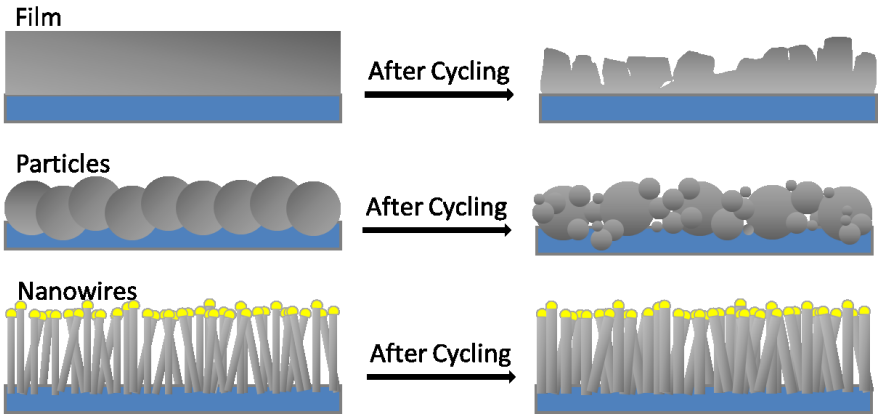

Figure 1.2. Schematic of morphological changes that occur in different structures during cycling.

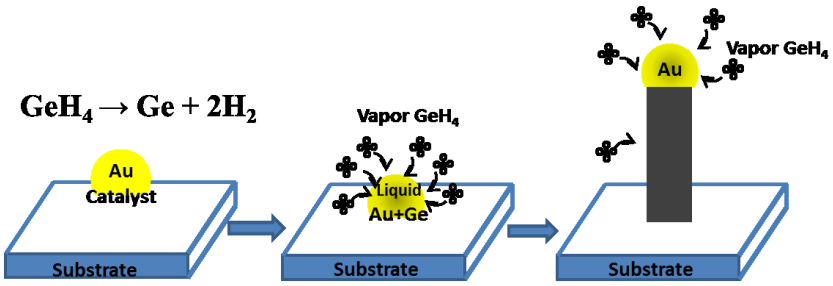

Figure 1.3. The Au catalyzed GeNW growth via VLS mechanism

The requirement of the presence of a liquid for the VLS mechanism suggests that the nanowire growth should be carried out at temperatures above the binary eutectic melting point. [43] However, the growth of germanium nanowires at temperatures below the Au–Ge eutectic temperature have been extensively reported, [28,43-45,48,50] which is in apparent contradiction with the VLS mechanism. It has been suggested that capillary effects, which result in melting point depression for elemental nanoparticles, are responsible for a shift in eutectic temperature to lower temperatures in these binary systems. This can explain nanowire growth at substantially lower temperatures than the real eutectic temperature at which the bulk liquid would solidify. [43] In the Au-Ge binary alloy phase diagram, due to the nanoscale size effects, i.e., the size of the Au nanoparticles and the NW, the liquidus lines will shift and the eutectic temperature will shift to a lower value as shown in Figure 1.4. Therefore, the growth of Ge NWs below the eutectic temperature of bulk Au-Ge is expected. [42,44]

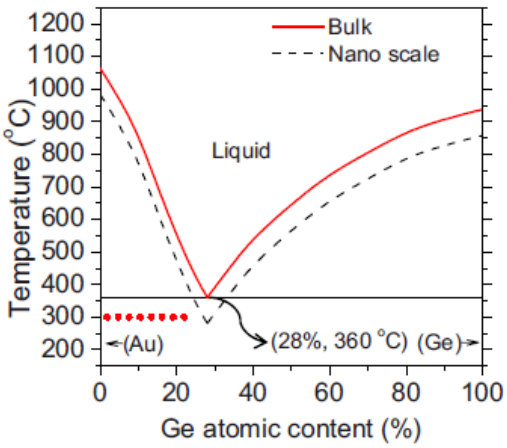

Figure 1.4. Phase diagram of the Au-Ge binary alloy. The solid purple and brown lines are the liquid lines of bulk AuGe while the dashed red and blue lines are the liquid lines of nanoscale AuGe. [42]

1.1.2. Sodium-ion Batteries

While lithium ion batteries (LIBs) are the dominant secondary energy storage source for portable and electric vehicle applications, there are some concerns about lithium's cost and continued availability. Sodium-ion batteries (NIBs) have recently attracted much scientific attention as alternatives to LIBs, since sodium is more readily available than lithium and has a potential for significant associated cost reduction. [51-56] Moreover NIBs are considered as the key technology for meeting large-scale energy storage needs, [57-59] mainly due to much more "geographically democratic" availability of Na and lower cost as compared to Li. NIBs also offer an increased resistance to metal plating-induced shorts. [60] The standard electrode potential is determined by the redox couple and by the ion solvation interactions, with the difference between Li and Na standard potentials in carbonate solvents being in the range of 0.2 - 0.25 V. [61] Table 1.1 shows a comparison between Na and Li elements.

Table 1.1: The comparison between Na and Li elements. [62]

	Na	**Li**
Cation radius (pm)	97	68
Atomic weight (g/mole)	23	6.9
E^0 vs. SHE (V)	-2.7	-3.04
Melting point (^oC)	97.7	180.5
Abundance (mg/Kg)	23.6×10^3	20
Distribution	Everywhere	70% in South America
Price (RMB per Kg)	~2	~40

1.1.2.1 NIB Anode Materials

Although Several classes of cathode materials have been proposed for NIBs, including $Na_{0.44}MnO_2$, $Na_{0.85}Li_{0.17}Ni_{0.21}Mn_{0.64}O_2$, $Na_{0.7}CoO_2$, $Na_3V_2(PO_4)_2F_3$, Na_2FePO_4F, $LiFeSO_4F$, $Na_{4-\alpha}M_{2+\alpha/2}(P_2O_7)_2$ ($2/3 \leq \alpha \leq 7/8$, M = Fe, $Fe_{0.5}Mn_{0.5}$, Mn), Olivines, and NASICONs. [52, 63,64] NIB anodes present more of a challenge since commercial graphite has very low Na storage capacity. [65] Charge storage capacities and cycling stabilities approaching LIB graphite have been demonstrated for various amorphous or partially graphitic carbons. [66-71] Anodes based on titanium oxide, such as $Na_2Ti_3O_7$ and anatase TiO_2 have also been successfully employed. These are highly desirable from a cost and environmental friendliness perspective, while offering capacities of ~ 150 mAh g^{-1} and good cycling stability. [72-78] These materials along with the carbons represent perhaps the most economical anode option for large-scale stationary applications.

As in the case of Li, other Group 14 elements besides carbon have potentially higher storage capacities for sodium. [79] According to the equilibrium phase diagram, Sn can store 3.75 Na/host-atom ($Na_{15}Sn_4$), [80] with a resulting maximum charge storage capacity of 847 $mAhg^{-1}$. The experimentally measured capacity of Sn anodes generally approaches this value early in the testing, but degrades during cycling, *e.g.* [55,58,81-84] For instance, Yamamoto *et al.* [81] reported a NIB negative electrode based on Sn thin film with a discharge (charge) capacity of 790 (729) $mAhg^{-1}$ in the first cycle. However, this electrode showed a rapid capacity decay after 15 cycles. Ellis *et al.* [85] also observed an initial discharge capacity of ~850 $mAhg^{-1}$ for a sputtered Sn electrode, and a rapid cycling-induced capacity degradation to near zero. Sn- based alloy composites have been reported to exhibit improved cycle stability, such as $(Sn_{0.5}Co_{0.5})_{1-x}C_x$ alloy,

[85] $(Cu_6Sn_5)_{1-x}C_x$, [86] SnSb/C nanocomposite, [54] Cu_6Sn_5, [87] $Sn_{0.9}Cu_{0.1}$ alloy, [88] and Sn–SnS–C nanocomposite. [89]

Antimony has also been recently examined for its potential as a NIB anode, *e.g.* [90-93] The maximum stoichiometry of Na-Sb alloys is Na_3Sb, [80,94] giving Sb a theoretical capacity of 660 $mAhg^{-1}$. Authors have examined Sb alloy and intermetallic electrodes, including Cu_2Sb with a capacity of 280 $mAhg^{-1}$, [95] AlSb with a capacity of 490 $mAhg^{-1}$, [96] Mo_3Sb_7 with a capacity of 330 $mAhg^{-1}$, [97] Sb-MWCNT nanocomposites with a capacity of ~500 $mAhg^{-1}$. [98] Germanium in thin film form or as porous nanocolumnar structures have been demonstrated to work as a NIB anodes as well. [99,100] Experimental capacities in the range of 1:1 NaGe (369 $mAhg^{-1}$) have been reported.

1.2. The Motivation and Scope of This Thesis

The main focus of this thesis is to improve the electrochemical performance of germanium-based anode materials for lithium-ion and sodium-ion batteries. As mentioned before, Ge is attractive in terms of energy density, but suffers from a very large volume expansion/shrinkage during ion insertion/extraction. In fact, the high internal strains in Li- and Na-active Ge lead to structural disintegration, pulverization, loss of electronic contact, and ultimately poor capacity retention. In this work, we demonstrate that Ge nanowires grown at an optimum temperature and for an optimum time can significantly withstand the huge volume changes during lithium insertion/extraction and improve the capacity retention. We also present a new Ge-containing ternary alloy with an optimum composition as anode for sodium-ion batteries, which show an excellent electrochemical performance. The degradation mechanisms of

germanium nanostructures as negative electrode materials are investigated through post-cycled characterizations using X-ray diffraction (XRD), scanning electron microscopy (SEM), transmission electron microscopy (TEM), focused ion beam (FIB), X-ray photoelectron spectroscopy (XPS), time of flight secondary ion spectroscopy (TOF-SIMS), electron energy loss spectroscopy (EELS), etc.

In chapter two of this thesis, we show substantial variation in the electrochemical lithiation performance of "1-D" Ge nanowires. We varied the VLS growth temperature (320°C and 360°C) and time (2, 5 and 10 minutes), resulting in Ge nanowire arrays with distinct mass loadings, mean diameters and lengths, and thicknesses of the parasitic Ge films that are formed at the base of the array during growth. We also elucidate that there is a degradation of cycling capacity retention, coulombic efficiency and rate capability with higher mass loading and with coarser array geometry (mean nanowire diameter, mean thickness of the parasitic Ge films at the current collector - array interface). Using TOF-SIMS we are the first to demonstrate marked segregation of Li to the current collector interface in planar Ge films that are 300 and 500 nm thick, but not in the 150 nm specimens. FIB analysis shows that the cycled higher mass loaded electrodes develop more SEI and interfacial cracks near the current collector. The inferior cycling capacity retention and CE is correlated with increasing levels of Li segregation to the current collector interface, and to preferential SEI formation and macroscopic cracking in that region. The inferior rate capability is likely caused by the longer Li diffusion distances associated with the larger diameters of the nanowires, and with the thicker Ge films at the bottom of the arrays. Our findings may serve as a useful design tool for fabricating high performance 1-D nanostructured anodes for Li ion storage applications.

In chapter three, we provide the first report on several compositions of ternary Sn-Ge-Sb for application as NIB anodes. The discovery of new materials and microstructures for sodium ion battery (NIBs or SIBs) electrodes is of high scientific interest. Here we provide the first report on several compositions of ternary Sn-Ge-Sb for application as NIB anodes. Alloy of Sn-25at%Ge-25Sb demonstrates the best overall performance, displaying a reversible capacity as high as 878 mAh/g (at 85 mAh/g), with ~ 609 mAh/g remaining after 50 cycles. This material also has the best rate capability, displaying a stable capacity as high as 381 mAh/g at a very high current density of 8500 mA/g (~ 10C). This capacity, capacity retention, and rate capability are substantially superior to what we obtained for identically synthesized elemental Sn, Sb, Ge, or for Sn-Ge or Sb-Ge. A survey of published literature shows that 878 mAh/g is among the highest reversible capacities reported for any NIB anode, while 381 mAh/g represents the most optimum fast charge value. We employ TEM analysis to assay the cycling microstructure of the binary and ternary electrodes, showing that Sn-25at%Ge-25Sb is a composite of Sn and Ge nanocrystals embedded in an amorphous Sn-Ge-Sb matrix. Our hypothesis is that the measured remarkable capacity is due to the ability of Ge nanocrystallites alloyed with Sn to sodiate beyond the 1:1 Ge:Na (369 mAh/g) ratio previously reported for "stand alone" Ge electrodes, perhaps approaching the 3:1 stoichiometry present on the equilibrium phase diagram.

1.3. References

1 J. M. Tarascon, *Philosophical Transactions of the Royal Society a-Mathematical Physical and Engineering Sciences*, 2010, **368**, 3227.

2 M. Armand, J. M. Tarascon, *Nature,* 2008, **451**, 652.

3 M. M. Thackeray, C. Wolverton, E. D. Isaacs, *Energy & Environmental Science,* 2012, **5**, 7854.

4 V. Etacheri, R. Marom, R. Elazari, G. Salitra, D. Aurbach, *Energy & Environmental Science,* 2011, **4**, 3243.

5 J. B. Goodenough, *Accounts of Chemical Research,* 2013, **46**, 1053.

6 N.-S. Choi, Z. Chen, S. A. Freunberger, X. Ji, Y.-K. Sun, K. Amine, G. Yushin, L. F. Nazar, J. Cho, P. G. Bruce , *Angewandte Chemie International Edition,* 2012, **51**, 9994.

7 A. Patil, V. Patil, D. W. Shin, J.-W. Choi, D.-S. Paik, S.-J. Yoon, *Materials Research Bulletin,* 2008, **43**, 1913.

8 J. M. Tarascon, M. Armand, *Nature,* 2001, **414**, 359 .

9 M.R. Zamfir, H.T. Nguyen, E. Moyen,Y.H. Lee, D. Pribat, *Journal of Materials Chemistry A*, 2013, **1**,9566.

10 B. Xu, D. Qian, Z. Wang, Y. S. Meng, *Materials Science and Engineering: R: Reports,* 2012, **73**, 51.

11 M. I. Hoffert, K. Caldeira, G. Benford, D. R. Criswell, C. Green, H. Herzog, A. K. Jain, H. S. Kheshgi, K. S. Lackner, J. S. Lewis, H. D. Lightfoot, W. Manheimer, J. C. Mankins, M. E Mauel, L. J. Perkins, M. E. Schlesinger, T. Volk, T. M. L. Wigley, *Science*, 2002, **298**, 981.

12 J. R. Szczech, S. Jin, *Energy & Environmental Science*, 2011, **4**, 56-72.

13 J.-M. Tarascon, M. Armand, *Nature*, 2001, **414**, 359-367.

14 M. Wakihara, O. Yamamoto, Wiley-VCH, Japan, 1998.

15 H. Takeshita, *Proceedings of the American Power Conference*, 2000, San Diego.

16 K. Caldeira, A. K. Jain, M. I. Hoffert, *Science,* 2003, **299**, 2052.

17 C. K. Chan, X. F. Zhang and Y. Cui, *Nano Letters*, 2008**, 8**, 307.

18 B. Laforge, L. Levan-Jodin, R. Salot and A. Billard, *Journal of the Electrochemical Society*, 2008, **155**, A181.

19 T. Song, J. L. Xia, J. H. Lee, D. H. Lee, M. S. Kwon, J. M. Choi, J. Wu, S. K. Doo, H. Chang, W. Il Park, D. S. Zang, H. Kim, Y. G. Huang, K. C. Hwang, J. A. Rogers and U. Paik, *Nano Letters*, 2010, **10**, 1710–1716.

20 W.J. Zhang, *Journal of Power Sources*, 2011, **196**, 877-885.

21 D. Linden, T.B. Reddy, *Handbook of Batteries;* 3 ed.; McGraw-Hill: New York, 2001.

22 W. H. Liu et al., "In Situ TEM Experiments of Electrochemical Lithiation and Delithiation of Individual Nanostructures", Advanced Energy Materials, 2012, **2**, 722–741.

23 J. Graetz, C. C. Ahn, R. Yazami and B. Fultz, *Journal of the Electrochemical Society*, 2004, **151**, A698.

24 S. Yoon, C. M. Park and H. J. Sohn, *Electrochemical and Solid State Letters*, 2008, **11**, A42.

25 X. H. Liu, S. Huang, S. T. Picraux, J. Li, T. Zhu and J. Y. Huang, *Nano Letters*, 2011, **11**, 3991.

26 L. P. Tan, Z. Y. Lu, H. T. Tan, J. X. Zhu, X. H. Rui, Q. Y. Yan and H. H. Hng, *Journal of Power Sources*, 2012, **206**, 253.

27 M. H. Park, Y. Cho, K. Kim, J. Kim, M. L. Liu and J. Cho, *Angewandte Chemie-International Edition*, 2011, **50**, 9647.

28 H. Adhikari, A. F. Marshall, C. E. D. Chidsey and P. C. McIntyre, *Nano Letters*, 2006, **6**, 318.

29 Y. D. Ko, J. G. Kang, G. H. Lee, J. G. Park, K. S. Park, Y. H. Jin and D. W. Kim, *Nanoscale*, 2011, **3**, 3371.

30 L. C. Yang, Q. S. Gao, L. Li, Y. Tang and Y. P. Wu, *Electrochemistry Communications*, 2010, **12**, 418.

31 M. H. Seo, M. Park, K. T. Lee, K. Kim, J. Kim and J. Cho, *Energy & Environmental Science*, 2011, **4**, 425.

32 R. A. DiLeo, S. Frisco, M. J. Ganter, R. E. Rogers, R. P. Raffaelle and B. J. Landi, *Journal of Physical Chemistry C*, 2011, **115**, 22609.

33 J. S. Cheng and J. Du, *Crystengcomm*, 2012, **14**, 397.

34 Y. Hwa, C. M. Park, S. Yoon and H. J. Sohn, *Electrochimica Acta*, 2010, **55**, 3324.

35 L. Baggetto, E. J. M. Hensen and P. H. L. Notten, *Electrochimica Acta*, 2010, **55,** 7074.

36 S. Fang, L. Shen, P. Nie, G. Xu, J. Wang and X. Zhang, *Journal of Materials Science*, 2014, **49**, 2279.

37 L. Baggetto and P. H. L. Notten, *Journal of the Electrochemical Society*, 2009, **156**, A169.

38 R. Huang and J. Zhu, *Materials Chemistry and Physics*, 2010, **121**, 519.

39 E. L. Memarzadeh, W. P. Kalisvaart, A. Kohandehghan, B. Zahiri, C. M. B. Holt and D. Mitlin, *Journal of Materials Chemistry*, 2012, **22**, 6655.

40 S. Misra, N. Liu, J. Nelson, S. S. Hong, Y. Cui and M. F. Toney, *Acs Nano*, 2012, **6**, 5465.

41 S. V. Thombare, A. F. Marshall and P. C. McIntyre, *Journal of Applied Physics*, 2012, **112**.

42 C. B. Li, K. Usami, H. Mizuta and S. Oda, *Journal of Applied Physics*, 2009, 106.

43 H. Adhikari, P. C. McIntyre, A. F. Marshall and C. E. D. Chidsey, *Journal of Applied Physics*, 2007, **102**.

44 M. Simanullang, K. Usami, T. Kodera, K. Uchida and S. Oda, *Japanese Journal of Applied Physics*, 2011, **50**.

45 S. Kodambaka, J. Tersoff, M. C. Reuter and F. M. Ross, *Science*, 2007, **316**, 729.

46 M. S. Song, J. H. Jung, Y. Kim, Y. Wang, J. Zou, H. J. Joyce, Q. Gao, H. H. Tan and C. Jagadish, *Nanotechnology*, 2008, **19**.

47 I. R. Musin and M. A. Filler, *Nano Letters*, 2012, **12**, 3363.

48 H. Adhikari, A. F. Marshall, I. A. Goldthorpe, C. E. D. Chidsey and P. C. McIntyre, *Acs Nano*, 2007, **1**, 415.

49 C. Renard, R. Boukhicha, C. Gardes, F. Fossard, V. Yam, L. Vincent, D. Bouchier, S. Hajjar, J. L. Bubendorff, G. Garreau and C. Pirri, *Thin Solid Films*, 2012, **520**, 3314.

50 T. I. Kamins, X. Li and R. S. Williams, *Nano Letters*, 2004, **4**, 503.

51 M. D. Slater, D. Kim, E. Lee and C. S. Johnson, Advanced Functional Materials, 2013, **23**, 947-958.

52 B. L. Ellis and L. F. Nazar, Current Opinion in Solid State & Materials Science, 2012, **16**, 168-177.

53 V. Palomares, P. Serras, I. Villaluenga, K. B. Hueso, J. Carretero-Gonzalez and T. Rojo, Energy & Environmental Science, 2012, **5**, 5884-5901.

54 L. F. Xiao, Y. L. Cao, J. Xiao, W. Wang, L. Kovarik, Z. M. Nie and J. Liu, Chemical Communications, 2012, **48**, 3321-3323.

55 Y. H. Xu, Y. J. Zhu, Y. H. Liu, C. S. Wang, *Advanced Energy Materials*, 2013, **3**, 128-133.

56 S. W. Kim, D. H. Seo, X. H. Ma, G. Ceder and K. Kang, Advanced Energy Materials, 2012, **2**, 710-721.

57 V. Palomares, M. Casas-Cabanas, E. Castillo-Martinez, M. H. Han and T. Rojo, Energy & Environmental Science, 2013**, 6**, 2312-2337.

58 V. L. Chevrier and G. Ceder, Journal of the Electrochemical Society, 2011, **158**, A1011-A1014.

59 H. L. Pan, Y. S. Hu and L. Q. Chen, Energy & Environmental Science, 2013, **6,** 2338-2360.

60 Pourbaix, M. Atlas of Electrochemical Equilibria in Aqueous Solutions, National Association of Corrosion Engineers, 1974.

61 R. Wibowo, L. Aldous, S. E. W. Jones, R. G. Compton, Chemical Physical Letters, 2010, **492**, 276-280.

62 H. Pan, Y.-S. Hu, L. Chen, *Energy & Environmental Science*, 2013, **6**, 2338.

63 K-H. Ha, S. H. Woo, D. Mok, N-S. Choi, Y. Park, S. M. Oh, Y. Kim, J. Kim, J. Lee, L. F. Nazar, K. T. Lee, *Advanced Energy Materials*, 2013, **3**, 770-776.

64 R. Tripathi, G. R. Gardiner, M. S. Islam and L. F. Nazar, *Chemistry of Materials*, 2011, **23**, 2278-2284.

65 A. Metrot, D. Guerard, D. Billaud and A. Herold, *Synthetic Metals*, 1980, **1**, 363-369.

66 Y. L. Cao, L. F. Xiao, M. L. Sushko, W. Wang, B. Schwenzer, J. Xiao, Z. M. Nie, L. V. Saraf, Z. G. Yang and J. Liu, *Nano Letters*, 2012, **12**, 3783-3787.

67 W. Luo, J. Schardt, C. Bommier, B. Wang, J. Razink, J. Simonsen and X. L. Ji, *Journal of Materials Chemistry A*, 2013, **1**, 10662-10666.

68 S. Komaba, W. Murata, T. Ishikawa, N. Yabuuchi, T. Ozeki, T. Nakayama, A. Ogata, K. Gotoh and K. Fujiwara, *Advanced Functional Materials*, 2011, **21**, 3859-3867.

69 J. Ding, H. Wang, Z. Li, A. Kohandehghan, K. Cui, Z. Xu, B. Zahiri, X. Tan, E. M. Lotfabad, B. C. Olsen and D. Mitlin, *Acs Nano*, 2013, **7**, 11004.

70 Y. Y. Shao, J. Xiao, W. Wang, M. Engelhard, X. L. Chen, Z. M. Nie, M. Gu, L. V. Saraf, G. Exarhos, J. G. Zhang and J. Liu, *Nano Letters*, 2013, **13**, 3909-3914.

71 A. Ponrouch, A. R. Goni, M. R. Palacin, *Electrochemical Communication*, 2013, **27**, 85-88.

72 P. Senguttuvan, G. Rousse, V. Seznec, J. M. Tarascon, M. R. Palacin, *Chemistry of Materils,* 2011, **23**, 4109-4111.

73 L. Zhao, H. L. Pan, Y. S. Hu, H. Li, L. Q. Chen, *Chinese Physics B*., 2012, **21**, 028201.

74 H. L. Pan, X. Lu, X. Q. Yu, Y. S. Hu, H. Li, X. Q. Yang, L. Q. Chen, *Advanced Energy Materials*, 2013, **3**, 1186-1194.

75 A. Rudola, K. Saravanan, C. W. Mason, P. Balaya, *Journal of Materials Chemistry A*, 2013, **1**, 2653-2662.

76 Y. Xu, E. M. Lotfabad, H. L. Wang, B. Farbod, Xu, W. Z. A. Kohandehghan, D. Mitlin, *Chemical Communication*, 2013, **49**, 8973-8975.

77 K-T. Kim, G. Ali. K.Y. Chung, C.S. Yoon, H. Yashiro, Y.K. Sun, Y-K. Sun, J. Lu, K. Amine, S-T. Myung, *Nano Letters*, 2014, 14, **2**, 416–422.

78 L. Wu, D. Buchholz, D. Bresser, L.G. Chagas, S. Passerini, *Journal of Power Sources.*, 2014, **251**, 379–385.

79 H. Kim, G. Jeong, Y-U. Kim, J-H. Kim, C-M. Park, H-J. Sohn, *Chemical Society Reviews*, 2013,**42**, 9011-9034.

80 H. Okamoto, Desk Handbook "Phase Diagrams for Binary Alloys", *ASM International*, 2000.

81 T. Yamamoto, T. Nohira, R. Hagiwara, A. Fukunaga, S. Sakai, K. Nitta and S. Inazawa, *Journal of Power Sources*, 2012, **217**, 479-484.

82 H.L. Zhu, Z. Jia, Y.C. Chen, N. Weadock, J.Y. Wan, O. Vaaland, X.G. Han, T. Li, L.B. Hu, *Nano Letters*, 2013, **13**, 3093-3100.

83 L. D. Ellis, T. D. Hatchard, M. N. Obrovac, *Journal of Electrochemical Society*, 2012, **159**, A1801-A1805.

84 L. Baggetto, P. Ganesh, R.P. Meisner, R.R. Unocic, J.C. Jumas, C.A. Bridges, G.M. Veith, *Journal of Power Sources*, 2013, **234**, 48-59.

85 L. D. Ellis, P. P. Ferguson and M. N. Obrovac, *Journal of the Electrochemical Society*, 2013, **160**, A869-A872.

86 J. S. Thorne, R. A. Dunlap, M. N. Obrovac, *Electrochimica Acta*, 2013, **112**, 133-137.

87 L. Baggetto, J.C. Jumas, J. Górka, C.A. Bridges, G. M. Veith, *Physical Chemistry Chemical Physics*, 2013,**15**, 10885-10894.

88 Y.-M. Lin, P. R. Abel, A.Gupta, J. B. Goodenough, A. Heller, C. B. Mullins, *ACS Applied Materials Interfaces*, 2013, **5**, 8273-8277.

89 L. Wu, X. H. Hu, J. F. Qian, F. Pei, F. Y. Wu, R. J. Mao, X. P. Ai, H. X. Yang and Y. L. Cao, *Journal of Materials Chemistry A*, 2013, **1**, 7181-7184.

90 A. Darwiche, C. Marino, M. T. Sougrati, B. Fraisse, L. Stievano and L. Monconduit, *Journal of the American Chemical Society*, 2012, **134**, 20805-20811.

91 J. F. Qian, Y. Chen, L. Wu, Y. L. Cao, X. P. Ai and H. X. Yang, *Chemical Communications*, 2012, **48**, 7070-7072.

92 Y. J. Zhu, X. G. Han, Y. H. Xu, Y. H. Liu, S. Y. Zheng, K. Xu, L. B. Hu and C. S. Wang, *ACS Nano*, 2013, **7**, 6378-6386.

93 D-H. Nam, K-S. Hong, S-J. Lim, H-S. Kwon, *Journal of Power Sources*, 2014**, 247**, 423-427.

94 L. Baggetto, P. Ganesh, C. N. Sun, R. A. Meisner, T. A. Zawodzinski and G. M. Veith, *Journal of Materials Chemistry A*, 2013, **1**, 7985-7994.

95 L. Baggetto, E. Allcorn, A. Manthiram and G. M. Veith, *Electrochemistry Communications*, 2013, **27**, 168-171.

96 L. Baggetto, M. Marszewski, J. Gorka, M. Jaroniec and G. M. Veith, *Journal of Power Sources*, 2013, **243**, 699-705.

97 L. Baggetto, E. Allcorn, R. R. Unocic, A. Manthiram and G. M. Veith, *Journal of Materials Chemistry A*, 2013, **1**, 11163-11169.

98 X. Zhou, Z. Dai, X., J. Bao and Y. G. Guo, *Journal of Materials Chemistry A*, 2013, **1**, 13727-13731.

99 P. R. Abel, Y.-M. Lin, T. d. Souza, C.-Y. Chou, A. Gupta, J. B. Goodenough, G. S Hwang, A. Heller and C. B. Mullins, *Journal of Physical Chemistry C*, 2013, **117**, 18885-18890.

100 L. Baggetto, J. K. Keum, J. F. Browning and G. M. Veith, *Electrochemistry Communications*, 2013, **34**, 41-44.

2. Array Geometry Dictates Electrochemical Performance of Ge Nanowire Lithium Ion Battery Anodes

Material in this chapter has been accepted in Journal of Materials Chemistry A., 2014, 2 (39), 16770 – 16785.

List of authors: Farbod B., Cui K., Kupsta M., Kalisvaart W. P., Memarzadeh E., Kohandehghan A., Zahiri B., and Mitlin D.

2.1. Introduction

Lithium ion batteries (LIBs) are rechargeable batteries meeting high power density demands of the portable electronic and implantable devices as well as electric and hybrid electric vehicle. [1-3] Commercial LIB anodes are primarily based on graphite, in which a maximum theoretical specific capacity of 372 mAh g^{-1} may be achieved. [4] Since this capacity is less than that required for high-energy applications, alternative anode materials are being sought. Germanium with the theoretical capacity of 1624 mAh g^{-1} ($Li_{22}Ge_5$) is considered to be a promising alternative [5-7]. Despite its higher price, Ge has some advantages over Si, including 10^4 times higher electrical conductivity, and 400 times higher lithium diffusivity at room temperature. [8-10] Compared to Si, Ge forms a much less tenacious native oxide at its outermost layer, resulting in a decreased Li_2O formation during first lithiation and thereby an improved

initial coulombic efficiency. [11] However, similarly to Si, the high internal strains in Li-active Ge lead to structural disintegration, pulverization, loss of electronic contact, and ultimately poor capacity retention. [12-14] While attractive in terms of energy density, Ge also suffers from a very large volume expansion/shrinkage during lithium insertion/extraction. As a comparison, graphite expands 10% upon lithiation to LiC_6, [15] $Li_{22}Ge_5$ exhibits 370 % [5] volume expansion.

To improve capacity retention many strategies have been recently implemented using Ge planar films, [11,16-21] nanoparticles, [10,22-30] nanotubes, [31] alloyed nanocrystals, [32,33] and "1-D" nanowires. [8,34-43] Such structures are also expected to demonstrate improved rate capability due to the high specific surface area available for Li uptake and charge transfer. [44] However, the large surface area is also a disadvantage, leading to formation of copious amounts of solid electrolyte interphase (SEI) and an accompanying irreversible capacity loss. [45-49] Being manufacturable en-masse through various VLS and solution growth mechanisms, Ge nanowires (GeNWs) remain highly scientifically interesting. Lithiation and expansion of Ge nanowires has been reported to proceed isotropically, [50-52] contrary to the dumbbell-shapes that develop in SiNWs. [49,53,54] Early studies on GeNWs reveal that the cycling stability requires further improvement [35-42] and that it varies substantially from study to study. For instance, authors in [38] reported a capacity loss of 65.7% for bare GeNWs, cycled 50 times at the rate of 0.1C. Losses higher than 50% over the first 20 cycles have been reported as well. [39] Other studies show that GeNWs grown directly on a current collector are generally more favorable. [39-41,55] VLS-grown GeNWs using chemical vapor deposition (CVD) from GeH_4 showed ~1000 mAh g^{-1} capacity at 0.05C over the first 20 cycles [40]. Failure modes for GeNWs appear to be distinct form their Si counterparts. For instance highly anisotropic expansion followed by break-up into thinner filaments has been observed during

lithiation of SiNWs. [52,53,56,57] GeNWs, on the other hand, expands more isotropically becoming porous over the course of cycling. [58]

Our original objective was to investigate the role of GeNW array geometry on its cycling capacity retention and rate capability as a lithium ion battery anode. Remarkably, despite a large number of high quality studies (e.g. those cited in this Introduction and in Table 2.3) on a given GeNW array with a fixed architecture, the actual role of the mean nanowire length, diameter, etc. on the electrochemical performance has not been explicitly examined. While there is some (primarily modeling) work on geometric-aspects of the lithiation behavior of Si nanowires, as will be discussed in the main manuscript, the two systems are sufficiently distinct. The mean nanowire diameters and lengths in the arrays were tuned by changing the vapor-liquid-solid (VLS) growth temperatures (320°C and 360°C) and times (2, 5 and 10 minutes). We started with a hypothesis that thicker nanowires will fail at faster rates due to the higher differential stresses incurred between their lithiated and non-lithiated sections. For a given growth temperature, this relationship was indeed observed. We also documented a factor of 3X improvement in the electrodes' rate capability when the mean nanowire diameter was halved. When the capacity retention and steady-state coulombic efficiency were plotted against the electrode mass loading, there was a clear empirical tend of decreasing performance with higher loading that spanned an order of magnitude in active material weight (~ 0.1 - 1 mg cm^{-2}). Such a strong correlation has never been reported in literature for either Ge or Si nanowires. This study is also the first to examine the role of the parasitic thin film layer sitting at the base of the nanowire arrays in establishing the cycling performance of Ge nanowires. Parasitic films are widely reported in literature for VLS grown Si and Ge nanowires [59-65] and have been recently examined by Picraux et al. [59] only for the case of Si. However their role remains unexplored for the fundamentally

different case of Ge nanowires. Time of Flight Secondary Ion Spectroscopy (TOF-SIMS) is a powerful emerging technique that is becoming employed to analyze Li interfacial segregation in Si and Sn [66,67,68,69] and Na segregation in Sn alloy films. [70] Here we are the first to employ TOF-SIMS to probe Li segregation in Ge, delivering a finding that such segregation does indeed occur but is highly thickness dependent, with consequently profound implications on the mechanical performance of a range of Ge-based electrodes. Finally we provide a systematic comparison of the performance of our best GeNW arrays with a range of state-of-the-art Ge nanostructures reported in literature. We demonstrate that our materials are among the best in terms of a range of key parameters, such as the initial capacity, the cycling capacity retention, the cycling coulombic efficiency and the rate capability.

2.2. Experimental Procedure

Germanium nanowires (GeNWs) of varying mass loadings were grown on commercial 316 stainless steel spacers (MTI Corporation) that were polished down to 0.05 micron. The nanowires were grown in a commercial CVD tube furnace (Tystar, Inc.) by the vapor-liquid-solid (VLS) mechanism. A 200 nm TiN conductive diffusion barrier layer and a 10 nm Au seed catalyst layer were employed. The furnace was heated up to the growth temperature, either 320 or 360 °C, at 10 ^{o}Cmin^{-1} under a flow of Ar and H_2. Even though 320 ^{o}C is well below the eutectic temperature of Au-Ge, nanowire growth can still occur by the VLS mechanism. When the Au catalyst particles are in the order of several tens of nanometers, the eutectic point can shift to lower temperature. [60,71] To dewet the Au catalytic film, the substrates were held at the growth temperature for 1 hour prior to introducing GeH_4. During the growth process, a mixture of

GeH_4:H_2 with a flow ratio of 1:4 was used as a working gas and the total pressure of chamber was set at 100 Torr. Three different growth times, 2, 5, and 10 minutes, were employed.

Standard 2032 half-cells were assembled using lithium metal foil as the counter electrode and polyethylene separators (MTI Corporation, porosity of 36-44% and average 0.03 μm pore size). The spacers were weighted before and after GeNWs deposition. The microbalance employed (Mettler Toledo, XP6U) had a manufacturer quoted 0.1 μg accuracy. 1 M lithium hexafluorophosphate ($LiPF_6$) salt in 1:1:1 volume ratio of ethylene carbonate: dimethyl carbonate: diethyl carbonate (EC:DMC:DEC) was used as electrolyte. The assembly process was carried out in an argon-filled glovebox in which oxygen and moisture concentration levels were kept below 0.2 ppm. Galvanostatic charge-discharge measurements were carried out on a BT2000 Arbin potentiostat at a potential range of 0.01-2 V vs. Li/Li^+ and a constant current (CC) density. Cyclic voltammetry (CV) experiments were carried out using a Solartron 1470 Multistat system with Corrware data acquisition software, in which the potential was scanned in a range of 0.01-2 V vs. Li/Li^+ with a scan rate of 1 mV s^{-1} for 10 cycles. After testing, the samples were disassembled in order to do post-cycling characterization of the microstructure. The cycled electrodes were soaked and rinsed in acetonitrile and kept overnight in the glovebox to remove residual electrolyte. All testing was performed at room temperature.

The as-grown and cycled nanowire samples were characterized using scanning electron microscopy (SEM) (Hitachi FESEM S-4800) and transmission electron microscopy (TEM) (JEOL 2100, 200 kV). Cross-sectional images of cycled electrodes were obtained using a dual beam FIB/SEM (Hitachi NB5000). Electron diffraction patterns were simulated using the commercial software Crystal Maker ™ and open-source software Diffraction Ring Profiler, [72]

with the input of known space group information of Ge (Fd3m, 5.6578, 5.6578, 5.6578, Wyckoff position: 8a). Electron energy loss spectroscopy (EELS) measurements were conducted using scanning TEM (STEM) (JEOL 2200FS, 200 kV) with a nominal analytical beam size of 0.5 nm. High angle annular dark field (HAADF) images were also recorded simultaneously with the EELS analysis. We mapped Ge, C and O by integrating over core-loss edges of Ge-L, C-K, and O-K edge, respectively. Lithium maps for cycled materials were obtained from the low-loss Li-K edge at 60-70 eV. Digital Micrograph (Gatan, Inc.) was employed for signal collection and data extraction from EELS spectra. XPS measurements were conducted on an ULTRA (Kratos Analytical) spectrometer under ultrahigh vacuum (10^{-9} Torr), using monochromatic Al-K_α radiation ($h\nu$ = 1486.6 eV) operated at 210 W. The high-resolution spectra were collected with an energy window of 20 eV. The XPS data were analyzed using CasaXPS software. Planar Ge thin films were depth analyzed using time-of-flight secondary ion mass spectroscopy (TOF-SIMS) instrument, ION-TOF GmbH. The analysis chamber was kept at a pressure of $< 5 \times 10^{-9}$ mbar. 1 kV O_2 ions with current of ~ 40 nA were used for sputtering over an area of 200 × 200 μm^2 and a 25 kV Bi ion source was used for analysis over an area of 40 × 40 μm^2.

2.3. Results and Discussion

The GeNWs were grown for three different growth times, 2, 5, and 10 minutes, at temperatures of 320°C or 360°C. For the remainder of manuscript, the samples will be labeled according to their mass loading which corresponds to a specific growth temperature - time combination: 0.12mg-(320/2min), 0.31mg-(320/5min), 0.73mg-(320/10min), 0.2mg-(360/2min), 0.52 mg-(360/5min), 0.86 mg-(360/10min).

Plan - view and cross-sectional images of as-grown nanowires for 0.12mg-(320/2min), 0.2mg-(360/2min), 0.52mg-(360/5min) are shown in Figure 2.1. The samples 0.31mg-(320/5min), 0.73mg-(320/10min) and 0.86mg-(360/10min) are shown in Figure 2.2. The wires are all shown at the same magnification. The high-magnification insets show that the 0.52mg-(360/5min) and 0.86mg-(360/10min) nanowires possess a two-tiered morphology. The top parts of the nanowires, below the Au catalyst droplets at the tips, are smooth, whereas further down the nanowire there is a transition to a different morphology where the surface becomes much rougher and tapered. The nanowire diameter and length distribution histograms are shown in Figure 2.3. Approximately 200 nanowires were analyzed per synthesis condition. With longer growth times not only does the mean nanowire diameter increase, but the overall diameter distribution broadens.

In addition to being present as crystalline nanowires, the Ge is also present as a largely continuous parasitic thin film layer sitting at the base of the array. The arrows in the cross-sectional images mark these films, with the associated numbers representing their mean thickness and standard deviation. It is important to point out that parasitic films are not a particularity of our CVD process (which was performed in a commercial nanowire growth reactor), but are a fairly universal feature of Ge and Si nanowire growth through VLS. For instance, Cho and Picraux have recently detailed the ubiquity of parasitic layers (in that case semicontinuous islands) at the nanowire base for VLS Si nanowires. [59] The authors demonstrated that their formation could only be avoided by growth involving a tailored anodized aluminum oxide template. For the case of VLS Ge nanowires, parasitic islands near the current collector were reported in a range of studies. [60-65] In our samples, with increasing growth time and with a higher growth temperature the parasitic Ge layers thickened.

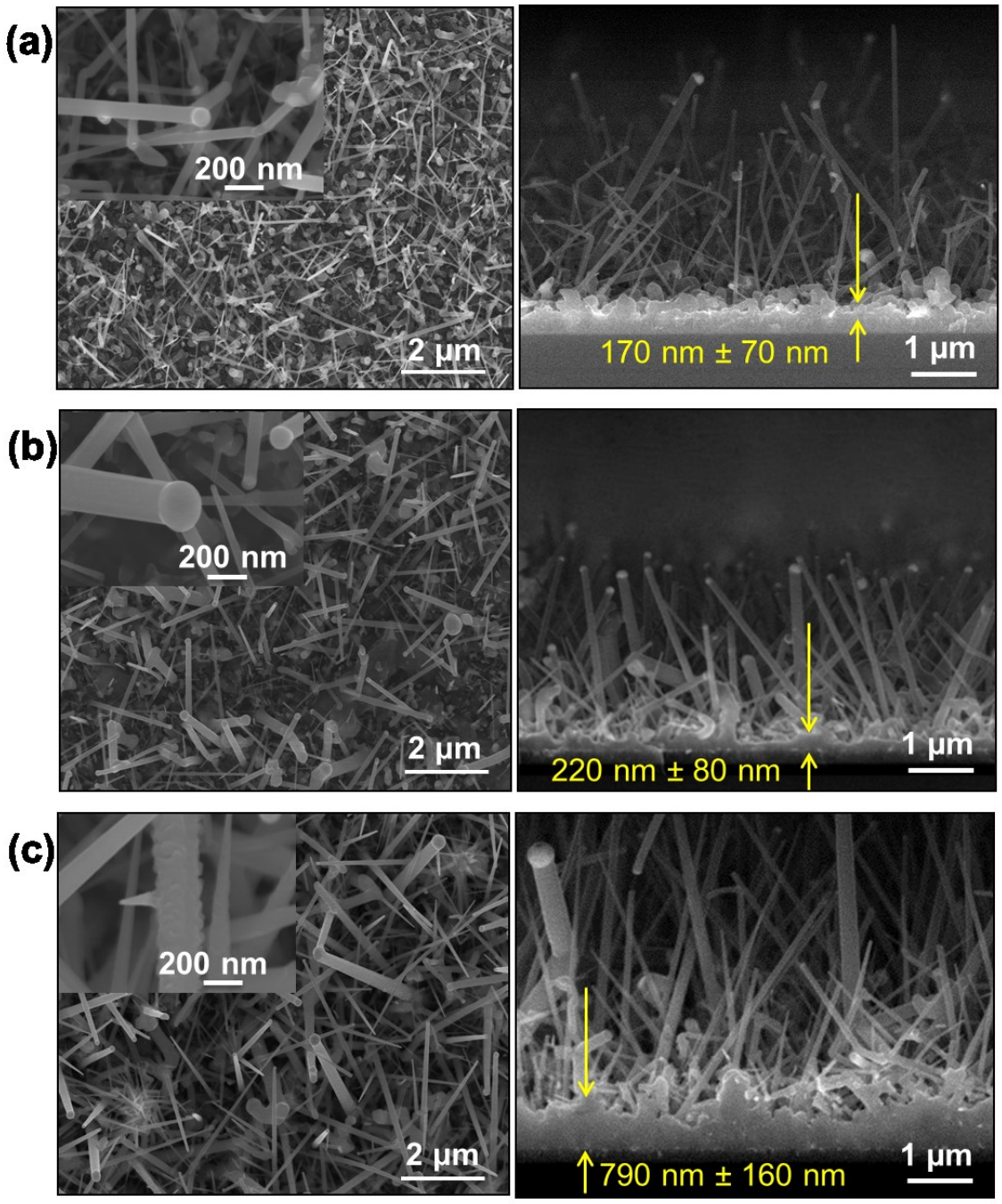

Figure 2.1: Plan-view (left-column) and cross-sectional (right column) SEM images of as synthesized nanowires. (a) 0.12mg-(320/2min); (b) 0.2mg-(360/2min); (c) 0.52mg-(360/5min); The images for samples grown with the remaining three sets of conditions are shown in 2.2. Parasitic Ge films, formed at the nanowire base during VLS growth, are indicated by arrows in cross-sectional images.

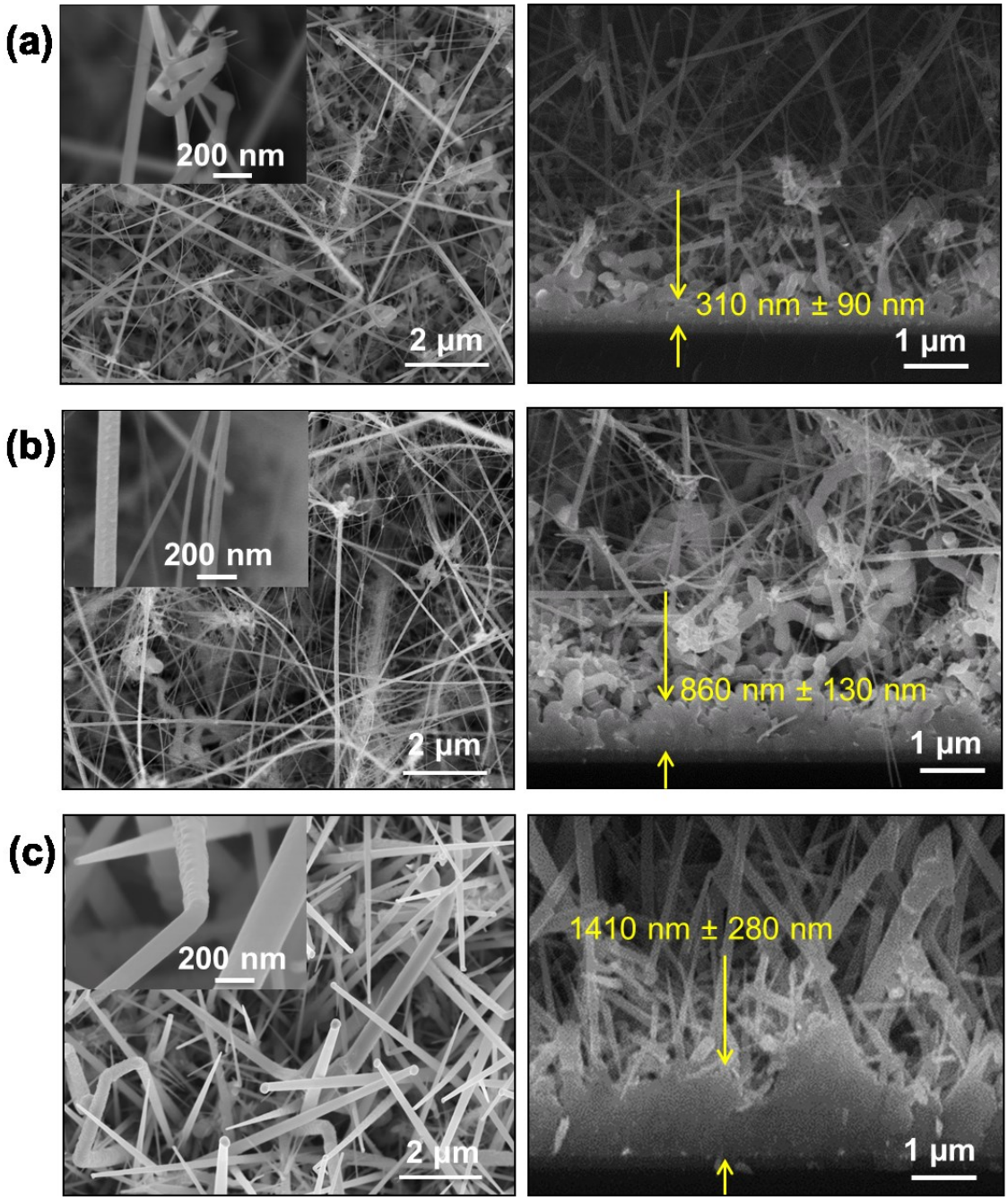

Figure 2.2: Plan-view (left column) and cross-sectional (right column) SEM images of as synthesized nanowires. (a) 0.31mg-(320/5min); (b) 0.73mg-(320/10min); (c) 0.86mg-(360/10min). Parasitic Ge films, formed at the nanowire base during VLS, are indicated by arrows in cross-sectional images.

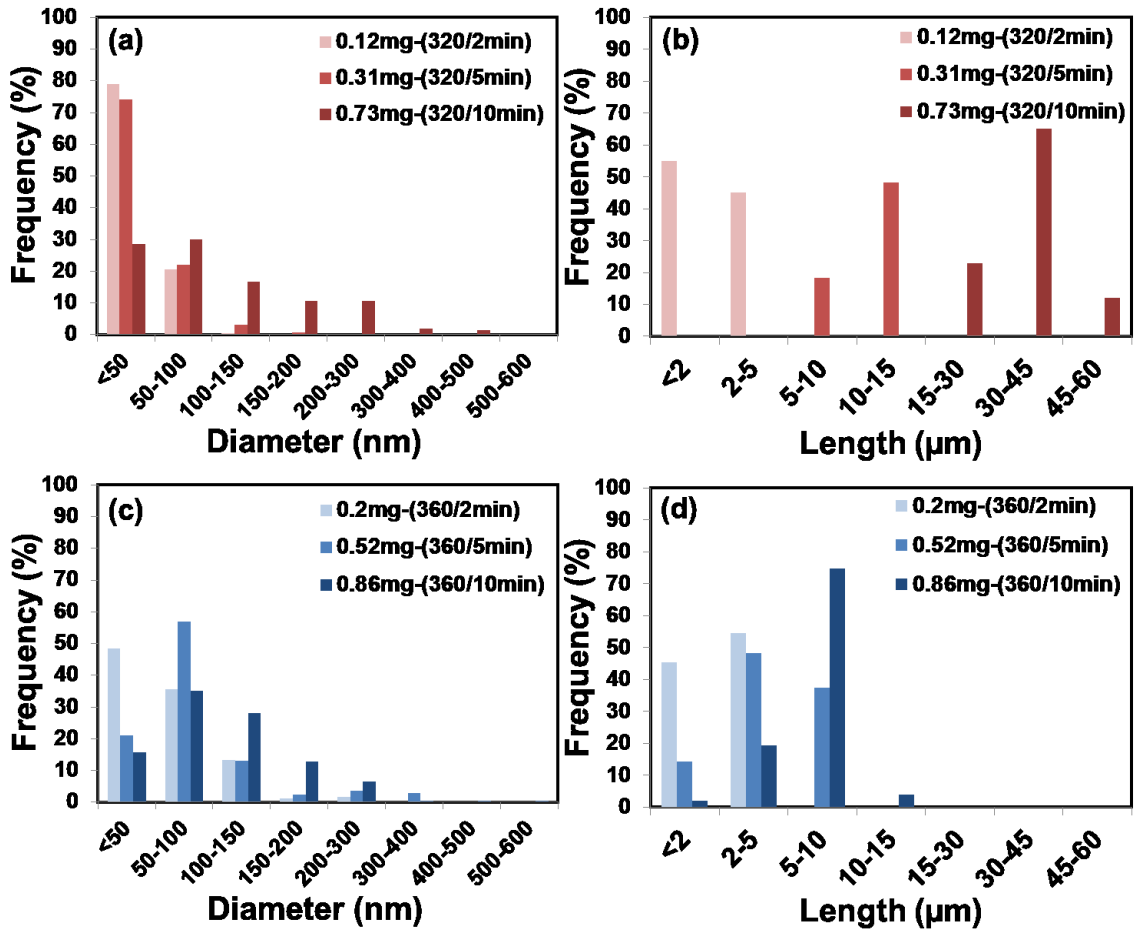

Figure 2.3: (a) – (d) Diameter and length distribution histograms of the as-synthesized GeNWs, grown at 320 °C and 360 °C.

Table 2.1 provides the mean and standard deviation values for the nanowire length, the nanowire diameter and the parasitic layer thickness, for each synthesis conditions. For the more tapered nanowires grown at 360°C, the diameter was measured in the middle of the nanowire. For a given temperature, higher growth times also lead to longer nanowires. However, the nanowires grown at 360°C are consistently shorter than the ones grown for the same duration at 320°C. For a given growth duration the higher growth temperature also yields a higher Ge mass loading. Figure 2.4 shows conventional and high resolution TEM analysis for the 0.12mg-

(320/2min), 0.73mg-(320/10min) and 0.86mg-(360/10min) specimens. The 320°C grown nanowires are primarily single crystal or twinned single crystal. The 360°C grown nanowires are also single crystal at their core, but contain a substantial fraction of secondary Ge nanocrystallites nucleated near the nanowire base. This is what is responsible for the tapered morphology especially observed in the 0.86 mg-(360/10min) sample. Figure 2.5 shows the XPS results of the as-synthesized electrodes. The presence of a minor oxygen peak in addition to a strong Ge signal indicates that the as-grown nanowires are covered by a layer of oxide that is quite thin, likely in the single nanometer or sub nanometer range.

Table 2.1: Mean and standard deviation values for the nanowire length, nanowire diameter, and the thin film layer thickness versus processing conditions.

Electrode	Mean diameter (nm)	Mean length (μm)	Mean thickness of Ge thin film (nm)
0.12mg-(320/2min)	34 ± 19	2 ± 0.7	170 ± 70
0.31mg-(320/5min)	35 ± 30	13 ± 3.5	310 ± 90
0.73mg-(320/10min)	106 ± 81	36 ± 8.3	860 ± 130
0.2mg-(360/2min)	64 ± 42	2 ± 0.7	220 ± 80
0.52mg-(360/5min)	88 ± 61	4 ± 1.5	790 ± 160
0.86mg-(360/10min)	115 ± 76	7 ± 2.0	1410 ± 280

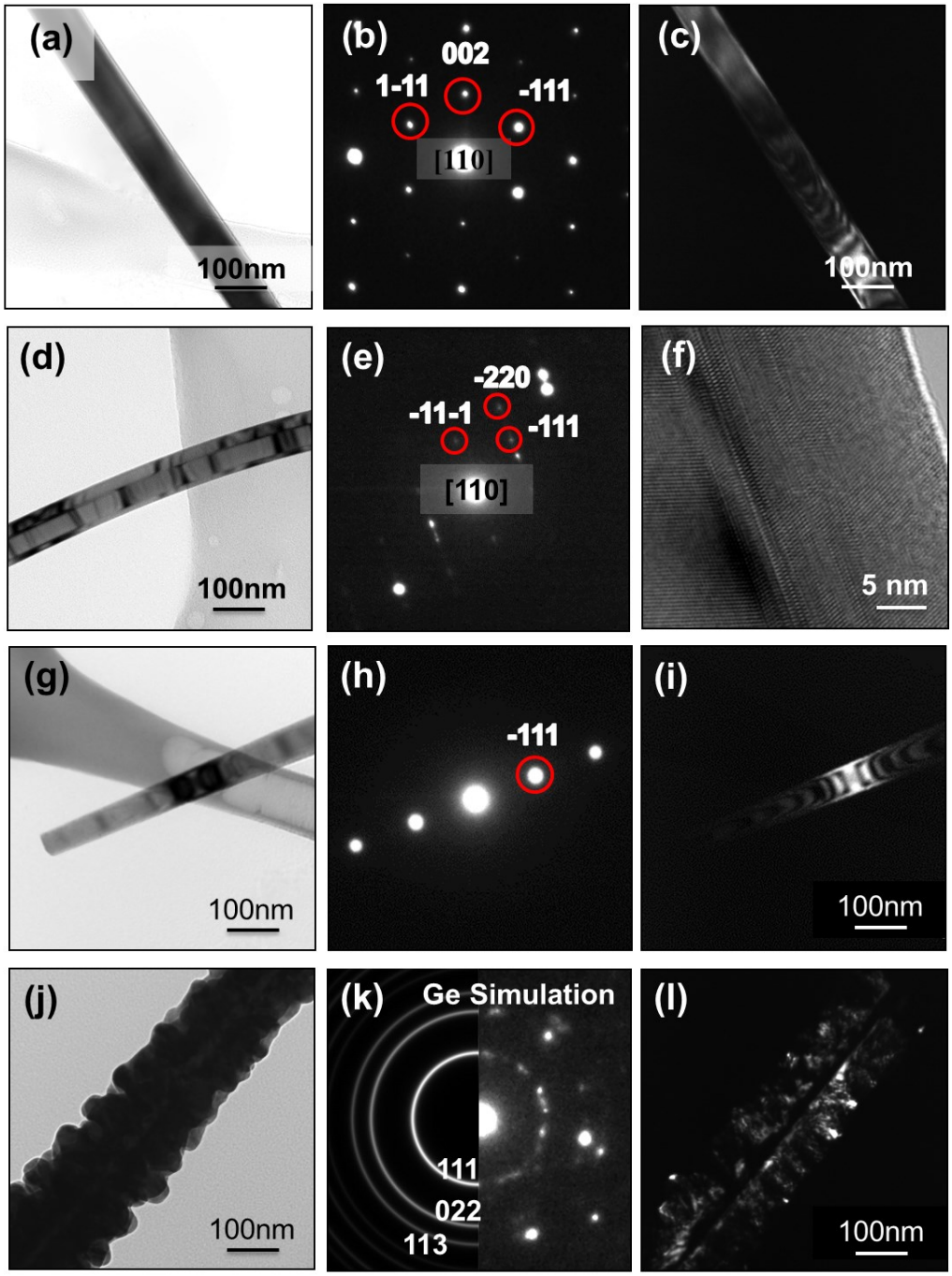

Figure 2.4: (a) – (c) TEM analysis of 0.12mg-(320/2min); (a) bright field image of a single Ge nanowire; (b) SAD pattern confirming that it is single crystal; (c) dark field image taken using g = -111 reflection. (d) – (f) TEM analysis of 0.73mg-(320/10min); (d) bright-field image showing this nanowire to be multiply twinned along its length (e) SAD pattern streaked perpendicular to the twin interface f) HRTEM image showing a twin interface (g) – (l) TEM analysis of the near-top portion of a nanowire 0.86mg-(360/10min), showing the core single crystal. (j) – (l) TEM analysis of the near-base portion another nanowire in 0.86mg-(360/10min), showing the secondary nucleated Ge particles around the core. The dark field image in (l) was taken using a section of the 111 ring pattern.

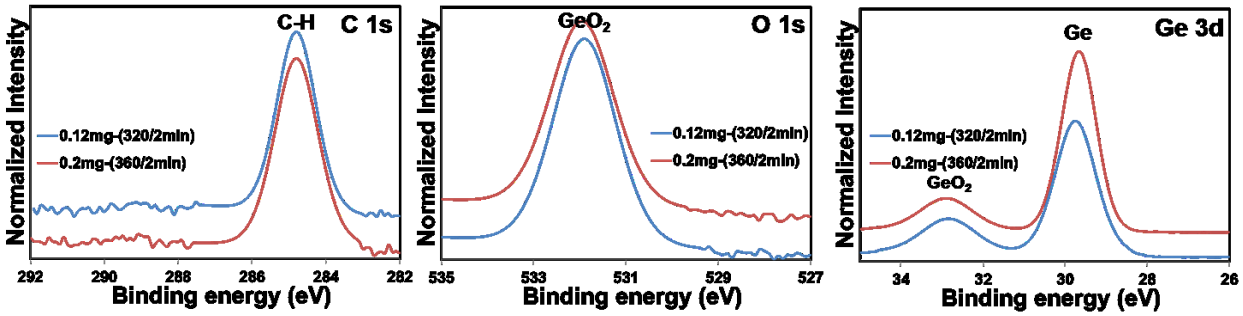

Figure 2.5: High resolution XPS spectra of C 1s, O 1s, and Ge 3d of as-synthesized 0.12mg-(320/2min) and 0.2mg-(360/2min) electrodes.

In the VLS mechanism, the reactants are introduced via the decomposition of GeH_4 gas and dissolve into the catalyst to form a molten gold-germanium alloy. Super-saturation of the molten droplet by Ge finally leads to the nucleation and axial growth of the nanowires. [73,74] The presence of liquid phase in the VLS growth mechanism requires the NWs growth to be carried out at temperatures above the eutectic melting point of the Au-Ge binary system (360 °C). [63] However, the eutectic temperature may shift to lower values in nanoscale binary systems due to the capillary effects, making it possible to grow Ge nanowires at temperatures below 360 °C. [60,64,75,76] Germanium nanowires grown at temperatures near the bulk eutectic are reportedly tapered with thicker root and thinner top. [60,74,76,77] Tapering growth of nanowires can occur via two possible mechanisms. One mechanism, first reported by Hannon et al., [78] is due to the Au catalyst mass loss during the VLS process at high temperatures. Catalyst migration through the surface of the nanowires will gradually consume the Au-containing alloy from the tip and make the droplet size smaller. This phenomenon induces further tapering growth of nanowires with non-uniform diameters. [76] Previous works on GeNWs [75,79] have shown that lowering the growth temperature can significantly decrease the surface diffusion of gold and the tapered growth of the NWs. Another mechanism can be the vapour-solid (VS) growth of the nanowires during the VLS

process, probably due to the direct deposition of Ge on their sidewalls. [71,64] At high temperatures, the decomposition of GeH_4 can take place without the presence of the Au nanoparticles, leading to the deposition of Ge nanoparticles. [64] The lower sections of the NWs are exposed to a Ge source for longer time, leading to increased radial growth at these parts and thus tapering and irregular morphology. Since the nanowires become amorphous in their delithiated state after the first lithiation, it is their geometrical (i.e. diameter, length) rather than their crystallographic features that are important for electrochemical performance.

Figure 2.6 shows the cyclic voltammetry (CV) curves for all the materials. The order of presentation is (a) 0.12mg-(320/2min), (b) 0.31mg-(320/5min), (c) 0.73mg-(320/10min), (d) 0.2mg-(360/2min), (e) 0.52mg-(360/5min), (f) 0.86mg-(360/10min). The peak currents increase with increasing temperature/growth time, consistent with increasing mass loading per unit area. While the absolute current varies due to the different mass loading for each growth condition, qualitative shape of the CV's is analogous for each specimen. In the first cycle, crystalline Ge is transformed into a series of Li_xGe_y alloys. Over the course of cycling, there are three highly broadened reduction peaks centered near 0.45, 0.3 and 0.1 V, and a sharp oxidation peak near 0.7 V vs. Li/Li^+. In the CV of the 0.12mg-(320/2min) specimen these peaks are highlighted by arrows. The reduction peak near 0.1 V has been associated with the crystallization to $Li_{15}Ge_4$, [80,81] with the reverse dissolution process having an oxidation peak too broad to detect separately. The remaining peaks may be attributed to compositional and structural (i.e. nearest neighbor arrangement) changes within the lithiating/delithiating Li_xGe_y. The associated phases would not be present on the equilibrium phase diagram and are yet to be well characterized. Similarly to the Li-Si system, the nucleation barrier for the intermediate Li-Ge phases of equilibrium crystal

structure is expected to be too high at ambient temperature. It is reasonable to argue that these intermediate Li-Ge phases should rather be amorphous, as they are known to be in Li-Si.

Figure 2.6 also shows the constant current (CC) voltage versus capacity curves for all the electrodes, in the order of (a) 0.12mg-(320/2min), (b) 0.31mg-(320/5min), (c) 0.73mg-(320/10min), (d) 0.2mg-(360/2min), (e) 0.52mg-(360/5min), (f) 0.86mg-(360/10min). Testing was performed at a current density of 138 mA g^{-1}. The CC curves are shown for cycles 1, 2, 10, 50 and 100. The potential versus capacity curves for all electrodes are quite similar both upon lithium insertion at first cycle and during subsequent cycling, with the mean positions of the sloping plateaus agreeing with the broadened peaks in the CV profiles. With increased cycling the plateau around 0.1 V decreases in capacity, indicating progressively less crystallization to $Li_{15}Ge_4$. The same has been observed for SiNWs [48,82,83] and may be related to the fact that during cycling, the nanowires disintegrate and the individual filaments are too small to accommodate a phase boundary.

The GeNWs specimens are amorphous in their delithiated state. This is demonstrated in Figure 2.7, which displays HRTEM micrographs and the corresponding Fast Fourier Transforms (FFTs) of two representative nanowires in the 0.12mg-(320°C/2min) arrays after their first delithiation.

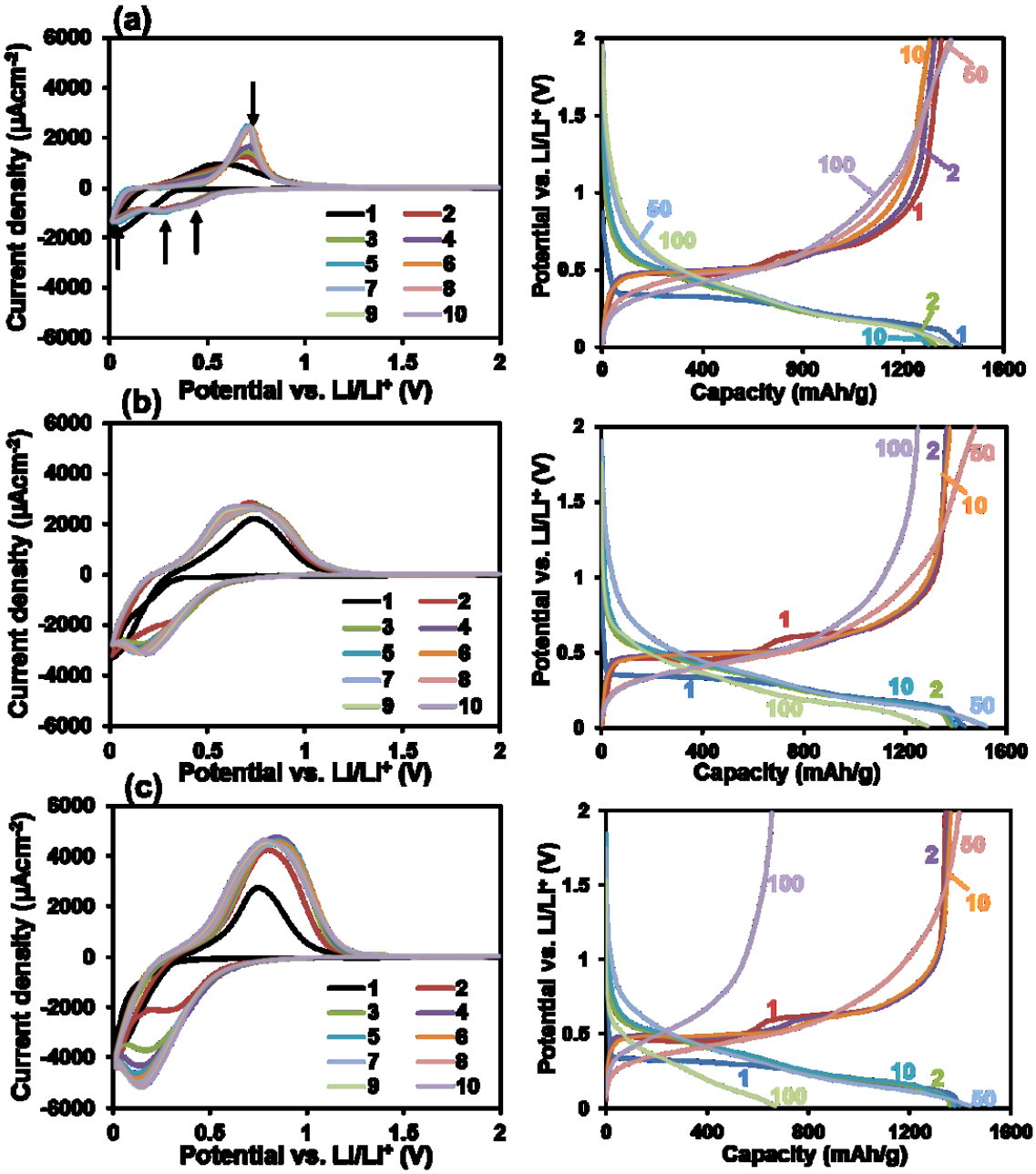

Figure 2.6: Cyclic voltammetry curves (left column) and constant-current voltage profiles (right column) of (a) 0.12mg-(320/2min), (b) 0.31mg-(320/5min), (c) 0.73mg-(320/10min), (d) 0.2mg-(360/2min), (e) 0.52-(360/5min), (f) 0.86-(360/10min) between 0 and 2V vs. Li/Li+ and 0.1C rate.

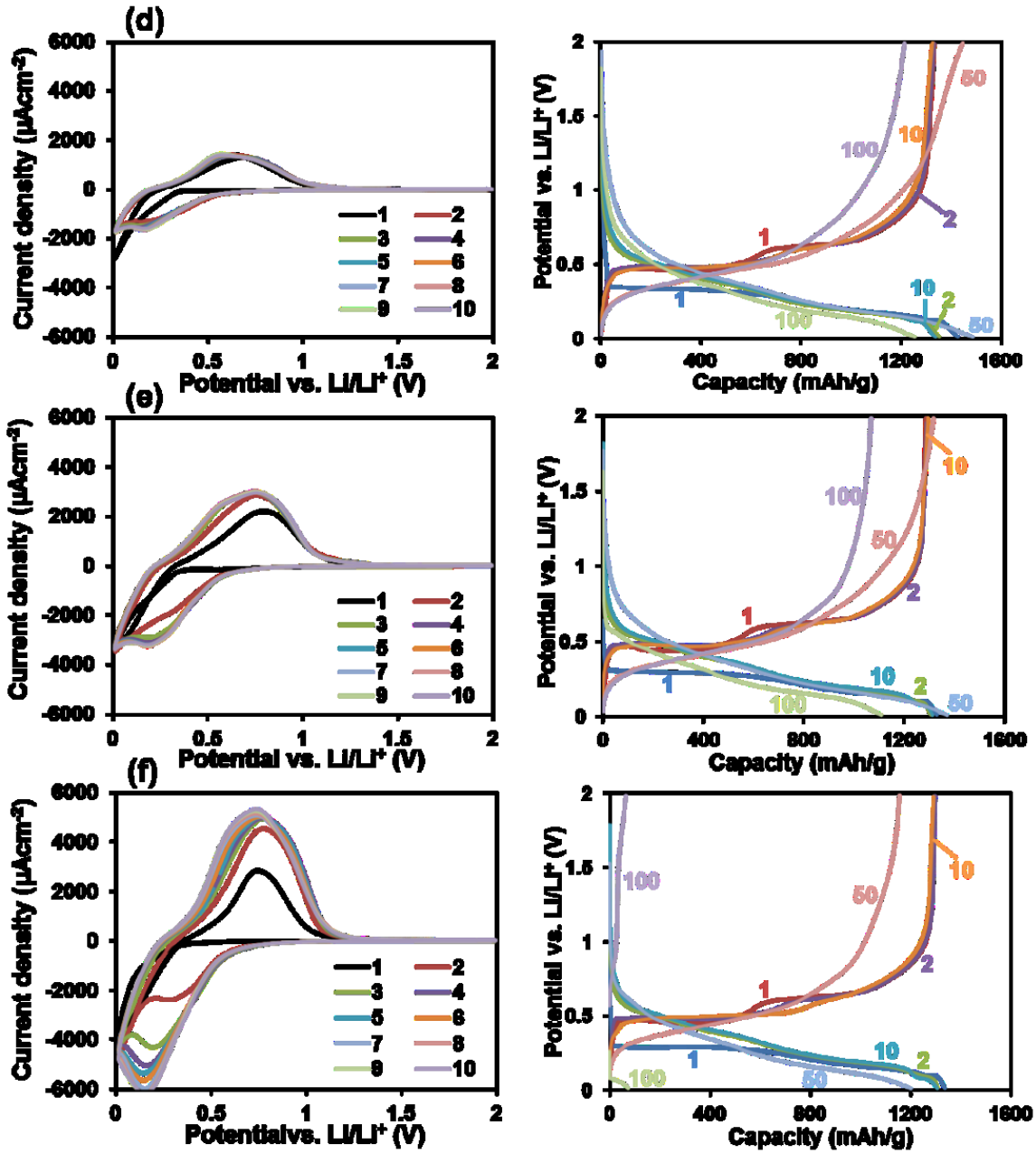

Figure 2.6, cont.: Cyclic voltammetry curves (left column) and constant-current voltage profiles (right column) of (d) 0.2mg-(360/2min), (e) 0.52-(360/5min), (f) 0.86-(360/10min) between 0 and 2V vs. Li/Li^+ and 0.1C rate.

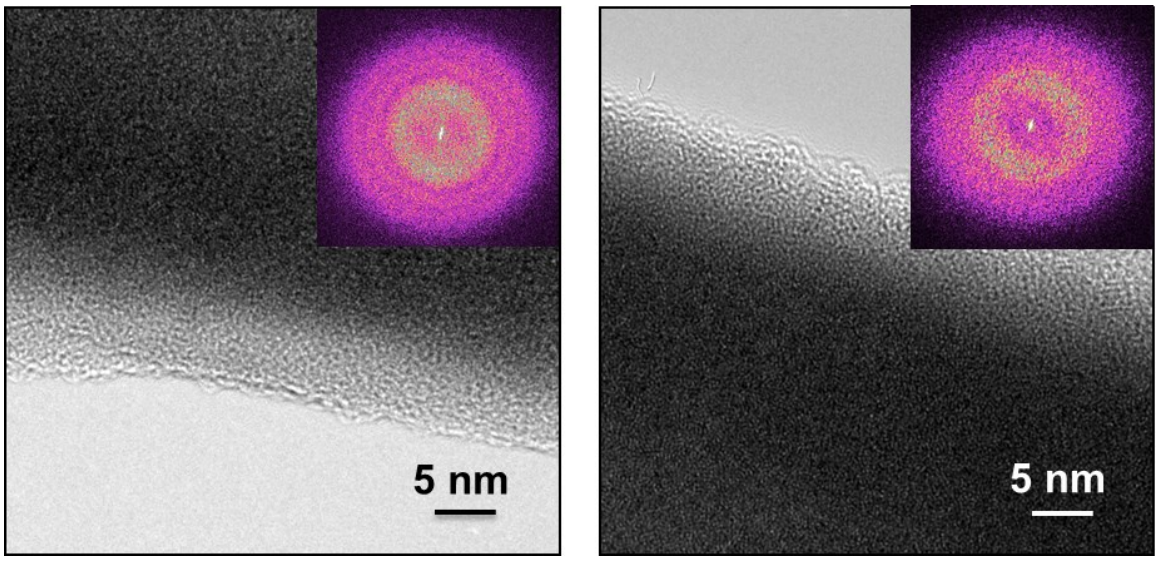

Figure 2.7: HRTEM and corresponding FFT images of representative sections of the 0.12mg-(320°C/2min) samples, after the first delithiation at 138 mA g^{-1}.

As shown in Table 2.2, the cycle 1 coulombic efficiency (CE) of the nanowires is effectively independent of the Ge nanowire and underlying Ge film dimensions, or of the mass loading. Figure 2.8 shows a plot of the first cycle charge and discharge capacities versus cycle number versus mass loading, tested at 138 mAh g^{-1}. This is in contrast to what is known for Si nanowires where cycle 1 CE substantially depends on the nanowire dimensions and size distribution, e.g. being in the range of 94 - 83% depending on the geometry. [82] Moreover, the cycle 1 CE values (94.8 - 96.8) are in the range, albeit on the upper end, of what has been previously reported for a variety of Ge - based nanostructures. This is illustrated in Table 2.3, where the literature reported cycle 1 CE values run as high as 98.6% down to the low 30's. Interestingly the same wide variation is reported in scientific literature for graphite-based LIB anodes, with cycle 1 CE values ranging anywhere from 100% (within measurement accuracy) to 74.5%. Table 2.4 shows a comparison of the initial CE for literature published graphite and

related materials - based LIB anodes. The associated references are provided in the supplemental.

For Si nanowires extensive modeling and experimental analysis shows that there is a critical diameter (200 - 300 nm range) above which the initially single or twinned single crystal nanowires are not able to withstand the initial lithiation stress and fracture catastrophically. [52,53,54,82,84-90] Full fracture during the first cycle then leads to immediate mechanical separation from the current collector. Any Li already present in the fractured wires is then not recovered, leading to a lowering of the CE. Thicker crystalline blanket films of Si are similarly less able to withstand the anisotropic initial lithiation stress associated with the ~ 300% volume expansion. [84,91-95] However it has been recently demonstrated that 300 nm scale and even micro scale Ge particles behave fundamentally differently, not fracturing upon the initial lithiation. [96] This was explained in terms of the crystallographic isotropy of the lithiation process, with the stress state in Ge being much more uniform than in Si. Our cycle 1 results support this conclusion. Moreover comparing the cycle 1 capacity loss for the Ge nanowires in this study to the cycle 1 capacity loss for Si nanowires, shows that the roughly 4 - 7 % cycle 1 capacity loss for all the conditions tested here is on par with the CE loss in the most optimized Si nanowire arrays, i.e. the ones that have diameters largely below the critical fracture dimension. [48,82,83,97,98] The electrodes with larger Si nanowire dimensions lose as much as 17% capacity at cycle 1.

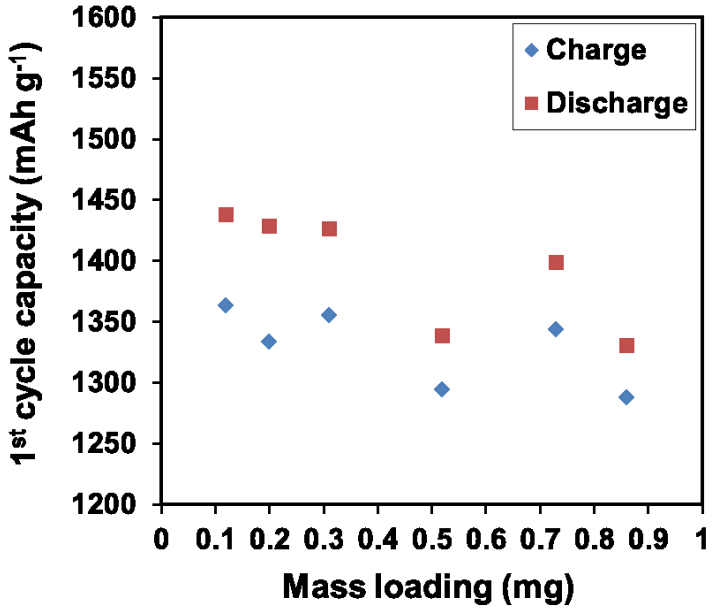

Figure 2.8: First cycle charge and discharge capacities versus mass loading, tested at 138 mAh g^{-1}.

Figure 2.9(a) shows a plot of the reversible capacity (measured at delithiation) of all the specimens as a function of cycle number, going up to 100 cycles. The results are plotted in the order of increasing mass loading, which clearly highlights the key trend in performance. The capacity of the highest mass loaded specimen, 0.86mg-(360/10min), decays to 5.6% of the initial capacity by cycle 100. The second highest mass loading specimen, 0.73mg-(320/10min), retains 50% of its initial capacity at cycle 100. With lower mass loadings, the capacity progressively improves until it reaches 98% of its initial value for 0.12mg-(320/2min). According to Figure 2.9(b) the cycling coulombic efficiency of the electrodes also decreases on the order of higher mass loading. As Table 2.2 indicates, the CE values at cycle 100 range from nearly 100% (99.8%) for the 0.12mg-(320/2min) specimen to 88.1% for 0.86mg-(360/10min). As demonstrated in Figure 2.9(c), the 320°C and the 360°C synthesis temperature cycling capacity retention and CE results converge into a fairly narrow single band of data when plotted against

the Ge mass loading. Figure 2.9(d) shows a rate capability comparison between 0.12mg-(320/2min) and 0.2mg-(360/2min). The drastic difference in the rate capability is likely a result of the longer Li diffusion distances associated with the larger diameters of the nanowires and the thicker Ge films in the 0.2mg-(360/2min) electrodes, as shown in Table 2.1. At high rates there is insufficient time to lithiate through the thickness and only a fraction of the theoretical capacity is achieved.

Table 2.2: The reversible capacity and coulombic efficiency of GeNWs after the 1st and 100th cycle, tested at 138 mA g^{-1}.

Electrode	Capacity ($mAh\ g^{-1}$)		Capacity retention (%)	Coulombic efficiency (%)	
	1st	100th	100th	1st	100th
0.12mg-(320/2min)	1438	1408	97.9	94.8	99.8
0.31mg-(320/5min)	1426	1300	91.1	95.0	96.9
0.73mg-(320/10min)	1398	691	49.4	96.1	98.1
0.2mg-(360/2min)	1429	1262	88.3	93.3	96.7
0.52mg-(360/5min)	1331	1120	84.1	96.7	96.3
0.86mg-(360/10min)	1338	75	5.6	96.8	88.1

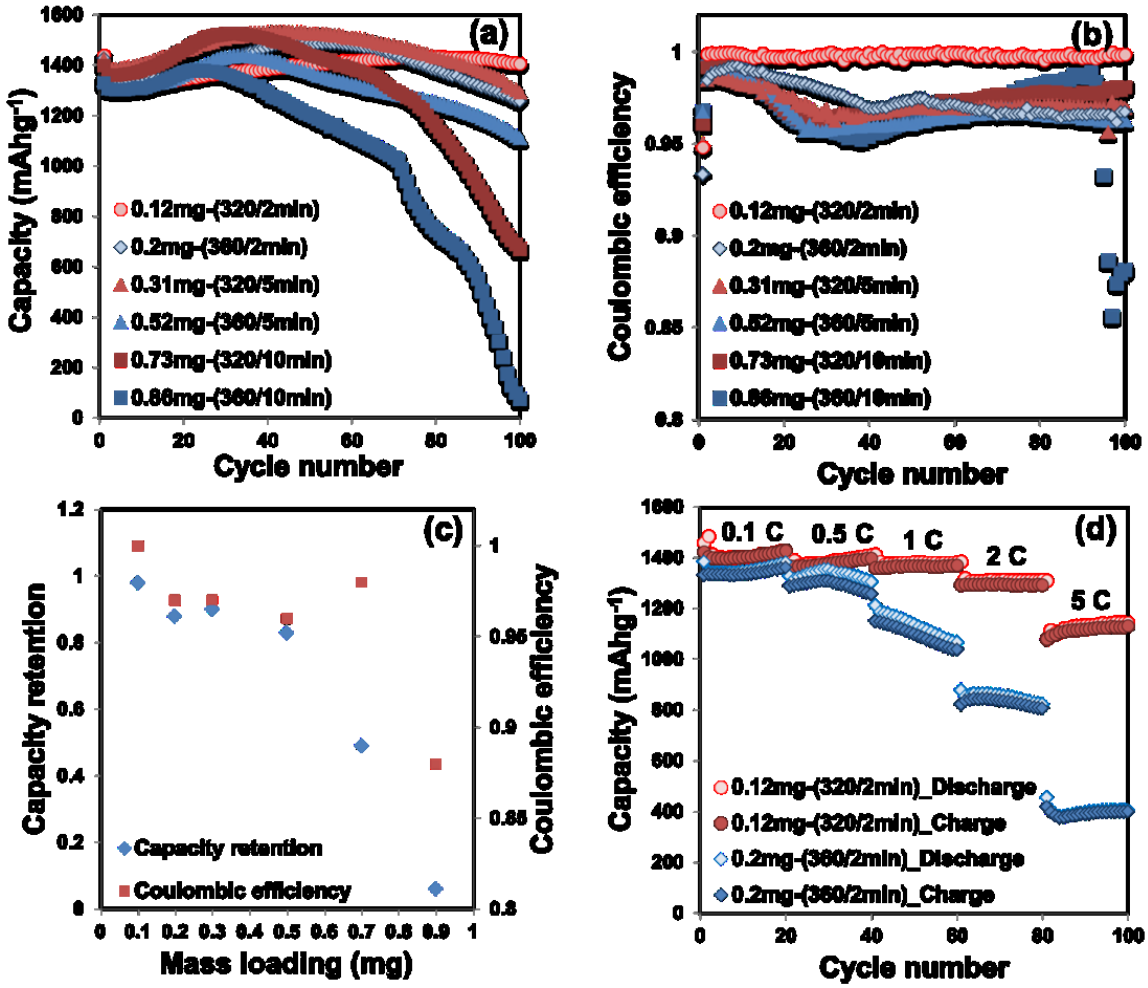

Figure 2.9: (a) Reversible capacity and (b) Coulombic efficiency (CE) versus cycle number, tested at 138 mA g^{-1}. (c) Cumulative comparison of capacity retention (at 100 cycles) and CE (at 50 cycles) versus mass loading. (d) Rate capability comparison of the 0.12 mg versus the 0.2 mg mass loading electrodes.

The role of electrode nanowire and parasitic film geometry on the cycling performance is highlighted in Figures 6. Figures 2.10(a) and 2.10(b) show the cycling capacity retention as a function of the mean nanowire diameter and of the Ge film thickness. These results highlight the strongest trends in performance. In both cases, there is a sharp monotonic decrease in the cycle 100 capacity with thicker nanowires and with thicker parasitic films. The role of nanowire (or nanoparticle) diameter and film thickness in establishing cycling electrochemical performance

has been treated extensively in scientific literature for the case of Si. [77,85] The general findings may be qualitatively applied for the case of Ge, which has received less attention to date, e.g. [17,18,52,99]. Both experimental and theoretical analysis of individual Si nanowires shows that with a larger diameter there is an increasing differential stress associated with the differential volume expansion due to lithiation, which proceeds radially inward. [52-54,89,100-103] Thicker films of Si will also be liable to fracture more both normal to the substrate plane [89] and in parallel to the substrate - film interface. [93-95] Since both Si and Ge cycled specimens are fully amorphous in their delithiated state, the behavior of Ge wires and films is expected to be qualitatively similar. This is different from cycle 1 lithiation, where Ge lithiates more isotropically than Si, as discussed. Figures 2.10(c) and 2.10(d) show the relationship between the coulombic efficiency (at cycle 50) and the wire diameter and film thickness. There again is a strong negative trend with progressively worsening CE with larger wire and film thicknesses. It is known that cycling CE is degraded by a combination of progressive SEI formation with every cycle and any loss of active material that contains Li. The second aspect may be understood in terms of a partially lithiated section of a nanowire fracturing from the assembly. As will be demonstrated in the next series of figures, at the thicker dimensions both mechanisms do contribute to the loss of CE. Figure 2.10(e) and 2.10(f) show the (less strong) trend of both capacity retention and CE decreasing with increasing mean nanowire length. This is presumably due to a higher statistical chance of catastrophic fracture occurring in longer wires.

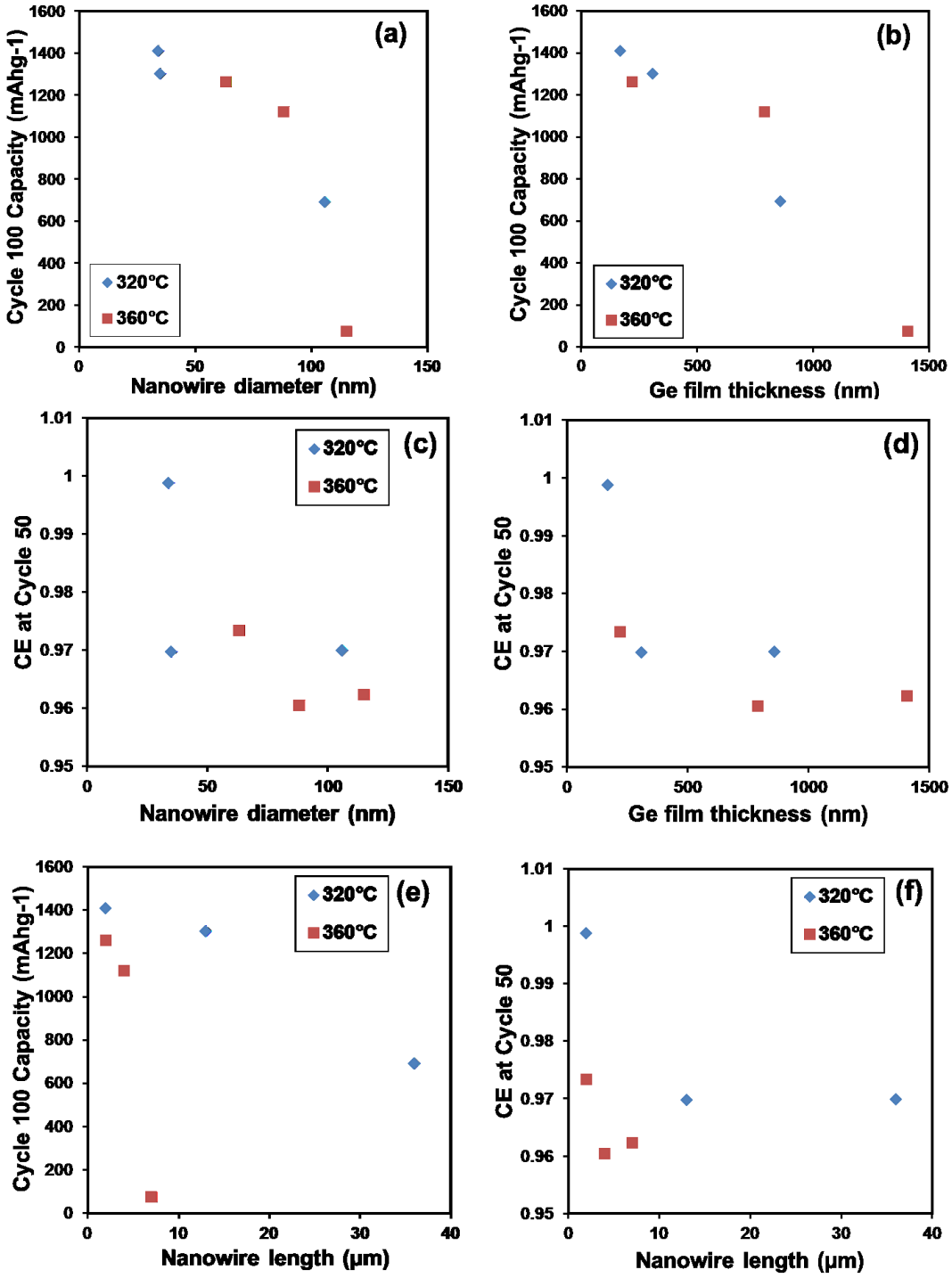

Figure 2.10: Cycle 100 capacity retention as a function of (a) the mean nanowire diameter, and (b) Ge parasitic film thickness. (c) – (d) CE (cycle 50) as a function of the mean nanowire diameter and parasitic Ge film thickness, (e) – (f) Cycling capacity retention (cycle 100) and CE (cycle 50) as a function of mean nanowire length.

Figure 2.11 compares the morphology of the post-cycled 0.12mg-(320/2min) and 0.2mg-(360/2min) specimens. With cycling, both electrodes show progressive lithiation-induced "stranding" of the nanowires, agreeing with previous reports on a range of cycled Ge nanostructures. [35,39,41]. Figure 2.12 shows the HAADF images and overlaid EELS maps of Ge, Li, C, and O for the post-100 cycles specimens in their delithiated state. For this analysis we found non-agglomerated nanowires, which were usually located near the top surface of the electrode. Figure 2.12(a) shows the 0.12mg-(320/2min) specimens, 2.12(b) shows the 0.73mg-(320/10min) specimens, and 2.12(c) shows the 0.2mg-(360/2min) specimens. In all three cases the microstructure of the individual cycled GeNWs is analogous: The nanowires have undergone substantial stranding parallel to their longitudinal direction and are now interspersed with visible porosity also running lengthwise (marked by arrows in the first panel of each series). The formation of nanopores during consecutive lithiation/delithiation has been previously reported for Ge nanowires. [52,58] Each of the newly exposed Ge surfaces is covered by SEI, which shows up as strong C, O and Li signals.

Figures 2.13 (a) and (b) show FIB cross-section SEM images of the post-100 cycles 0.73mg-(320/10min) and 0.86mg-(360/10min) electrodes. Near the current collector base (unlike near the top) the post-cycled nanowires are heavily agglomerated with SEI. There is much more cracking at the film - current collector interface in the 0.86mg-(360/10min) electrode. The stress driven failure of the bulk thin film has been discussed already. As the parasitic Ge film fractures during lithiation/delithiation cycling there is fresh Ge exposed to the electrolyte. This promotes more SEI growth, adding to the overall film stress and reducing the CE. The analytical maps shown in Figures 2.13(c) and 2.13(d) highlight the enhanced SEI formation near the nanowire – current collector interface, where a higher C and O signal is observed in that region. Note that

heavier elements in the steel substrate and the W in the "surface cap" have a large number of emission lines that overlap with any of the lighter elements and thus appear bright in all of the maps. The cycling-induced overgrowth of SEI on each nanowire also adds to the total film stress as there are regions where there is so much SEI that the nanowires actually fuse together to make a nanoporous composite.

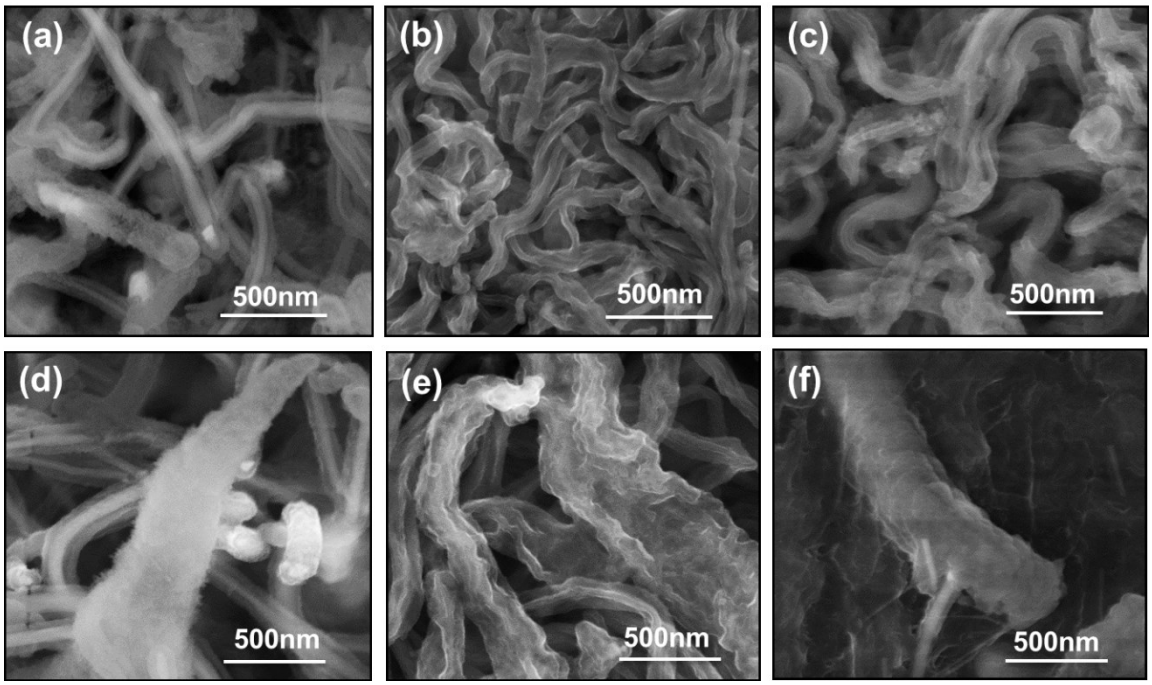

Figure 2.11: Plan-view SEM images of the cycled 0.12mg-(320/2min) for (a) 1 cycle, (b) 10 cycles, and (c) 100 cycles. Cycled 0.2mg-(360/2min) for (d) 1 cycle, (e) 10 cycles, and (f) 100 cycles.

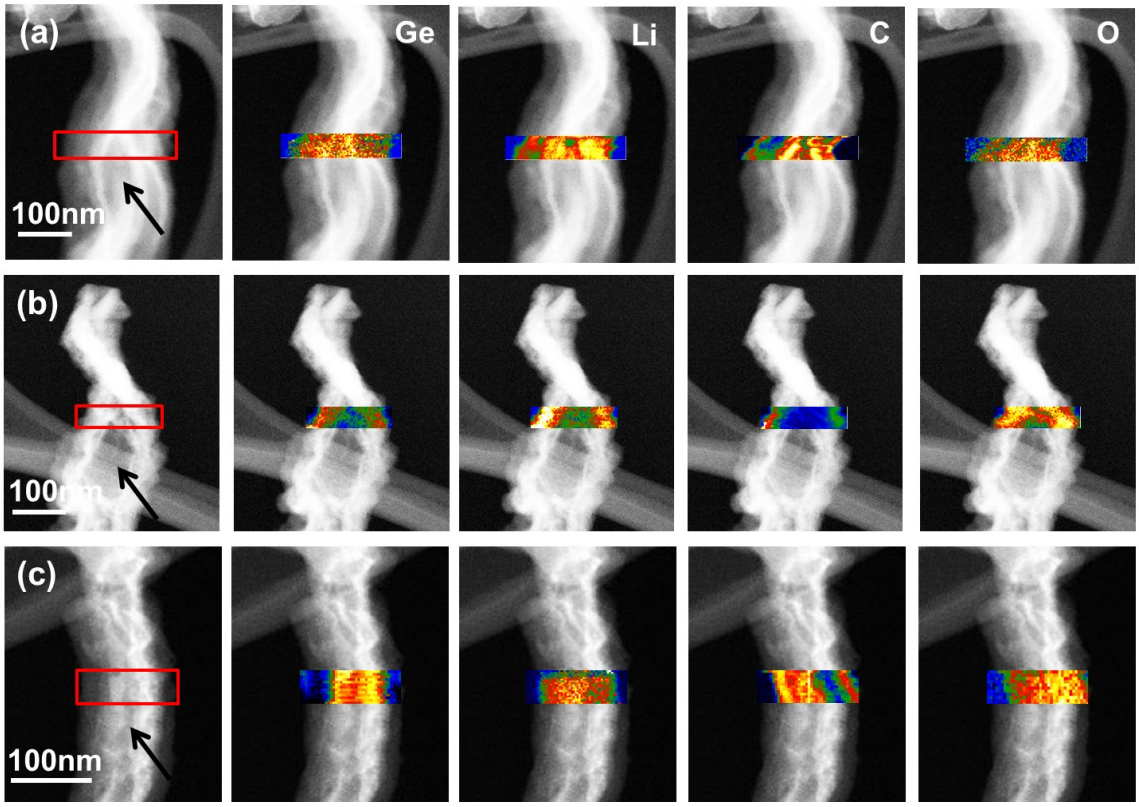

Figure 2.12: HAADF images and overlaid EELS maps of Ge, Li, C, and O for the post-100 cycles non-agglomerated nanowires located near the top surface of the electrode. (a) 0.12mg-(320/2min), (b) 0.73mg-(320/10min), and (c) 0.2mg-(360/2min). Arrows indicate the porosity near the center of the nanowires, which is running lengthwise.

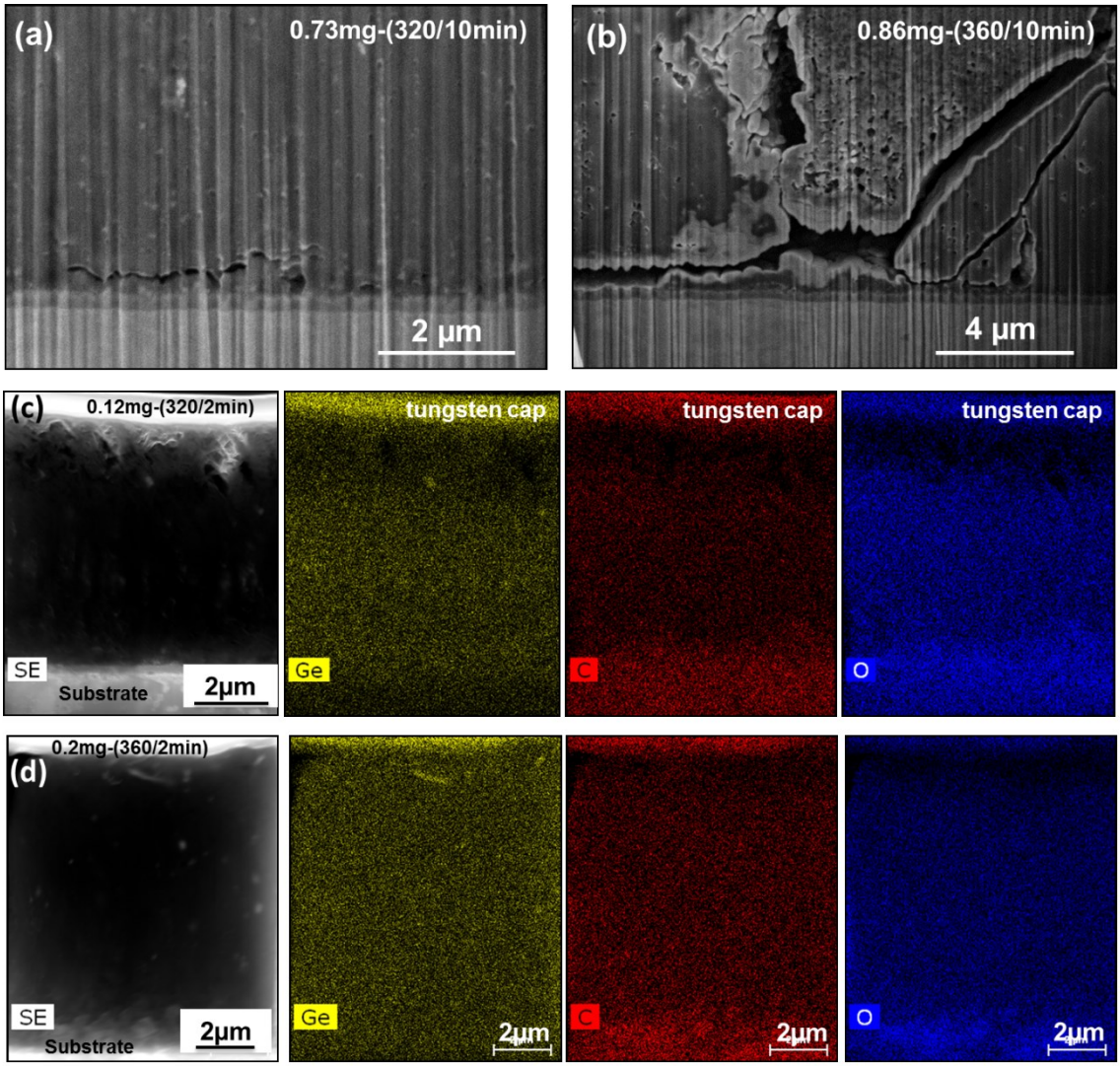

Figure 2.13: (a) and (b) FIB cross-sectional SEM images of the post-100 cycles 0.73mg-(320/10min) and 0.86mg-(360/10min) electrodes highlighting cracking at the current collector interface. (c) and (d) FIB cross-sectional images and elemental maps of germanium, carbon, and oxygen in the post-100 cycles 0.12mg-(320/2min) and 0.2mg-(360/2min) electrodes, highlighting enhanced SEI formation near the nanowire – current collector interface.

Electrochemical impedance spectroscopy (EIS) was employed to further understand the effect of mass loading on the cycling performance. Button cells (2 electrode) were tested in their delithiated state immediately after cycling. The Nyquist plots in Figure 2.14 are for the post-cycled electrodes, analyzed after cycle 10 and 100 delithiation. The insert in the figures shows

the equivalent circuits employed for modeling. The spectra exhibit well-defined features including a high-frequency depressed semi-circle, followed by a 45° sloped line in the low-frequency region of the spectra. The intercept of the spectra with the real part of the impedance axis shows equivalent series resistance (R_{es}) of the half-cell. The diameter of the high frequency semi-circle represents the interfacial charge transfer resistance (R_{ct}). [104] At cycle 10 the equivalent series and the charge transfer resistances of all the specimens are on par: R_{es} is 4, 5, 6 and 10 Ω for the 0.12mg-(320/2min), 0.2mg-(360/2min), 0.73mg-(320/10min), and 0.86 mg-(360/10min), respectively. In the same order R_{ct} is 90, 70, 80 and 60 Ω. Cycling has a negative effect on the higher mass loaded specimens. After 100 cycles R_{es} is 4.5, 5, 22 and 19 Ω for the 0.12mg-(320/2min), 0.2mg-(360/2min), 0.73mg-(320/10min), and 0.86 mg-(360/10min), respectively. R_{ct} increases to 80, 240, 180 and 340 Ω. The R_{ct} in post-cycled LIB anodes is known to be related to the charge transfer resistance through the multilayer SEI structure that forms initially upon cycle 1 lithiation and subsequently during cycling as fresh electrode material is exposed to the electrolyte. [108-105] For a given material, higher values of R_{ct} are considered synonymous with more interfaces that impede Li ion transfer into the bulk of the electrode, caused by a thicker SEI. [109] Since SEI irreversibly consumes Li during the reduction process, higher rates of SEI formation lead to lower CE values. Increasing R_{es} may be associated with a degradation of the electrical conductivity of the electrode materials, in addition to other factors such as an increasing interfacial electrical resistance, an increasing resistance of the current collector and of the electrochemical fixtures (the last two effects are unlikely). Having the specimens R_{ct} values be on-par at cycle 10 agrees with the results in Figure 2.9, showing on-par retained capacity and a similar CE at that point. After 100 cycles EIS results also agree with the

cycling data, with the CE at cycle 100 being the lowest for the 0.86 mg-(360/10min) specimens and the best for 0.12mg-(320/2min) electrodes.

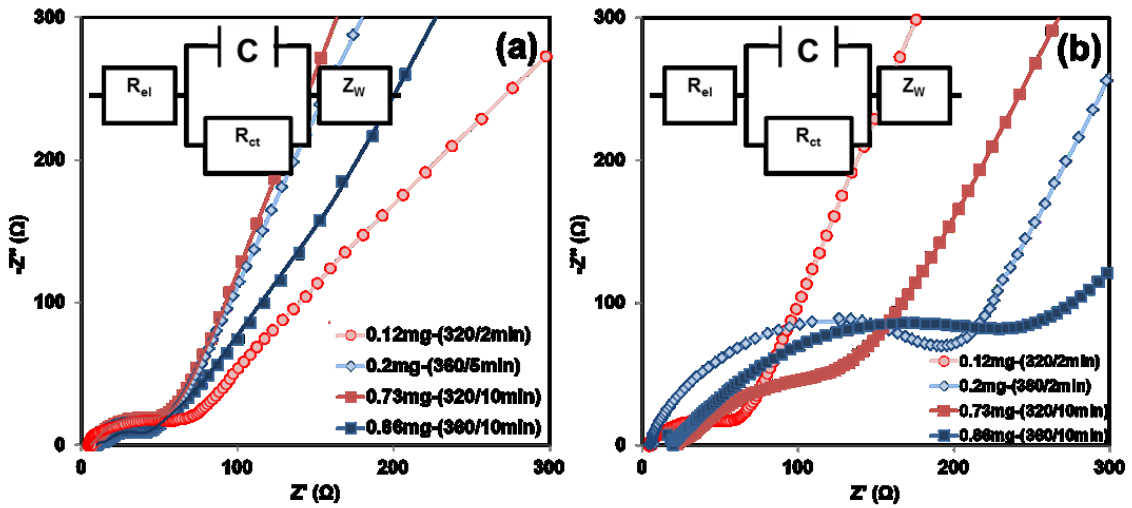

Figure 2.14: Electrochemical impedance (EIS) spectra of the GeNW electrodes after (a) 10 cycles, and (b) 100 cycles based on the equivalent circuit of two-electrode cells shown in the insets.

Figure 2.15 shows the XPS data for all the 0.12mg-(320/2min) electrodes after 1, 10 and 100 cycles. In the C 1s spectra, the shoulder off the main hydrocarbon signal at about 286 – 287 eV is attributed to polyethylene oxide (PEO). Lithium ethylene dicarbonate peak in C 1s appears as a broad shoulder at the binding energy of 288 – 289 eV. The peak associated with the Li_2CO_3 is located at about 290 eV. The O 1s spectra confirm the assignments made for C 1s spectra. The maximum intensity has a binding energy of around 531 – 532 eV for all the materials with a broad shoulder at higher binding energy of 532 – 534 eV. The main peak at ~ 531.5 eV represents Li_2CO_3 compound and the broad shoulder off the main carbonate signal at around 532 – 533 eV is associated with the PEO-like polymers and lithium ethylene dicarbonate. Presence of

fluorine and phosphorous in the SEI film suggests that degradation of $LiPF_6$ salt occurred during cycling. LiF is the main compound formed upon degradation of $LiPF_6$ through either a chemical decomposition or a reaction in presence of water. Li 1s spectra also have a main peak with a center at 55.2 eV, corresponding to Li_2CO_3, and a shoulder at about 56 eV, for LiF. Correspondingly, the main peak in F 1s spectra at ~ 684.5 eV is assigned to LiF. [110] The main signal in P 2p is from $Li_xPF_yO_z$, produced from the reaction of PF_5, formed upon chemical decomposition of $LiPF_6$ salt, with the contaminations and compounds in the cell. The XPS measurements indicate that the SEI layer consists mostly of Li_2CO_3 and LiF compounds. Li_2CO_3 is a well-known electrolyte reduction product, [111,112] the irreversible formation of which is associated with poor coulombic efficiency. Lithium carbonate, Li_2CO_3, and lithium ethylene dicarbonate, $(CH_2OCO_2Li)_2$, are produced upon the electrochemical reduction of EC solvent. Polyethylene oxide (PEO), $-(CH_2CH_2O)_n-$, is another product of EC degradation. [110] LiF is considered an electroless decomposition product of the $LiPF_6$ salt that forms over time. [107,113]

Figures 2.16 (a) – (c) show TOF-SIMS depth profiles of Li and Fe concentration through the thickness of three pure Ge films that were sputtered onto stainless steel substrates and then lithiated twice. The films had thicknesses of 150, 300 and 500 nm and were employed as model systems for understanding Li segregation in the Ge parasitic films present in the nanowire arrays. The Fe signal originates from the stainless steel current collector and demarcates the current collector – electrode interface. The profiles reveal Li segregation to the current collector interface in the 300 and 500 nm specimens, but with negligible segregation present in the 150 nm electrode. Segregation in the 500 nm specimen appears to be stronger than in the 300 nm film. The actual Li segregation profile in the 300 and 500 nm samples is probably sharper than what the TOF-SIMS results indicate, since the current collector's inherent roughness will smear the

through-thickness Fe and Li distributions. The results shown in Figure 2.16 are the first direct experimental confirmation of this phenomenon in regard to Ge electrodes. Our group has recently reported a similar interfacial segregation behavior of Na in Sn films deposited on stainless steel current collectors. [70] Authors reported calculations demonstrating that lithiation of pure Sn and Si leads to elastic softening of Sn-Li [114] and Si-Li [115] phases. Moreover failure of similar "film-on-support" type architectures (Si on Cu) has been both experimentally and theoretically proven to be critically related to a weakening of the mutual interface due to Li segregation and a change in bonding of the Si-Li alloy. [66] It is reasonable to expect an analogous effect for Ge-Li. Such phenomenology would further explain our electrochemical cycling and FIB results, where the array with a higher parasitic film thickness and hence with potentially more severe Li segregation is the one showing more interfacial fracture.

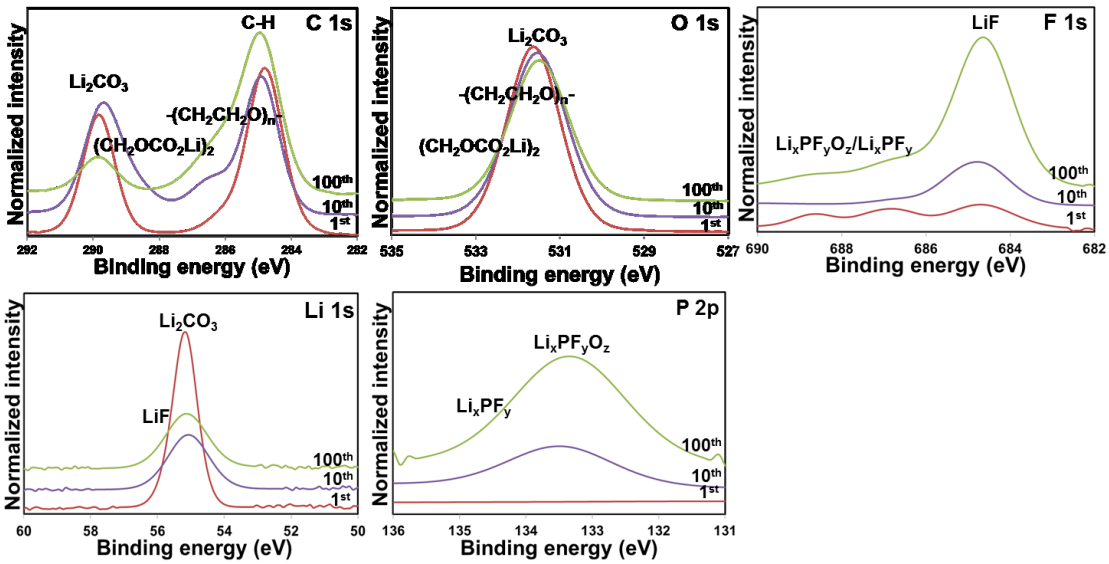

Figure 2.15: High resolution XPS spectra of 0.12mg-(320/2min) electrode after 1, 10 and 100 cycles.

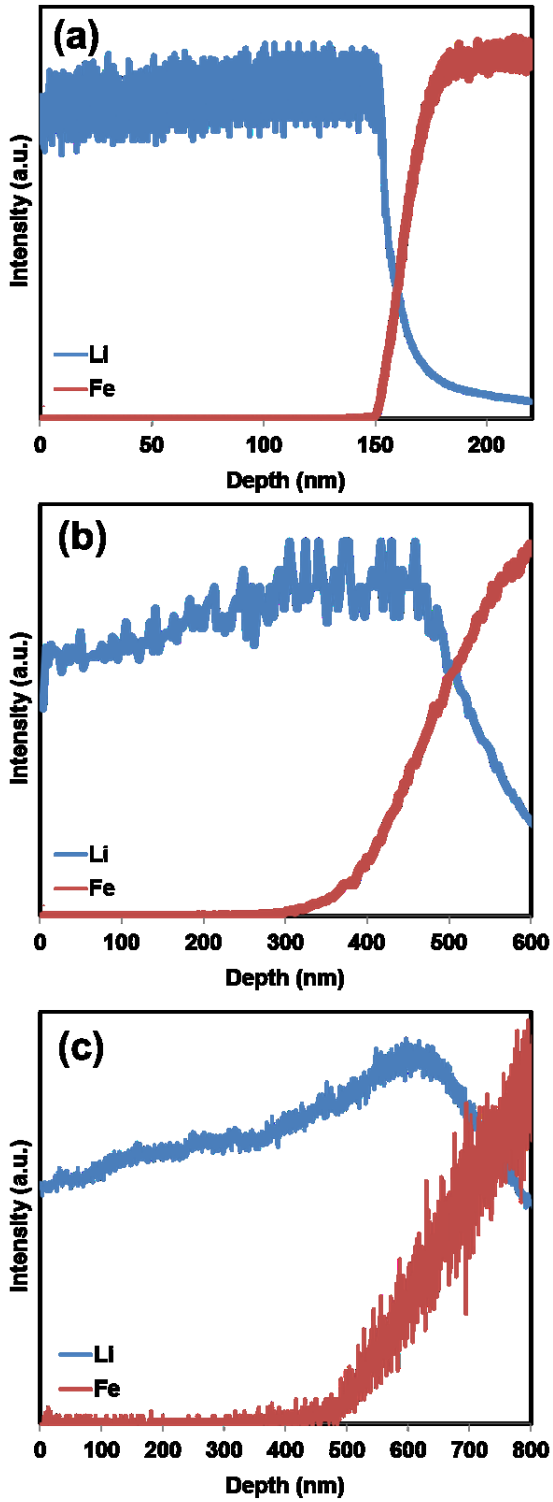

Figure 2.16: TOF-SIMS depth profiles of Li and Fe concentration through the thickness of lithiated Ge thin films on stainless steel substrate after the 2nd lithiation (a) – (c) 150, 300 and 500 nm Ge film thicknesses.

Finally, it is instructive to compare our electrochemical testing results with state-of-the-art scientific literature concerning the electrochemical performance of a range of Ge - based nanostructures employed as LIB anodes. Table 3 presents this comparison, highlighting the essential features of each material including the initial CE, reversible capacity at cycle 1 and at cycle 100, a steady-state cycling CE, and the high rate capability. In the Table, we present the performance of our best nanowire arrays, i.e. the ones with 0.12 mg mass loading. It may be observed that the performance of this electrode is among the best in all respects as compared to a range of advanced Ge - based nanostructures.

Table 2.3: A comparison of our best-performing electrode with previously published literature on Ge-based LIB anodes.

Electrodes	**Initial Coulombic Efficiency (%)**	**Cycling Capacity $mAhg^{-1}$ (current density)**		**Coulombic Efficiency (%) (current density)**		**Rate Capability $mAhg^{-1}$ (current density)**
		10st	**100th**	**10th**	**100th**	
0.12mg-(320°C/2min)	*95*	*1318*	*1405*	*99.85*	*99.86*	*1143*
	(138 mAg^{-1})	*(138 mAg^{-1})*	*(138 mAg^{-1})*	*(138 mAg^{-1})*	*(138 mAg^{-1})*	*(6900 mAg^{-1})*
	(0.1C)	*(0.1C)*	*(0.1C)*	*(0.1C)*	*(0.1C)*	*(5C)*
Alkanethiol-Passivated Ge Nanowires[41]	79.3	1300	1150	N/A	~99	733
	(0.1C)	(0.1C)	(0.1C)		(0.1C)	(6.5C)
Cu–Ge core–shell nanowire arrays [81]	80.1	~1538	NA	~97	NA	1103
	(800 mAg^{-1})	(800 mAg^{-1})		(800 mAg^{-1})		(6400 mAg^{-1})
Ge nanoparticle–multiwalled CNT [116]	~33	~875	~850	~94	~97	~500
	(1623 mAg^{-1})	(1623 mAg^{-1})	(1623 mAg^{-1})	(1623 mAg^{-1})	(1623 mAg^{-1})	(8115 mAg^{-1})

Carbon-Coated Ge Composite [11]	~90 (100 mAg^{-1})	~500 (100 mAg^{-1})	NA	NA	NA	NA
Graphene-Supported Germanium [42]	~81 (0.05C)	~830 (0.05C)	~375 (0.1C)	~93 (0.05C)	~98 (0.1C)	~100 (1C)
Entangled Ge NWs and Graphite Nanofibers[55]	78 (0.1C)	~ 1200 (0.1C)	NA	~99 (0.1C)		~600 (5C)
Ge Nanotubes [117]	76 (0.2C)	~900 (0.2C)	NA	~99 (0.2C)	NA	~650 (5C)
Ge nanowires-based carbon composite[38]	62.1 (160 mAg^{-1})	~900 (160 mAg^{-1})	NA	N/A	NA	~600 (800 mAg^{-1})
Germanium–Graphene composite [30]	~80 (400 mAg^{-1})	~800 (400 mAg^{-1})	~720 (400 mAg^{-1})	~99 (400 mAg^{-1})	~99.5 (400 mAg^{-1})	~300 (5000 mAg^{-1})
Ge Nanowires [40]	39 (0.05C)	~1150 (0.05C)	NA	~99 (0.05C)	NA	~600 (2C)
Ge nanowire anode sheathed with carbon [39]	91 (0.5C)	~800 (0.5C)	~700 (0.5C)	NA	~90 (0.5C)	~700 (6C=4800 mAg^{-1})
Ge Nanoparticles [23]	96	NA	NA	NA	NA	NA
Hybrid Ge Nanoparticle Single-Wall CNT [23]	~58 (50 mAg^{-1})	NA	NA	NA	NA	~300 (2000 mAg^{-1})
Ge@C Core−Shell Nanoparticles and Graphene Networks [10]	~52 (50 mAg^{-1})	~1025 (50 mAg^{-1})	NA	~99 (50 mAg^{-1})	NA	~380 (3600 mAg^{-1})
Mesoporous Ge [24]	43.8 (150 mAg^{-1})	~900 (150 mAg^{-1})	NA	NA	NA	NA

Ge Thin Films[18]	~33 (375 mAg^{-1})	~1700 (375 mAg^{-1})	NA	~97 (375 mAg^{-1})	NA	~500 (1000C)
Ion-beam Modified Ge Films [100]	98.4 (0.14C)	1300 (0.14C)	1342 (0.14C)	~96 (0.14C)	~95 (0.14C)	1000 (1.1C)
Solution-Grown Ge Nanowires [8]	~82 (0.1C)	~1300 (0.1C)	~ 1400 (0.1C)	~97 (0.1C)	~99 (0.1C)	~800 (5C)
p- and n-doped Ge Thin films [17]	NA	~750 (μAh cm^{-2}. μm^{-1}) (100 μA cm^{-2})	~800 (μAh cm^{-2}.μm^{-1}) (100 μA cm^{-2})	NA	NA	~800 ($mAh.g^{-1}$) (1600 μA cm^{-2})
Ge/Cu_3Ge/C composite[22]	78.4 (100 mAg^{-1})	~1000 (100 mAg^{-1})	NA	N/A	NA	NA
GeO_2/Ge/C Nanocomposite [5]	82 (0.05C)	~1800 (1C=2100 mAg^{-1})	NA	NA	NA	~1750 (5C)
Colloidal Tin-Germanium Nanorods [6]	~52 (1000 mAg^{-1})	~1650 (1000 mAg^{-1})	~1500 (1000 mAg^{-1})	NA	NA	~750 (4000 mAg^{-1})
GeO_2−SnCoC Composite[7]	80 (100 mAg^{-1})	~950 (300 mAg^{-1})	~800 (300 mAg^{-1})	NA	NA	~500 (1200 mAg^{-1})
Ge-Mo Composite [99]	91.6	~1050	~930	>99	97.2	NA
Ge Thin Film [99]	~95 (167 μA cm^{-2})	~1020 (167 μA cm^{-2})	~720 (167 μA cm^{-2})	~99 (167 μA cm^{-2})	~97 (167 μA cm^{-2})	NA
Ge Nanowire Arrays [35]	97 (0.5C)	~1120 (0.5C)	~1000 (0.5C)	~97 (0.5C)	~98 (0.5C)	~700 (5C)
Graphene-encapsulated	~53	~1400	NA	~96	NA	~1000

Ge Nanowires [36]						
Metallic Ge [36]	~72 (1C=1600mAg^{-1})	~300 (1600 mAg^{-1})	NA	~99 (1600 mAg^{-1})	NA	NA (8000 mAg^{-1})
Ge Thin Film [20]	~65 (0.1C)	~1250 (0.1C)	NA	NA	NA	~1130 (5C)
Sn–Ge alloy[32]	~78 (0.1C)	~1100 (0.1C)	NA	~98 (0.1C)	NA	~500 (5C)
GeS Nanocrystals [12]	78	~1375	~1250	~99	~99	~1125
GeO_2 Nanocrystals [12]	70	~1300	~1120	~99	~99	~625
Ge Nanocrystals [12]	70 (0.1C)	~1250 (0.1C)	~1125 (0.1C)	~98.5 (0.1C)	~98.5 (0.1C)	~600 (5C)
Ge microstructures [50]	NA	~550 (0.05C)	NA	~98 (0.05C)	NA	NA

Table 2.4: A comparison of the initial CE for literature published graphite and related materials - based LIB anodes.

Electrodes	Initial Coulombic Efficiency (%) (current rate or density)
Graphite flakes [118]	~92 (0.5C)
Graphite [119]	~93 (0.33C)
Graphite with Stabilized Lithium Metal Powder [119]	~100 (0.33C)
graphite/microfibrillated cellulose [120]	~75 (0.1C)
$ZnFe_2O_4$/Flake Graphite Composite [121]	87.7 (100 mA g^{-1})
Spherical natural graphite/ PVDF binder [122]	~88.5 (70 mAg^{-1})
Spherical natural graphite/ CMC/SBR binder [122]	~90.3 (70 mAg^{-1})
Spherical natural graphite/ PAA binder [122]	~90.1 (70 mAg^{-1})
Spherical natural flake graphite [123]	~91.3 (0.2C)
Mildly expanded graphite [123]	~84.4 (0.2C)
Ultrathin Graphite Foam [124]	~94 (190 mAg^{-1})
Graphene/SWNT Hybrid Foam [124]	~98 (190 mAg^{-1})
Pristine Graohite [125]	~94 (0.05C)
$Li_4Ti_5O_{12}$-coated Graphite [125]	~88 (0.05C)
Graphite-anchored lithium vanadium oxide [126]	79 (0.1C)
Graphite [127]	~89 (50 mAg^{-1})
graphite/silicon/graphene spherical composite [127]	~74.5 (50 mAg^{-1})
Commercial Graphite [128]	~86 (0.1C)

2.4. References

1 B. Dunn, H. Kamath and J. M. Tarascon, *Science*, 2011, **334**, 928-935.

2 J. M. Tarascon and M. Armand, *Nature*, 2001, **414**, 359-367.

3 P. V. Braun, J. Cho, J. H. Pikul, W. P. King and H. G. Zhang, *Curr. Opin. Solid State Mater. Sci.*, 2012, **16**, 186-198.

4 N. Ding, J. Xu, Y. X. Yao, G. Wegner, X. Fang, C. H. Chen and I. Lieberwirth, *Solid State Ionics*, 2009, **180**, 222-225.

5 K. H. Seng, M.-h. Park, Z. P. Guo, H. K. Liu and J. Cho, *Nano Lett.*, 2013, **13**, 1230-1236.

6 M. I. Bodnarchuk, K. V. Kravchyk, F. Krumeich, S. Wang and M. V. Kovalenko, *ACS nano*, 2014, **8**, 2360-2368.

7 B. Liu, A. Abouimrane, M. Balasubramanian, Y. Ren and K. Amine, *J. Phys. Chem. C*, 2014, **118**, 3960-3967.

8 A. M. Chockla, K. C. Klavetter, C. B. Mullins and B. A. Korgel, *Acs Appl. Mater. & Interfaces*, 2012, **4**, 4658-4664.

9 C. S. Fuller and J. C. Severiens, *Phys. Rev.*, 1954, **96**, 21-24.

10 D. J. Xue, S. Xin, Y. Yan, K. C. Jiang, Y. X. Yin, Y. G. Guo and L. J. Wan, *J. Am. Chem. Soc.*, 2012, **134**, 2512-2515.

11 S. Yoon, C. M. Park and H. J. Sohn, *Electrochem. Solid State Lett.*, 2008, **11**, A42-A45.

12 Y. J. Cho, H. S. Im, H. S. Kim, Y. Myung, S. H. Back, Y. R. Lim, C. S. Jung, D. M. Jang, J. Park, E. H. Cha, W. Il Cho, F. Shojaei and H. S. Kang, *Acs Nano*, 2013, **7**, 9075-9084.

13 Y.Yu, C.Yue, S. Sun, W. Lin, H. Su, B. Xu, J. Li, S. Wu, J. Li, and J. Kang, *ACS Appl. Mater. Interfaces*, 2014, **6(8)**, 5884-90.

14 C. K. Chan, H. L. Peng, G. Liu, K. McIlwrath, X. F. Zhang, R. A. Huggins and Y. Cui, *Nature Nanotech.*, 2008, **3**, 31-35.

15 A. H. Whitehead, K. Edstrom, N. Rao and J. R. Owen, *J. Power Sources*, 1996, **63**, 41-45.

16 L. Baggetto, E. J. M. Hensen and P. H. L. Notten, *Electrochimica Acta*, 2010, **55**, 7074-7079.

17 B. Laforge, L. Levan-Jodin, R. Salot and A. Billard, *J. Electrochem. Soc.*, 2008, **155**, A181-A188.

18 J. Graetz, C. C. Ahn, R. Yazami and B. Fultz, *J. Electrochem. Soc.*, 2004, **151**, A698-A702.

19 N. G. Rudawski, B. L. Darby, B. R. Yates, K. S. Jones, R. G. Elliman and A. A. Volinsky, *Appl. Phys. Lett.*, 2012, **100**.

20 P. R. Abel, A. M. Chockla, Y.-M. Lin, V. C. Holmberg, J. T. Harris, B. A. Korgel, A. Heller and C. B. Mullins, *Acs Nano*, 2013, **7**, 2249-2257.

21 X. Liu, J. Zhao, J. Hao, B.-L. Su and Y. Li, *J. Mater. Chem. A*, 2013, **1**, 15076-15081.

22 Y. Hwa, C. M. Park, S. Yoon and H. J. Sohn, *Electrochimica Acta*, 2010, **55**, 3324-3329.

23 R. A. DiLeo, S. Frisco, M. J. Ganter, R. E. Rogers, R. P. Raffaelle and B. J. Landi, *J. Phys. Chem. C*, 2011, **115**, 22609-22614.

24 L. C. Yang, Q. S. Gao, L. Li, Y. Tang and Y. P. Wu, *Electrochem. Commun.*, 2010, **12**, 418-421.

25 Y. Son, M. Park, J. S. Lee, J. H. Jang, Y. Kim and J. Cho, *Nano Lett.*, 2014, **14**, 1005-1010.

26 T. Song, Y. Jeon, M. Samal, H. Han, H. Park, J. Ha, D. K. Yi, J.-M. Choi, H. Chang, Y.-M. Choi and U. Paik, *Energ. Environ. Sci.*, 2012, **5**, 9028-9033.

27 W. Li, Z. Yang, J. Cheng, X. Zhong, L. Gu, Y. Yu, *Nanoscale*, 2014, **6**, 4532.

28 W. Li, J. Zheng, T. Chen, T. Wang, X. Wang and X. Li, *Chem. Commun.*, 2014, **50**, 2052-2054.

29 C. Zhong, J.-Z. Wang, X.-W. Gao, D. Wexler and H.-K. Liu, *J. Mater. Chem. A*, 2013, **1**, 10798-10804.

30 J.-G. Ren, Q-H. Wu, H. Tang, G. Hong, W. Zhang, and S.-T. Lee*, J. Mater. Chem. A*, 2013, **1**, 1821.

31 M. H. Park, Y. Cho, K. Kim, J. Kim, M. L. Liu and J. Cho, *Angewandte Chemie-International Edition*, 2011, **50**, 9647-9650.

32 S. Fan, L. Y. Lim, Y. Y. Tay, S. S. Pramana, X. Rui, M. K. Samani, Q. Yan, B. K. Tay, M. F. Toney and H. H. Hng, *J. Mater. Chem. A*, 2013, **1**, 14577-14585.

33 Y. J. Cho, C. H. Kim, H. S. Im, Y. Myung, H. S. Kim, S. H. Back, Y. R. Lim, C. S. Jung, D. M. Jang, J. Park, S. H. Lim, E. H. Cha, K. Y. Bae, M. S. Song and W. Il Cho, *Phys. Chem. Chem. Phys.*, 2013, **15**, 11691-11695.

34 T. Song, H. Cheng, K. Town, K. Park, R. W. Black, S. Lee, W. Park, Y. Huang, J. A. Rogers, L. F. Nazar, and U. Paik. *Adv. Funct. Mater.,* 2014, **24**, 1458–1464.

35 T. Kennedy, E. Mullane, H. Geaney, M. Osiak, C. O'Dwyer and K. M. Ryan, *Nano Lett.*, 2014, **14**, 716-723.

36 C. Wang, J. Ju, Y. Yang, Y. Tang, J. Lin, Z. Shi, R. P. S. Han and F. Huang, *J. Mater. Chem. A*, 2013, **1**, 8897-8902.

37 D. D. Vaughn and R. E. Schaak, *Chem. Soc. Rev.*, 2013, **42**, 2861-2879.

38 L. P. Tan, Z. Y. Lu, H. T. Tan, J. X. Zhu, X. H. Rui, Q. Y. Yan and H. H. Hng, *J. Power Sources*, 2012, **206**, 253-258.

39 M. H. Seo, M. Park, K. T. Lee, K. Kim, J. Kim and J. Cho, *Energ. Environ. Sci.*, 2011, **4**, 425-428.

40 C. K. Chan, X. F. Zhang and Y. Cui, *Nano Lett.*, 2008, **8**, 307-309.

41 F. W. Yuan, H. J. Yang and H. Y. Tuan, *Acs Nano*, 2012, **6**, 9932-9942.

42 A. M. Chockla, M. G. Panthani, V. C. Holmberg, C. M. Hessel, D. K. Reid, T. D. Bogart, J. T. Harris, C. B. Mullins and B. A. Korgel, *J. Phys. Chem. C*, 2012, **116**, 11917-11923.

43 Y. Liu, S. Zhang and T. Zhu, *Chem.Electro. Chem.,* 2014*,* **1**, 817.

44 B. A. Korgel, *J. Phys. Chem. Lett.*, 2014, **5**, 749-750.

45 W. J. Zhang, *J. Power Sources*, 2011, **196**, 13-24.

46 D. Aurbach, B. Markovsky, G. Salitra, E. Markevich, Y. Talyossef, M. Koltypin, L. Nazar, B. Ellis and D. Kovacheva, *J. Power Sources*, 2007, **165**, 491-499.

47 Y. Matsumura, S. Wang and J. Mondori, *J. Electrochem. Soc.*, 1995, **142**, 2914-2918.

48 A. Kohandehghan, P. Kalisvaart, M. Kupsta, B. Zahiri, B. S. Amirkhiz, Z. P. Li, E. L. Memarzadeh, L. A. Bendersky and D. Mitlin, *J. Mater. Chem. A*, 2013, **1**, 1600-1612.

49 H. Wu, G. Chan, J. W. Choi, I. Ryu, Y. Yao, M. T. McDowell, S. W. Lee, A. Jackson, Y. Yang, L. B. Hu and Y. Cui, *Nature Nanotech.*, 2012, **7**, 309-314.

50 B. R. Long, J. L. Goldman, R. G. Nuzzo and A. A. Gewirth, *J. Solid State Electrochem.*, 2013, **17**, 3015-3020.

51 Y. Liu, X. H. Liu, B.-M. Nguyen, J. Yoo, J. P. Sullivan, S. T. Picraux, J. Y. Huang and S. A. Dayeh, *Nano Lett.*, 2013, **13**, 4876-4883.

52 X. H. Liu, Y. Liu, A. Kushima, S. L. Zhang, T. Zhu, J. Li and J. Y. Huang, *Adv. Energy Mater.*, 2012, **2**, 722-741.

53 X. H. Liu and J. Y. Huang, *Energ. Environ. Sci.*, 2011, **4**, 3844-3860.

54 X. H. Liu, H. Zheng, L. Zhong, S. Huan, K. Karki, L. Q. Zhang, Y. Liu, A. Kushima, W. T. Liang, J. W. Wang, J. H. Cho, E. Epstein, S. A. Dayeh, S. T. Picraux, T. Zhu, J. Li, J. P. Sullivan, J. Cumings, C. S. Wang, S. X. Mao, Z. Z. Ye, S. L. Zhang and J. Y. Huang, *Nano Lett.*, 2011, **11**, 3312-3318.

55 S. H. Woo, S. J. Choi, J. H. Park, W. S. Yoon, S. W. Hwang and D. Whang, *J. Electrochem. Soc.*, 2013, **160**, A112-A116.

56 Y. Yao, M. T. McDowell, I. Ryu, H. Wu, N. A. Liu, L. B. Hu, W. D. Nix and Y. Cui, *Nano Letters*, 2011, **11**, 2949-2954.

57 N. S. Choi, Y. Yao, Y. Cui and J. Cho, *Journal of Materials Chemistry*, 2011, **21**, 9825-9840.

58 X. H. Liu, S. Huang, S. T. Picraux, J. Li, T. Zhu and J. Y. Huang, *Nano Lett.*, 2011, **11**, 3991-3997.

59 J. H. Cho and S. T. Picraux, *Nano Lett.*, 2013, **13**, 5740-5747.

60 H. Adhikari, A. F. Marshall, C. E. D. Chidsey and P. C. McIntyre, *Nano Lett.*, 2006, **6**, 318-323.

61 A. Rath, J. K. Dash, R. R. Juluri, A. Ghosh, T. Grieb, M. Schowalter, F. F. Krause, K. Muller, A. Rosenauer and P. V. Satyam, *Cryst. Eng. Comm*, 2014, **16**, 2486-2490.

62 J. L. Taraci, T. Clement, J. W. Dailey, J. Drucker and S. T. Picraux, *Nucl. Instrum. Methods Phys. Res., Sect. B -Beam Interactions with Materials and Atoms*, 2006, **242**, 205-208.

63 H. Adhikari, P. C. McIntyre, A. F. Marshall and C. E. D. Chidsey, *J. Appl. Phys.*, 2007, **102**.

64 M. Simanullang, K. Usami, T. Kodera, K. Uchida and S. Oda, *Jpn. J. Appl. Phys.*, 2011, **50**.

65 Y. Sierra-Sastre, S. A. Dayeh, S. T. Picraux and C. A. Batt, *Acs Nano*, 2010, **4**, 1209-1217.

66 M. E. Stournara, X. Xiao, Y. Qi, P. Johari, P. Lu, and B. W. Sheldon, *Nano Lett.*, 2013, **13**, 4759−4768.

67 D. Santhanagopalan, D. Qian, T. McGilvray, Z. Y. Wang, F. Wang, F. Camino, J. Graetz, N. Dudney and Y. S. Meng, *Journal of Physical Chemistry Letters*, 2014, **5**, 298.

68 J.-T. Li, J. Swiatowska, A. Seyeux, L. Huang, V. Maurice, S.-G. Sun and P. Marcus, *Journal of Power Sources*, 2010, **195**, 8251.

69 J.-T. Li, J. Swiatowska, V. Maurice, A. Seyeux, L. Huang, S.-G. Sun and P. Marcus, *Journal of Physical Chemistry C*, 2011, **115**, 7012.

70 B.Farbod, C. Kai, W. P. Kalisvaart, M. Kupsta, B. Zahiri, A. Kohandehghan, E. Memarzadeh, Z. Li, E. J. Luber, and D. Mitlin, ACS Nano, 2014, DOI: 10.1021/nn4063598.

71 H. Adhikari, A. F. Marshall, I. A. Goldthorpe, C. E. D. Chidsey and P. C. McIntyre, *ACS Nano*, 2007, **1**, 415-422.

72 L. Zhang, C. M. B. Holt, E. Luber, B. C. Olsen, H. Wang, M. Danaie, X. Cui, X. Tan, V. Lui, W. P. Kalisvaart, and D. Mitlin, *J. Phys. Chem. C,* 2011, **115**, 24381–24393.

73 C. O'Regan, S. Biswas, N. Petkov and J. D. Holmes, *J. Mater. Chem. C*, 2014, **2**, 14-33.

74 C. Renard, R. Boukhicha, C. Gardes, F. Fossard, V. Yam, L. Vincent, D. Bouchier, S. Hajjar, J. L. Bubendorff, G. Garreau and C. Pirri, *Thin Solid Films*, 2012, **520**, 3314-3318.

75 T. I. Kamins, X. Li and R. S. Williams, *Nano Lett.*, 2004, **4**, 503-506.

76 S. Kodambaka, J. Tersoff, M. C. Reuter and F. M. Ross, *Science*, 2007, **316**, 729-732.

77 C. B. Li, K. Usami, H. Mizuta and S. Oda, *J. Appl. Phys.*, 2009, **106**.

78 J. B. Hannon, S. Kodambaka, F. M. Ross and R. M. Tromp, *Nature*, 2006, **440**, 69-71.

79 J. H. Kim, S. R. Moon, Y. Kim, Z. G. Chen, J. Zou, D. Y. Choi, H. J. Joyce, Q. Gao, H. H. Tan and C. Jagadish, *Nanotech.*, 2012, **23**.

80 L. Baggetto and P. H. L. Notten, *J. Electrochem. Soc.*, 2009, **156**, A169-A175.

81 J. Z. Wang, N. Du, H. Zhang, J. X. Yu and D. R. Yang, *J. Mater. Chem.*, 2012, **22**, 1511-1515.

82 E. L. Memarzadeh, W. P. Kalisvaart, A. Kohandehghan, B. Zahiri, C. M. B. Holt and D. Mitlin, *J. Mater. Chem.*, 2012, **22**, 6655-6668.

83 E.L. Memarzadeh, P. Kalisvaart, K. Cui, A. Kohandehghan, M. Kupsta, B. Olsen, D. Mitlin, *Phys. Chem. Chem. Phys.*, 2013, p. **13646**.

84 A. Mukhopadhyay and B. W. Sheldon, *Progress in Mater. Sci.,* 2014, **63**, 58–116.

85 X. Su, Q. L. Wu, J. C. Li, X. C. Xiao, A. Lott, W. Q. Lu, B. W. Sheldon and J. Wu, *Adv. Energ. Mater.*, 2014, **4**.

86 X. H. Liu, L. Zhong, S. Huang, S. X. Mao, T. Zhu and J. Y. Huang, *Acs Nano*, 2012, **6**, 1522-1531.

87 H. Kim, M. Seo, M. H. Park and J. Cho, *Angewandte Chemie-International Edition*, 2010, **49**, 2146-2149.

88 M. T. McDowell, S. W. Lee, J. T. Harris, B. A. Korgel, C. M. Wang, W. D. Nix and Y. Cui, *Nano Lett.*, 2013, **13**, 758-764.

89 I. Ryu, J. W. Choi, Y. Cui and W. D. Nix, *J. Mech. Phys. Solids*, 2011, **59**, 1717-1730.

90 S. W. Lee, M. T. McDowell, L. A. Berla, W. D. Nix and Y. Cui, *Proceedings of the National Academy of Sciences of the United States of America*, 2012, **109**, 4080-4085.

91 X. Xiao, P. Liu, M. W. Verbrugge, H. Haftbaradaran and H. Gao, *J. Power Sources*, 2011, **196**, 1409-1416.

92 S. K. Soni, B. W. Sheldon, X. C. Xiao and A. Tokranov, *Scripta Materialia*, 2011, **64**, 307-310.

93 H. Haftbaradaran, X. C. Xiao, M. W. Verbrugge and H. J. Gao, *J. Power Sources*, 2012, **206**, 357-366.

94 H. Haftbaradaran and H. J. Gao, *Appl. Phys. Lett.*, 2012, **100**.

95 H. Haftbaradaran, X. C. Xiao and H. J. Gao, *Modell. Simul. Mater. Sci. Eng.*, 2013, **21**.

96 W. Liang, H. Yang, F. Fan, Y. Liu, X. H. Liu, J. Y. Huang, T. Zhu and S. Zhang, *Acs Nano*, 2013, **7**, 3427-3433.

97 E. M. Lotfabad, P. Kalisvaart, A. Kohandehghan, K. Cui, M. Kupsta, B. Farbod and D. Mitlin, *J. Mater. Chem. A*, 2014, **2**, 2504-2516.

98 A. Kohandehghan, P. Kalisvaart, K. Cui, M. Kupsta, E. Memarzadeh and D. Mitlin, *J. Mater. Chem. A*, 2013, **1**, 12850-12861.

99 C. M. Hwang and J. W. Park, *Thin Solid Films*, 2010, **518**, 6590-6597.

100 S. T. Boles, A. Sedlmayr, O. Kraft and R. Monig, *Appl. Phys. Lett.*, 2012, **100**.

101 T. T. Fister, J. L. Goldman, B. R. Long, R. G. Nuzzo, A. A. Gewirth and P. A. Fenter, *Appl. Phys. Lett.*, 2013, **102**.

102 S. P. V. Nadimpalli, V. A. Sethuraman, S. Dalavi, B. Lucht, M. J. Chon, V. B. Shenoy and P. R. Guduru, *J. Power Sources*, 2012, **215**, 145-151.

103 R. Deshpande, Y. T. Cheng and M. W. Verbrugge, *J. Power Sources*, 2010, **195**, 5081-5088.

104 M. D. Levi and D. Aurbach, J. *Phys. Chem. B*, 1997, **101**, 4630-4640.

105 V. Etacheri, U. Geiger, Y. Gofer, G. A. Roberts, I. C. Stefan, R. Fasching and D. Aurbach, *Langmuir*, 2012, **28**, 6175-6184.

106 E. Pollak, G. Salitra, V. Baranchugov and D. Aurbach, *J. Phys. Chem. C*, 2007, **111**, 11437-11444.

107 K. Xu, *Chem. Rev.*, 2004, **104**, 4303-4417.

108 J. C. Guo, A. Sun, X. L. Chen, C. S. Wang and A. Manivannan, *Electrochimica Acta*, 2011, **56**, 3981-3987.

109 N. Ding, J. Xu, Y. X. Yao, G. Wegner, I. Lieberwirth and C. H. Chen, *J. Power Sources*, 2009, **192**, 644-651.

110 B. Philippe, R. Dedryvère, M. Gorgoi, H. Rensmo, D. Gonbeau, and K. Edström. Chem. Mater., 2013, **25**, 394–404.

111 D. Aurbach, B. Markovsky, M. D. Levi, E. Levi, A. Schechter, M. Moshkovich and Y. Cohen, *J. Power Sources*, 1999, **81**, 95-111.

112 K. W. Schroder, H. Celio, L. J. Webb and K. J. Stevenson, *J. Phys. Chem. C*, 2012, **116**, 19737-19747.

113 D. Aurbach, E. Zinigrad, Y. Cohen and H. Teller, *Solid State Ionics*, 2002, **148**, 405-416.

114 M. E. Stournara, P. R. Guduru and V. B. Shenoy, *J. Power Sources*, 2012, **208**, 165-169.

115 V. B. Shenoy, P. Johari and Y. Qi, *J. Power Sources*, 2010, **195**, 6825-6830.

116 I-S. Hwang, J-C. Kim,b S-D. Seo, S. Lee, J-H. Lee and D-W. Kim, *Chem. Commun.,* 2012, 48, 7061–7063.

117 M-H. Park, Y.H. Cho, K. Kim, J. Kim, M. Liu, and J. Cho, *Angew. Chem. Int. Ed.*, 2011, 50, 9647 –9650.

118 J. Zhang, Z. Xie, W. Li, S. Dong and M. Qu, *Carbon*, 2014, 74, 153.

119 Z. Wang, Y. Fu, Z. Zhang, S. Yuan, K. Amine, V. Battaglia and G. Liu, *Journal of Power Sources*, 2014, 260, 57.

120 D. Beneventi, D. Chaussy, D. Curtil, L. Zolin, E. Bruno, R. Bongiovanni, M. Destro, C. Gerbaldi, N. Penazzi and S. Tapin-Lingua, *Chemical Engineering Journal*, 2014, 243, 372.

121 L. Yao, X. Hou, S. Hua, X. Tang, X. Liu and Q. Ru, *Journal of Alloys and Compounds*, 2014, 585, 398.

122 Y. S. Park, E. S. Oh and S. M. Lee, *Journal of Power Sources*, 2014, 248, 1191.

123 Y. X. Lin, Z. H. Huang, X. L. Yu, W. C. Shen, Y. P. Zheng and F. Y. Kang, *Electrochimica Acta*, 2014, 116, 170.

124 A. P. Cohn, L. Oakes, R. Carter, S. Chatterjee, A. S. Westover, K. Share and C. L. Pint, *Nanoscale*, 2014, 6, 4669.

125 M. L. Lee, Y. H. Li, S. C. Liao, J. M. Chen, J. W. Yeh and H. C. Shih, *Electrochimica Acta*, 2013, 112, 529.

126 J. Yi, J. Key, F. Wang, Y. G. Wang, C. X. Wang and Y. Y. Xia, *Electrochimica Acta*, 2013, 106, 534.

127 L. Gan, H. J. Guo, Z. X. Wang, X. H. Li, W. J. Peng, J. X. Wang, S. L. Huang and M. R. Su, *Electrochimica Acta*, 2013, 104, 117.

128 B. B. Wu, T. Liu, Q. B. Xia and X. D. Wu, *Journal of the Electrochemical Society*, 2013, 160, A1720.

3. Anodes for Sodium Ion Batteries based on Tin - Germanium - Antimony Alloys

Material in this chapter has been published in: ACS Nano, 2014, 8 (5), 4415–4429.

List of authors: Farbod B., Cui K., Kalisvaart P., Kupsta M., Zahiri B., Kohandehghan A., Memarzadeh E., Li Z., Luber E. J., and Mitlin D.; DOI: 10.1021/nn4063598

3.1. Introduction

While lithium ion batteries (LIBs) are the dominant secondary energy storage source for portable and electric vehicle applications, there are some concerns about lithium's cost and continued availability. Sodium-ion batteries (NIBs) have recently attracted much scientific attention as alternatives to LIBs, since sodium is more readily available than lithium and has a potential for significant associated cost reduction. [1-6] Moreover NIBs are considered as the key technology for meeting large-scale energy storage needs, [7-9] mainly due to much more "geographically democratic" availability of Na and lower cost as compared to Li. NIBs also offer an increased resistance to metal plating-induced shorts. [10] The standard electrode potential is determined by the redox couple and by the ion solvation interactions, with the difference between Li and Na standard potentials in carbonate solvents being in the range of 0.2 - 0.25 V. [11] Several classes of cathode materials have been proposed for NIBs, including $Na_{0.44}MnO_2$,

$Na_{0.85}Li_{0.17}Ni_{0.21}Mn_{0.64}O_2$, $Na_{0.7}CoO_2$, $Na_3V_2(PO_4)_2F_3$, Na_2FePO_4F, $LiFeSO_4F$, $Na_{4-\alpha}M_{2+\alpha/2}(P_2O_7)_2$ ($2/3 \leq \alpha \leq 7/8$, M = Fe, $Fe_{0.5}Mn_{0.5}$, Mn), Olivines, and NASICONs. [2,12-13] NIB anodes, on the other hand, present more of a challenge since commercial graphite has very low Na storage capacity. [14] Charge storage capacities and cycling stabilities approaching LIB graphite have been demonstrated for various amorphous or partially graphitic carbons. [15-20] Anodes based on titanium oxide, such as $Na_2Ti_3O_7$ and anatase TiO_2 have also been successfully employed. These are highly desirable from a cost and environmental friendliness perspective, while offering capacities of ~ 150 mAh g^{-1} and good cycling stability. [21-27] These materials along with the carbons represent perhaps the most economical anode option for large-scale stationary applications.

As in the case of Li, other Group 14 elements besides carbon have potentially higher storage capacities for sodium. [28] According to the equilibrium phase diagram, Sn can store 3.75 Na/host-atom ($Na_{15}Sn_4$), [29] with a resulting maximum charge storage capacity of 847 $mAhg^{-1}$. The experimentally measured capacity of Sn anodes generally approaches this value early in the testing, but degrades during cycling, *e.g.*[5,8,30-33] For instance, Yamamoto *et al.*[30] reported a NIB negative electrode based on Sn thin film with a discharge (charge) capacity of 790 (729) $mAhg^{-1}$ in the first cycle. However, this electrode showed a rapid capacity decay after 15 cycles. Ellis *et al.* [34] also observed an initial discharge capacity of ~850 $mAhg^{-1}$ for a sputtered Sn electrode, and a rapid cycling-induced capacity degradation to near zero. Sn- based alloy composites have been reported to exhibit improved cycle stability, such as $(Sn_{0.5}Co_{0.5})_{1-x}C_x$ alloy,[34] $(Cu_6Sn_5)_{1-x}C_x$, [35] SnSb/C nanocomposite,[4] Cu_6Sn_5, [36] $Sn_{0.9}Cu_{0.1}$ alloy, [37] and Sn–SnS–C nanocomposite. [38]

Antimony has also been recently examined for its potential as a NIB anode, *e.g.* [39-42] The maximum stoichiometry of Na-Sb alloys is Na_3Sb,[29,43] giving Sb a theoretical capacity of 660 $mAhg^{-1}$. Authors have examined Sb alloy and intermetallic electrodes, including Cu_2Sb with a capacity of 280 $mAhg^{-1}$, [44] AlSb with a capacity of 490 $mAhg^{-1}$, [45] Mo_3Sb_7 with a capacity of 330 $mAhg^{-1}$, [46] Sb-MWCNT nanocomposites with a capacity of ~500 $mAhg^{-1}$. [47] Germanium in thin film form or as porous nanocolumnar structures have been demonstrated to work as a NIB anodes as well. [48-49] Experimental capacities in the range of 1:1 NaGe (369 $mAhg^{-1}$) have been reported.

While binary and a several ternary (containing C) Sn- and Sb- based alloys have been examined as potential NIB anodes, little is known regarding Ge-containing systems. Here we provide the first report on thin films – based ternary Sn-Ge-Sb alloy anodes. In order to better understand the role of each element in determining the electrochemical properties of the ternary system, and to obtain baselines for clear comparisons, elemental Ge, Sb, Sn and binary Sn-Ge and Sb-Ge alloys are also evaluated. Our results demonstrate a highly promising reversible capacity and rate capability in Sn60Ge20Sb20 and Sn50Ge25Sb25 alloys. These findings should serve as a useful guide for designing improved formulations of NIB electrode materials in bulk, using methods such powder co-mechanical milling and rapid solidification.

3.2. Experimental Procedure

Target composition 100 nm films were (co-)sputtered onto polished stainless steel substrates (battery spacers) at room temperature (ATC Orion 8, AJA International Inc.). Sb and

Ge deposition were carried out using radio frequency (RF)-magnetron sputtering, while Sn deposition was performed by DC-magnetron sputtering. Depositions were performed with continuous substrate rotation in presence of Ar gas with 5N purity at a sputtering pressure of 4 mTorr, with a maximum base pressure of 5×10^{-8} Torr. The deposition rates were adjusted for stoichiometry, being in the range of 0.04 - 0.39 nm sec^{-1}. The primary approach for confirming film thicknesses depended on a series of ex-situ deposition calibrations crosschecked against *in-situ* calibrations, film weight measurements and XPS. For a range of gun powers relevant to the deposition conditions, a series of elemental films were deposited at varying times with thicknesses up to 1.5 μm. Film thicknesses were then analyzed using a standard profilometer approach, with the deposition rate per given power being back- calculated. These results were crosschecked against an *in-situ* deposition rate monitor held in the plane of the substrate (instead of the battery substrate), using known tooling factors for each element. To ensure that re-sputtering did not affect the final alloy film stoichiometry or thickness (it should not since the atomic weights of the elements are not that divergent), the weight of the alloy film was compared to the rule of mixtures weight that would be expected for the 100 nm film thickness employed for all materials. High resolution FE-SEM was employed as secondary confirmation tool for reporting the film thicknesses. Film compositions were further confirmed using X-ray photoelectron spectroscopy (XPS) and are listed in atomic %, *e.g.* Sn50Ge25Sb25 is 50at.%Sn-25at%Ge-25at%Sb.

Na half-cells were assembled using Na metal foil as the counter electrode and polyethylene separators (MTI Corporation, porosity of 36-44% and average 0.03 μm pore size). 316 stainless steel spacer disks (MTI Corporation), with a diameter and thickness of 15.8 mm and 0.5 mm, respectively, were used as the substrates for thin film deposition. Prior to

deposition, the spacers were polished down to 5 micron SiC polishing paper (Allied High Tech Products, Inc.). The substrates were then cleaned by sonication in acetone, iso-propanol, and Milli-Q water and were finally dried. The spacers were weighted before and after deposition. The microbalance employed (Mettler Toledo, XP6U) had a manufacturer quoted 0.1 μg accuracy. For each composition, 3 - 6 samples were electrochemically tested to obtain a mean value of reversible capacity. Extended cycling testing was performed on 2 - 3 specimens per composition. Table 3.1 shows the average weight and standard deviation for each composition based on 6 different samples. Table 3.2 shows the XPS and EDXS results of as-synthesized alloy electrodes. The EDXS results contain approximately ± 10% error. In general more quantitative validity may be attributed the XPS results. The raw XPS and EDXS data are shown in Figure 3.1 and 3.2.

Table 3.1: Average weight and standard deviation for each composition based on 6 different samples.

Sample	Average weight (mg)	Standard deviation
Sb50Ge50	0.0883	0.0033
Sn50Ge50	0.0983	0.0054
Sn33Ge33Sb33	0.0898	0.0039
Sn50Ge25Sb25	0.1045	0.0028
Sn60Ge20Sb20	0.1093	0.002
Sn80Ge10Sb10	0.1159	0.0014

Table 3.2: XPS and EDX spectroscopy results of as-synthesized alloy electrodes, confirming the surface and bulk composition of thin films by ± 10% error.

Sample	XPS results			EDX results		
	At.% Sn	At.% Ge	At.%Sb	At.% Sn	At.% Ge	At.%Sb
Sn50Ge50	48	52	-	46	54	-
Sb50Ge50	-	54	46	-	54	46
Sn33Ge33Sb33	33.5	34	32.5	32	36	32
Sn50Ge25Sb25	51	24	25	50	30	20
Sn60Ge20Sb20	60.5	19.5	20	59	23	18
Sn80Ge10Sb10	77	12	11	76	12	12

1 M sodium perchlorate ($NaClO_4$, Alfa Aesar, 98-102% purity) salt in ethylene carbonate (EC, Alfa Aesar: 99% purity): diethyl carbonate (DEC, Alfa Aesar: >99% purity) (1:1 by volume) was used as an electrolyte. The assembly process was carried out in an argon-filled glovebox in which oxygen and moisture concentration levels were kept below 0.2 ppm. Galvanostatic charge-discharge tests were performed on a BT2000 Arbin potentiostat at a potential range of 0.01-2 V *vs.* Na/Na^+ and a constant current (CC) density. Current densities were based on the accurately measured final weight of the films. We employ the usual definition of a reversible capacity being the capacity at first charge (desodiation). Electrochemical impedance spectroscopy (EIS) measurement was conducted on a Solartron 1470E Multichannel Potentiostat in a frequency range of 10 MHz to 0.01 Hz at open circuit potential condition with an AC perturbation of 10 mV. Na batteries were disassembled in order to do post-cycling characterization of the microstructure. Cycled electrodes were soaked and rinsed in acetonitrile (Fisher Scientific, >95% purity) and kept overnight in the glovebox to remove residual electrolyte.

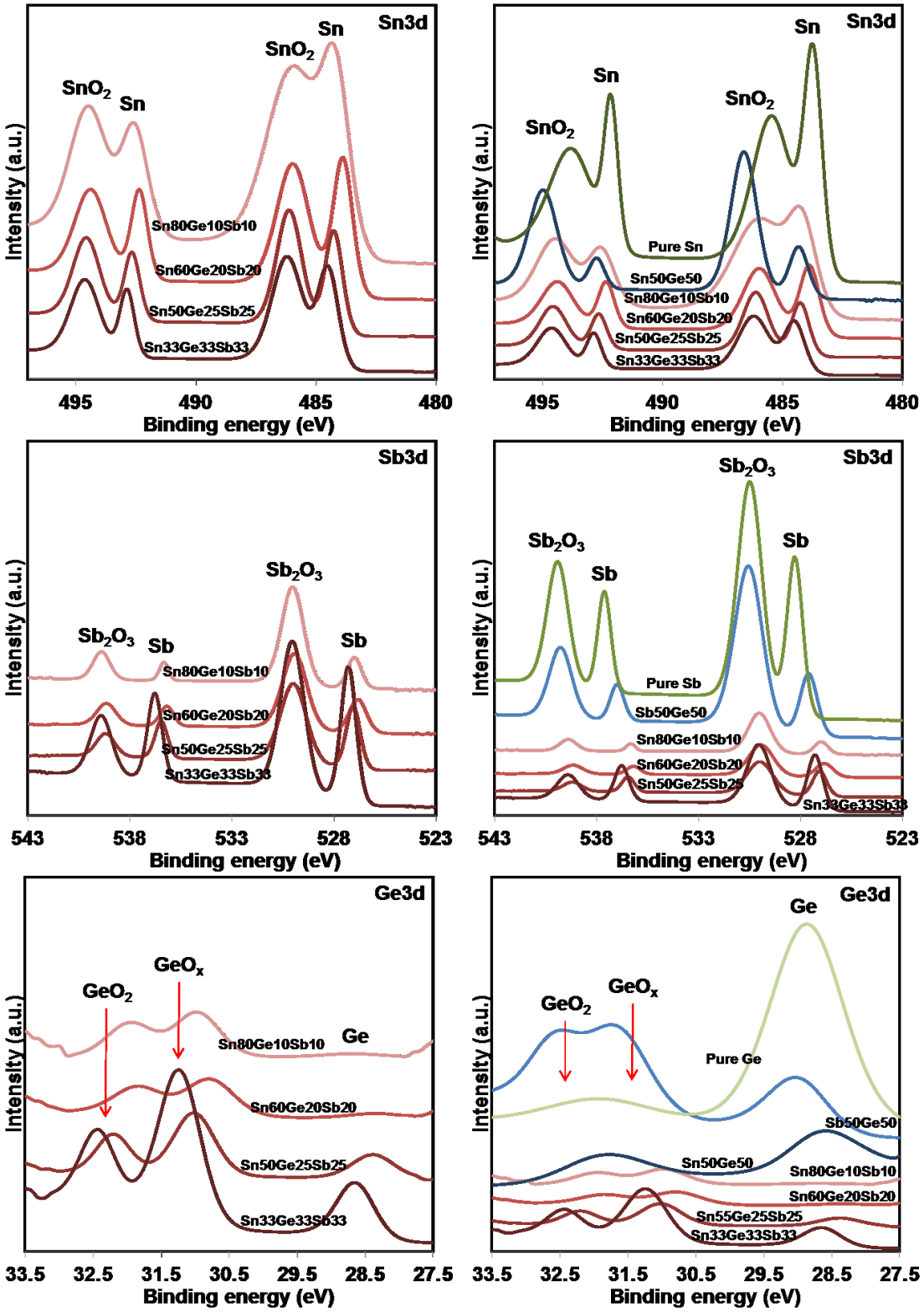

Figure 3.1: High resolution XPS spectra of Sn3d, Sb3d, and Ge3d of as-synthesized thin films.

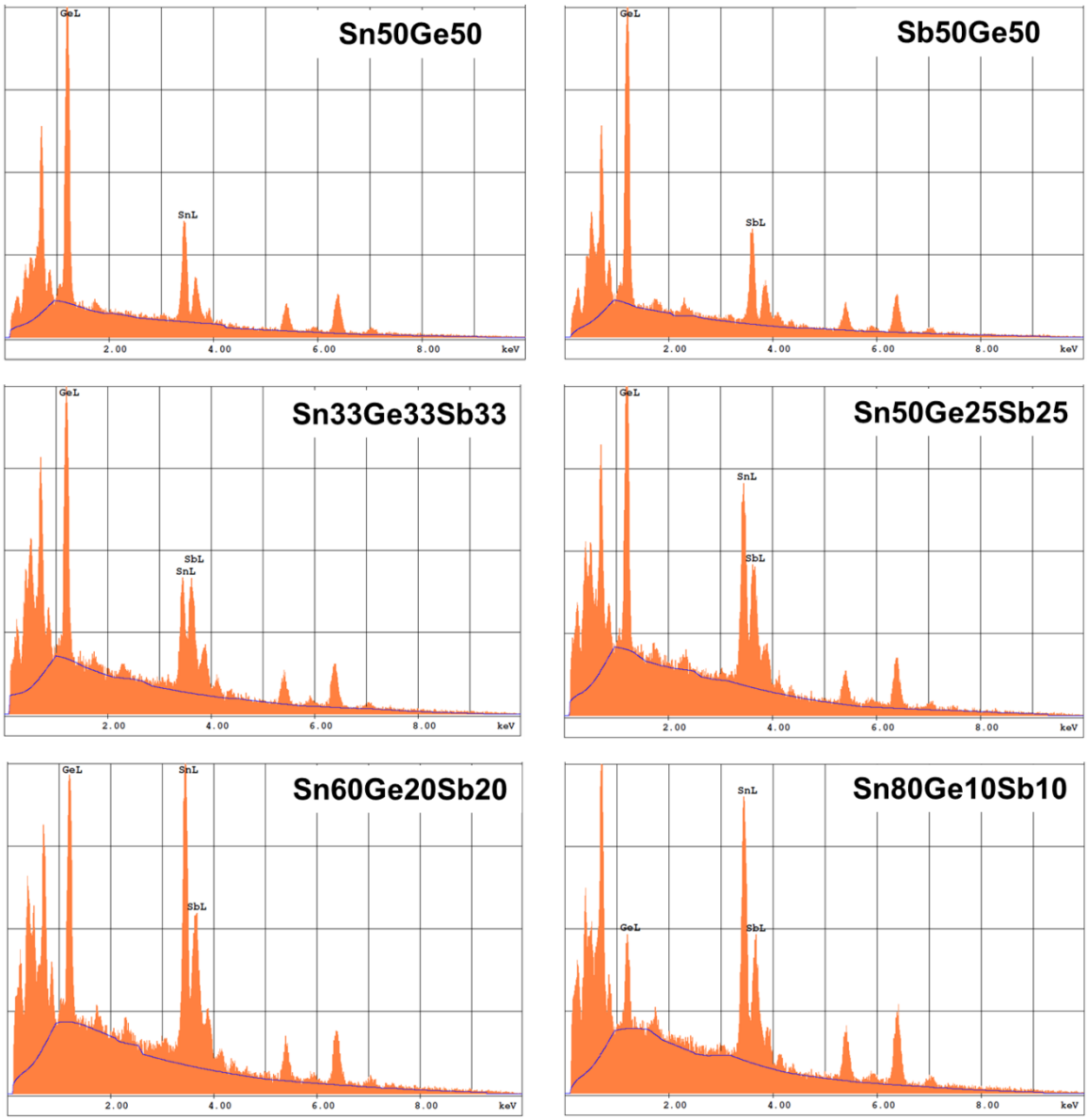

Figure 3.2: EDXS spectra of Sn3d, Sb3d, and Ge3d of as-synthesized thin films.

As-deposited and cycled samples were characterized using transmission electron microscopy TEM (JEOL 2010 and JEOL JEM 2100, both at 200 kV). Electron diffraction patterns were simulated using the commercial software Crystal Maker ™ and open-source software Diffraction Ring Profiler,[50] with the input of known space group information of the

relevant phases, such as Sn ($I4_1$/amd, 5.8197, 5.8197, 3.1749, Wyckoff position: 4a), Ge (Fd3m, 5.6578, 5.6578, 5.6578, Wyckoff position: 8a), Sb (R-3m, 4.5066, 4.5066, 4.5066, Wyckoff position: 36i), $Na_{15}Sn_4$ (I-43d, 13.16, 13.16, 13.16, Wyckoff positions Sn1:16c, Na1:12a, Na2:48e), and Na_3Sb ($P6_3$/mmc, 5.3550, 5.3550, 9.4960, Wyckoff positions Sb1:2c, Na1:2b, Na2:12k). The Diffraction Ring profiler integrates the selected area diffraction (SAD) ring pattern intensities to accurately calculate the center point of each ring. High resolution TEM (HRTEM) measurements were conducted using scanning TEM (STEM) (JEOL 2200FS, 200 kV) with a nominal beam size of 0.5 nm. Electron energy loss spectroscopy (EELS) analysis was also conducted using a 200 kV JEOL 2200FS scanning TEM (STEM) with a nominal beam size of 0.5 nm. High angle annular dark field (HAADF) images were also recorded. Digital Micrograph (Gatan, Inc.) was employed for signal collection and data extraction from EELS spectra. The Na spectrum was extracted by integrating over low loss edges of Na at 30-40 eV. Typical current densities for HRTEM imaging were 13.15 pA cm^{-2} at 400 K and 16.72 pA cm^{-2} at 500 K.

Crystal structures of as-deposited thin films were characterized by X-ray diffraction (XRD) on a Bruker AXS diffractometer with Cu-Kα radiation (λ=1.5406 Å) (Bruker Discover 8). The diffractometer is equipped with a HiStar general area 2-dimensional detection system (GADDs) with sample–detector distance of 15 cm. Phase identification was performed employing the XRD database on EVA software. The presented XRD patterns were obtained by subtracting the pattern of the substrate from the composite. To achieve this we performed XRD on both the stainless substrate and on the deposited thin film on the substrate, employing identical scanning conditions. The mathematical subtraction was performed using EVA™ commercial software. Cross-sectional samples of cycled materials were obtained using a Hitachi NB5000 dual beam focused ion beam/scanning electron microscopy (FIB/SEM). To prepare FIB

samples, a proper area from the bulk of the sample was selected using SEM. A thin layer of carbon and tungsten were then deposited on the top of the area. Using FIB and micro-sample manipulator, the selected volume was finally isolated, lifted out, and placed on a Cu 5-post grid.

The as-synthesized and cycled thin films were also analyzed using EDX spectroscopy with scanning electron microscopy (SEM) on a Hitachi FESEM S-5500. XPS measurements were conducted on an ULTRA (Kratos Analytical) spectrometer under ultrahigh vacuum (10^{-9} Torr), using monochromatic Al-K_α radiation ($h\nu$ = 1486.6 eV) operated at 210 W. The high-resolution spectra were collected with an energy window of 20 eV. The XPS data were analyzed using CasaXPS software. The sodiated Sn50Ge25Sb25 thin film electrode was depth analyzed using time-of-flight secondary ion mass spectrometery (TOF-SIMS) instrument (ION-TOF GmbH). The analysis chamber was kept at a pressure of less than 5 x 10^{-9} mbar and a 25 kV Bi^+ ion source was used for analysis. 1 kV O_2^+ ions with current of ~34 nA were also used for sputtering with the rate of ~0.06 nm/s. The analysis and sputtering areas were 40 μm × 40 μm and 200 μm × 200 μm, respectively.

Prior to XRD, XPS and TOF-SIMS analysis the samples were covered and sealed with Parafilm in a glovebox to avoid exposure to air. Next, the air-tight sample holder was transferred to the XRD instrument for measurement of the XRD patterns. For TEM, the samples were quickly transferred into the TEM, reducing its air exposure to around 20 s. TEM analysis did not reveal excessive oxide formation on the surfaces and we were able to perform quantitative HRTEM and analytical TEM without interference from the oxide.

3.3. Results and Discussion

TEM images of the as-deposited 100 nm thick elemental films are shown in Figures 3.3. The as-deposited Sn, as shown in Figures 3.3(a) – 3.3(c), is composed of relatively large crystallites of various orientations. The as-sputtered pure Ge (Figures 3.3(d) – 3.3(e) is diffraction amorphous (*i.e.* amorphous, nanocrystalline or a combination of the two) as evidenced by the washed out SAD ring pattern. The as-deposited Sb film is continuous and polycrystalline, with the grain size being large enough to generate single-crystal SAD patterns when the smallest field-limiting aperture is employed (Figures 3.3(f) – 3.3(h)). The crystallinity of pure Sn and Sb and the amorphous/nanocrystalline structure of Ge are confirmed by XRD analysis, as shown in Figure 3.4. These results are in good agreement with previous studies on Sn, Ge, and Sb films.[38,40,48,51]

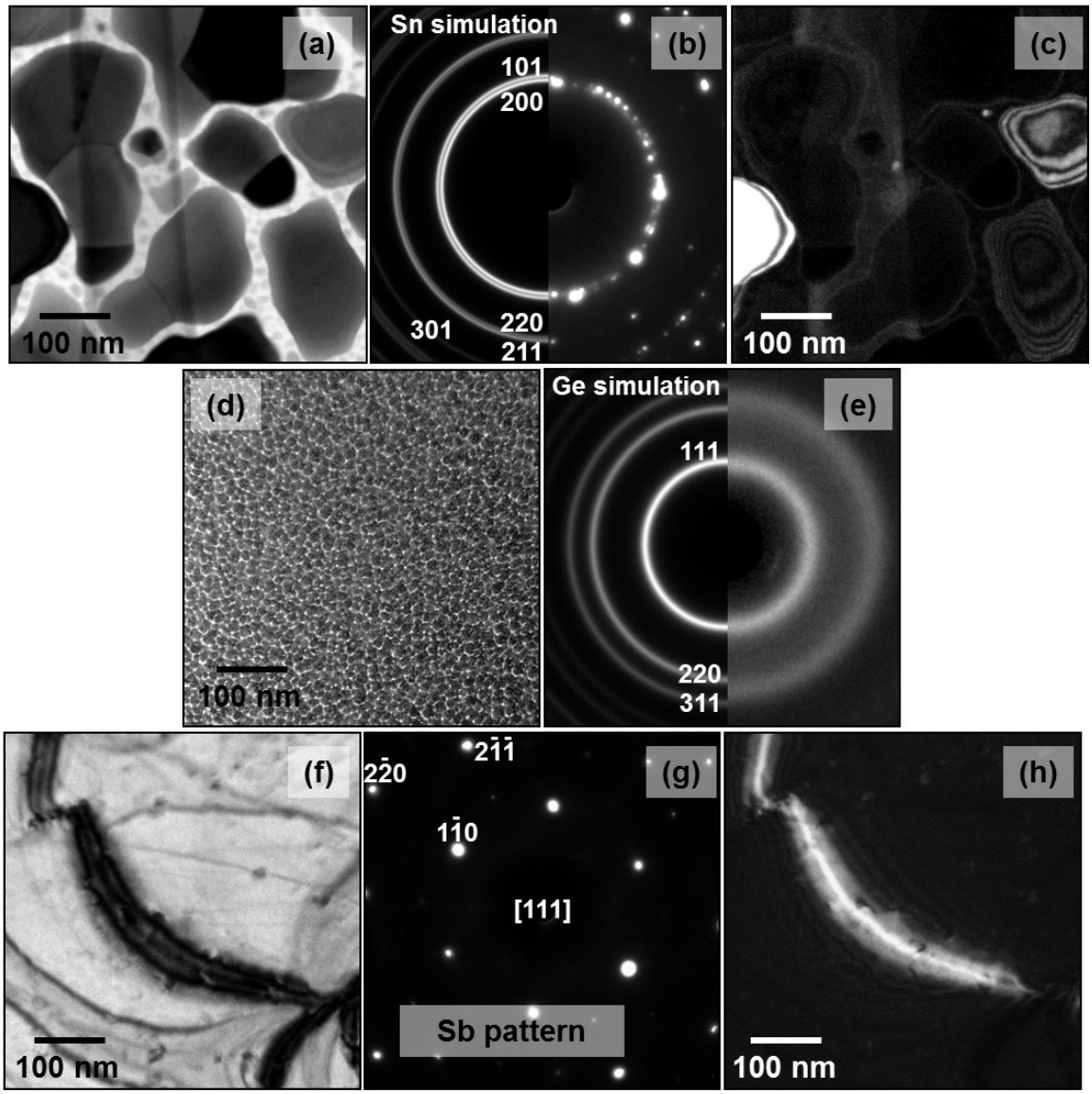

Figure 3.3: TEM micrographs of as-deposited (a)-(c) Sn, (d)-(e) Ge, and (f)-(h) Sb thin films. (a,d,f) Bright-field images, (b,e,g) corresponding SAD patterns, (c) dark-field image of Sn thin film taken from $(200)_{Sn}$ diffraction ring, (h) dark-field image of Sb thin film taken from $g = [1\text{-}10]_{Sb}$ diffraction spot.

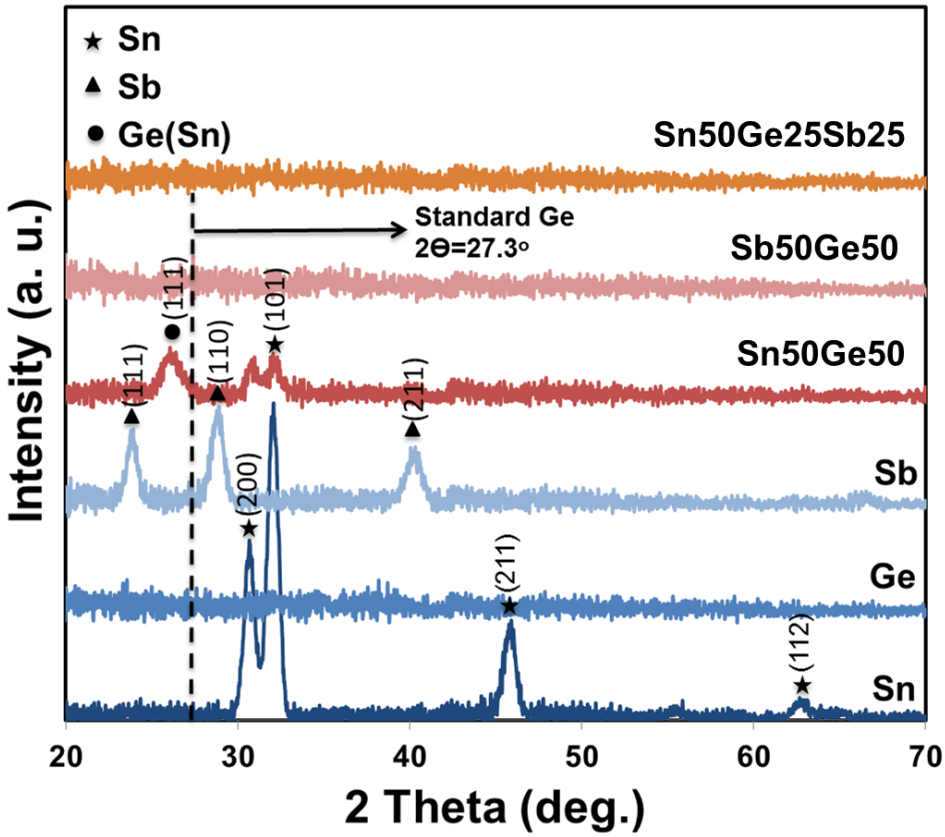

Figure 3.4: Indexed XRD patterns of as-deposited elemental and alloyed thin films.

Figures 3.5(a)- (b) show TEM micrographs and the indexed SAD pattern of the as-synthesized Sn50Ge50 alloy, which is a two-phase nanocomposite. Polycrystalline Sn is detected, as the 200, 101 and 211 Sn diffraction rings are visible in the SAD pattern. Two additional reflections belonging to Ge are also present. The associated d-spacing for the 111 and 220 Ge rings is expanded by ~6% with respect to elemental Ge, indicating that there is extended substitutional solid solubility of Sn in Ge, likely much beyond the equilibrium 1%. XRD analysis of the as-synthesized materials, shown in Figure 3.4, confirms this shift in the Ge lattice parameter. As is marked in the figure, the equilibrium position of the Ge (111) reflection (the film is highly textured) should be at 2θ = 27.30°, whereas it is located at 2θ = 25.70°,

corresponding to a 6% shift in the lattice parameter, which is the same as measured by TEM. Figures 3.5(c) presents TEM analysis of the as deposited Sb50Ge50. The equilibrium Sb-Ge phase diagram demonstrates negligible room temperature solubility and no intermediate phases. However, as evidenced by the SAD pattern, co-sputtering of Sb and Ge results in the formation of an amorphous alloy with the broad rings corresponding to the first and the second nearest neighbors. This conclusion is also confirmed by the XRD pattern of this alloy shown in Figure 3.4. Figures 3.5(d) and 3.5(e) show the Sn80Ge10Sb10 microstructure, which consists of nanocrystalline Sn with no evidence of Ge or Sb precipitates. TEM analysis of Sn33Ge33Sb33 is presented in Figures 3.5(f). Analysis of Sn50Ge25Sb25 is shown in Figures 3.5(g) - (i). The Sn33Ge33Sb33 alloy appears amorphous, while Sn50Ge25Sb25 has a two-phase structure consisting of an amorphous phase and nanocrystalline Sn. The Sn nanocrystals may be imaged in dark field (Figure 3.5(h)) and by HRTEM (Figure 3.5(i)). The Sn-rich side of the ternary Sn-Ge-Sb diagram consists of a mixture of Sn, SbSn and Ge phases with appreciable mutual solubility. [52] However, we detected no crystalline phases besides Sn. This means the rest of the material will consist of an amorphous matrix that may be compositionally homogeneous or segregated.

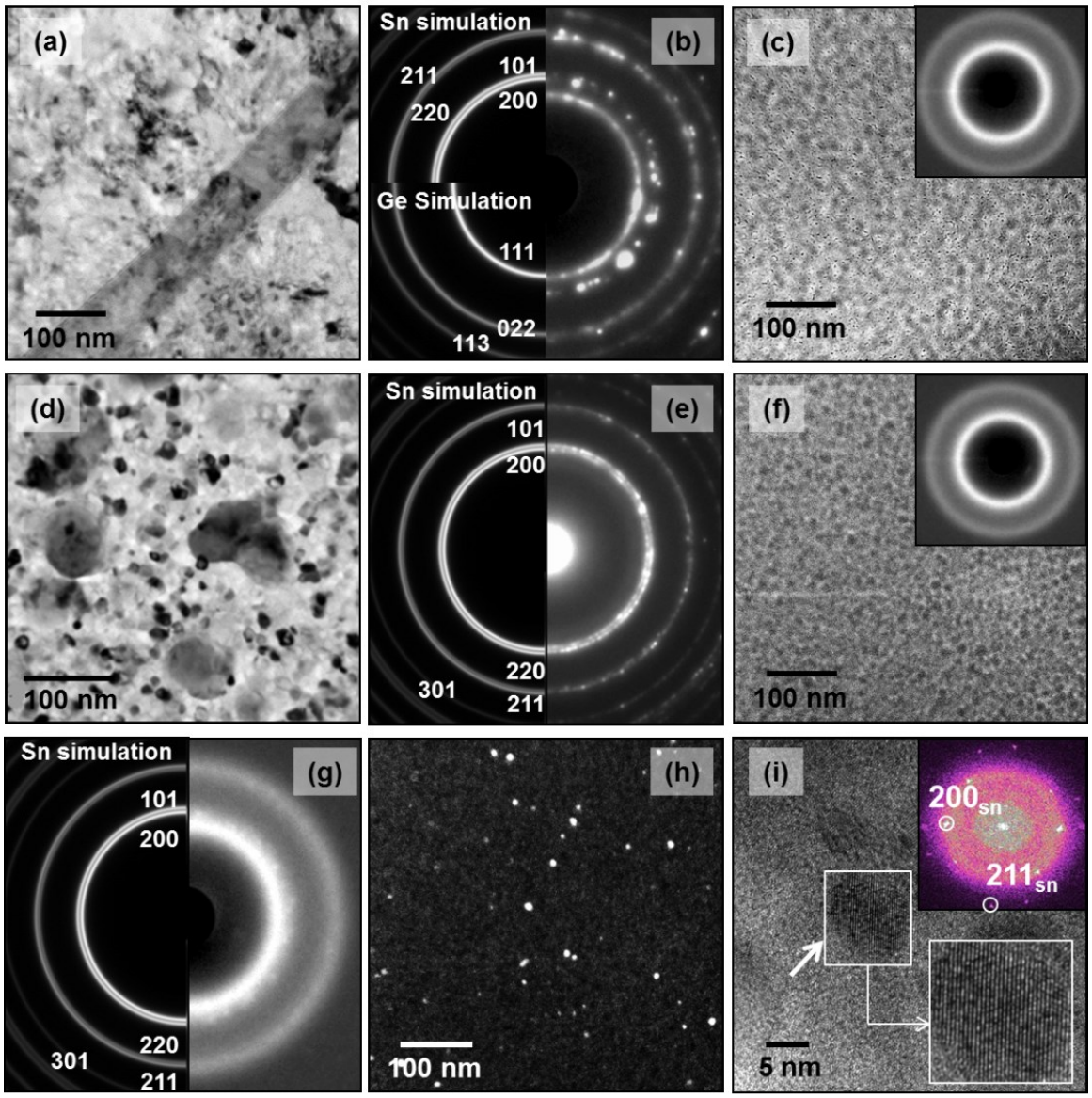

Figure 3.5: TEM analysis of as-synthesized alloys (pure Sn, Sb, Ge are shown in Suppl): (a) - (b) Sn50Ge50, bright field micrograph and simulated SAD with the Sn-induced expansion of the Ge lattice being taken into account. (c) Sb50Ge50, (d) and (e) Sn80Ge10Sb10, (f) Sn33Ge33Sb33, and (g) - (i) Sn50Ge25Sb25. The dark field image (h) was taken using a portion of the (200) and (101) Sn rings. (i) HRTEM micrograph showing a Sn nanocrystallite (arrowed) embedded in an amorphous matrix. The corresponding FFT is shown in the insert.

The trend of larger amounts of the amorphous phase with greater GeSb content can be better understood by analyzing the glass forming ability of (GFA) of all 3 binary alloys *i.e.*,

GeSb, SnGe and SnSb. From previous studies of co-sputtered films of GeSb, [53] SnGe, [54] and SnSb, [55] it is found that both GeSb and SnSb films deposited over a wide range of compositions possess an amorphous microstructure, while SnGe does not exhibit an amorphous phase at any of the studied compositions (also confirmed in our data). Moreover, the GFA of GeSb [53] and SnSb [55] alloys are found to highest when both components are in roughly equal proportion (*i.e.* ~50 at.% Sb). As such, we would expect to have the highest fraction of amorphous phase when both the Sn/Sb and Ge/Sb ratios are close to 1. For the films considered in this study the Ge/Sb ratio is always fixed at 1, while the Sn/Sb ratio approaches 1 as the GeSb content is increased relative to Sn. Specifically the condition of both Sn/Sb and Ge/Sb ratios being equal to 1 is satisfied at Sn33Ge33Sb33, which is found to consist completely of amorphous phase. However, it must be noted that this analysis is only a qualitative guide to understanding the trends that we observe, to more fully understand this phenomenon it is necessary to characterize the GFA properties of the ternary Sn-Ge-Sb *via* calorimetric or diffraction heating experiments.

The sodiation behavior of the elemental films is shown in Figure 3.6. Pure Sn was tested at 85 mAg^{-1}, Ge was tested at 110 mAg^{-1}, while Sb was tested at 120 mAg^{-1}. For pure Sn the reversible capacity drops to 38 mAh g^{-1} only after 10 cycles - far below its theoretical value. This agrees with previous studies on sodiation of pure Sn, where the materials degrade very rapidly during cycling.[30,31,34,56] During the first sodiation process, there are four sloping plateaus at roughly 0.45, 0.18, 0.08, and 0.03 V, although the only equilibrium phase that is observed to form electrochemically is $Na_{15}Sn_4$. Upon charging, the plateaus are at approximately 0.15, 0.28 and 0.55 and 0.63 V. The plateaus become less distinct with cycling. The reversible capacity of Ge is 349 $mAhg^{-1}$, being close to a 1:1 ratio of Na/Ge (369 $mAhg^{-1}$) and agreeing with a previous report.[42] The voltage profile of Ge presents an initial sharply sloping plateau during the first and

subsequent sodiation cycles from ~ 1V down to 0.1 - 0.15 V, followed by a flat plateau at 0.1 - 0.15 that remains until discharge. There is a large hysteresis in the charge/discharge behavior, with the flat desodiation plateau being at 0.6 V. The reversible capacity of Sb is 650 $mAhg^{-1}$, which is close to the 660 $mAhg^{-1}$ theoretical. In the pure Sb films, the voltage profiles show 2 sloping plateaus during sodiation, centered around 0.75 and 0.55 V. Only 2 stable intermetallics, NaSb and Na_3Sb, are known in the Na-Sb system.[29] Intermediate phases may be possible, as the voltage profile is not sharp enough to conform or negate their presence. During desodiation two plateaus are observed at around 0.78 and 0.85 V. The voltage profiles along with the TEM analysis of the post-cycled microstructure indicate that the desodiated Sb film is still crystalline after 10 cycles. Both elemental Ge and elemental Sb degrade during cycling, though not at a rate as fast as Sn. The sodiation voltage profiles of the individual elements are generally in agreement with previous reports.[8,39,48-49]

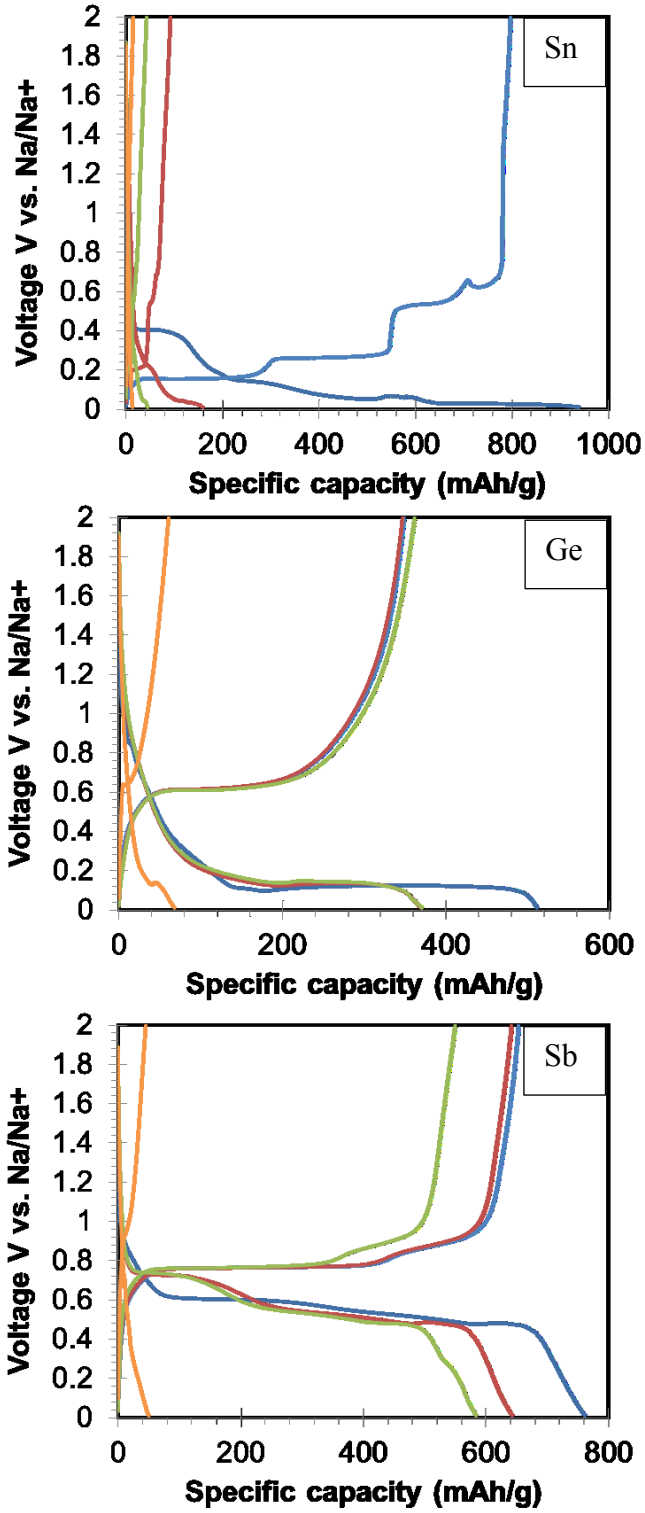

Figure 3.6: Constant current (CC) voltage profiles of elemental films.

Figure 3.7 shows the TEM analysis of the cycled elemental Sn, elemental Ge, and elemental Sb electrodes. All sodiated samples are characterized after the first Na insertion, while desodiated samples are characterized after 5 full cycles. Figures 3.7(a) – (c) show sodiated pure Sn, (d) – (f) show desodiated Sn, (g) – (i) sodiated Ge, (j) – (k) desodiated Ge, (l) – (n) sodiated pure Sb, and (o) – (q) desodiated Sb. The dark field image in (c) is taken using a portion of (022) and (013) $Na_{15}Sn_4$ diffraction rings. The dark field image in (f) is taken from the g = $(200)_{Sn}$ diffraction spot. The formation of the $Na_{15}Sn_4$ terminal phase is confirmed by TEM characterization of the Sn electrode discharged to 0.01 V. Desodiation leads to the formation of crystalline Sn. This is consistent with previous *in-situ* observations. [32,57] These findings are confirmed by XRD analysis, as presented in Figure 3.8. For as synthesized specimen, the (111), (110) and (211) peaks are respectively located at 2θ = 23.77, 28.77, 40.13°. For the desodiated one, these are located at 2θ = 23.83, 28.89, 40.39°, indicating that the crystalline structure is restored without any noticeable changes in the lattice parameter. TEM analysis indicates that the Ge electrode sodiated to 0.01V is partially nanocrystalline, though the exact phase could not be identified. Similar to the recent reports on Ge thin films,[48-49] it seems that the sodiation process of Ge reaches a metastable phase which is not on the equilibrium Na-Ge phase diagram. The desodiated Ge sample is diffraction amorphous.

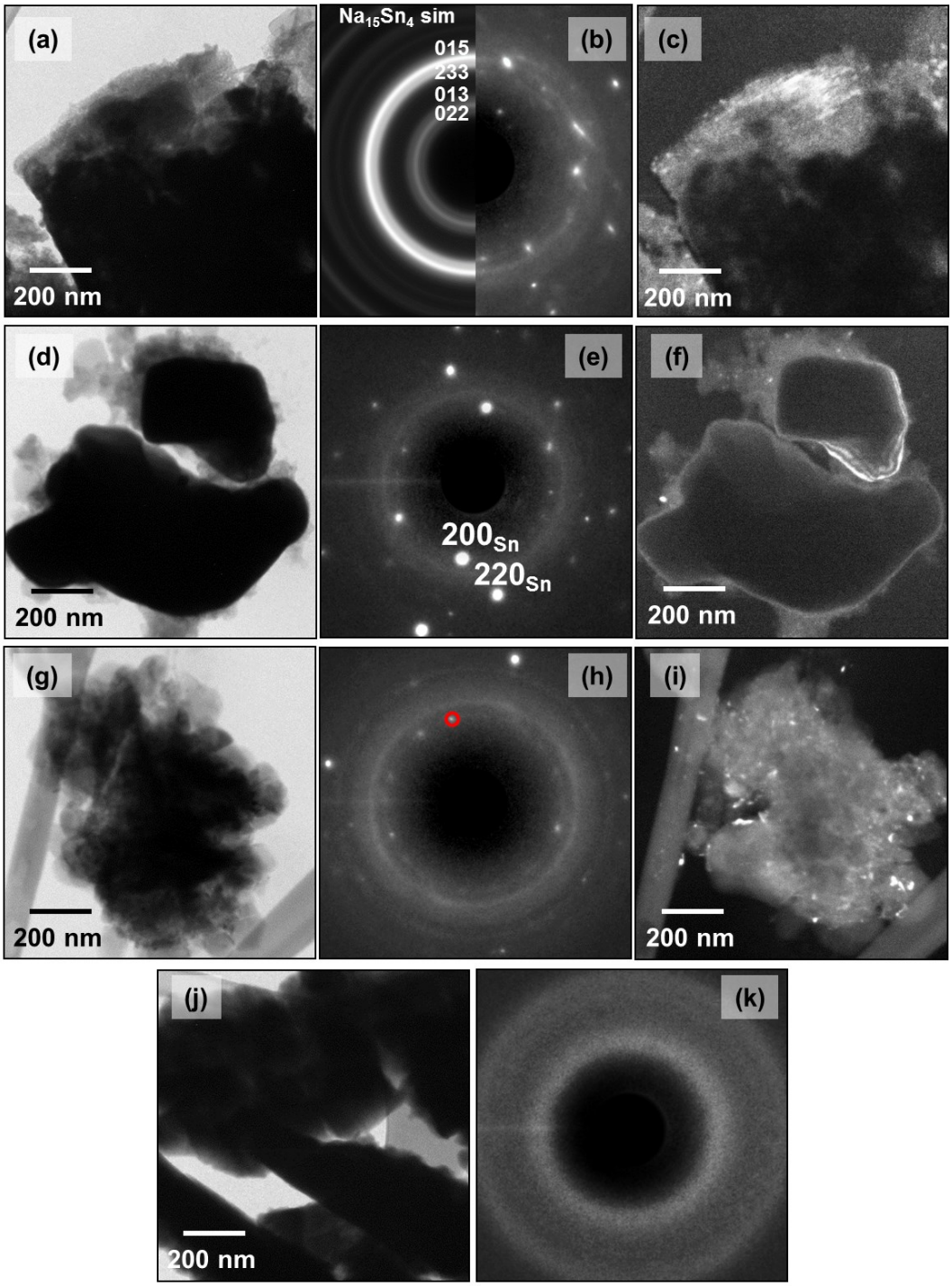

Figure 3.7: TEM micrographs of cycled elemental Sn, elemental Ge, and elemental Sb electrodes. All sodiated samples are characterized after first Na insertion, while desodiated samples are characterized after 5 full cycles. (a)-(c) Sodiated pure Sn, (d)-(f) desodiated Sn; (g)-(i) sodiated Ge; (j)-(k) desodiated Ge. Dark field image in (c) is taken using a portion of (022) and (013) $Na_{15}Sn_4$ diffraction rings. Dark field image in (f) is taken from g = $(200)_{Sn}$ diffraction spot. The dark field in (i) is taken using the region near the marked spot.

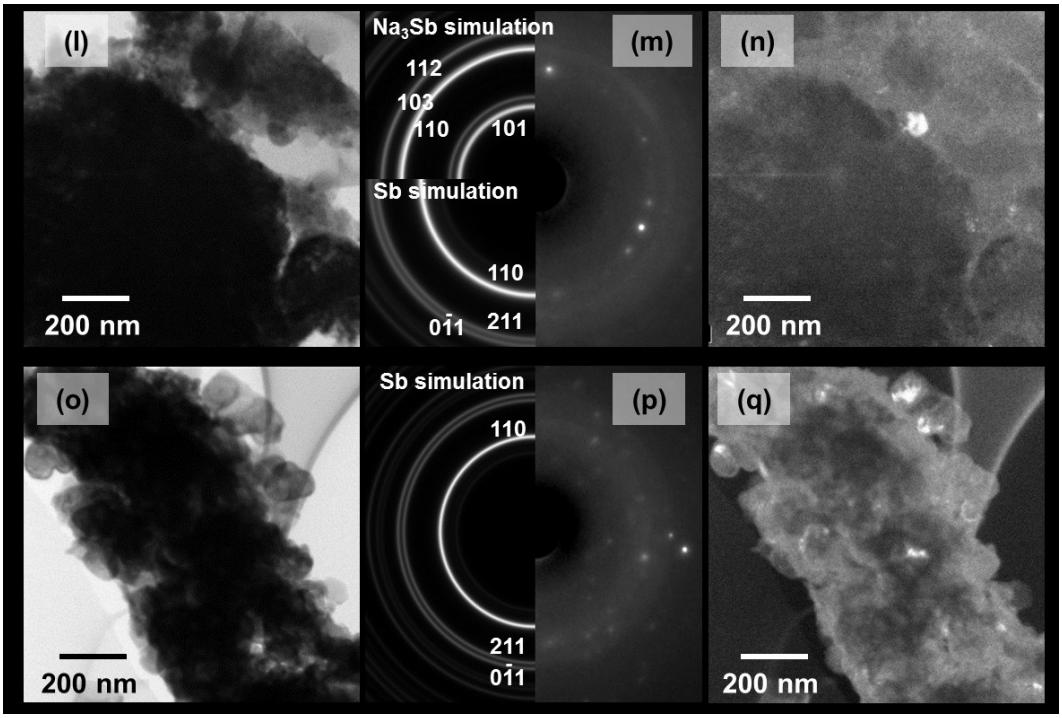

Figure 3.7, cont.: TEM micrographs of cycled elemental Sn, elemental Ge, and elemental Sb electrodes. All sodiated samples are characterized after first Na insertion, while desodiated samples are characterized after 5 full cycles. (l)-(n) Sodiated pure Sb; (o)-(q) Desodiated Sb. Dark field images in (n) and (q) are taken using a portion of the (110)Sb rings pattern.

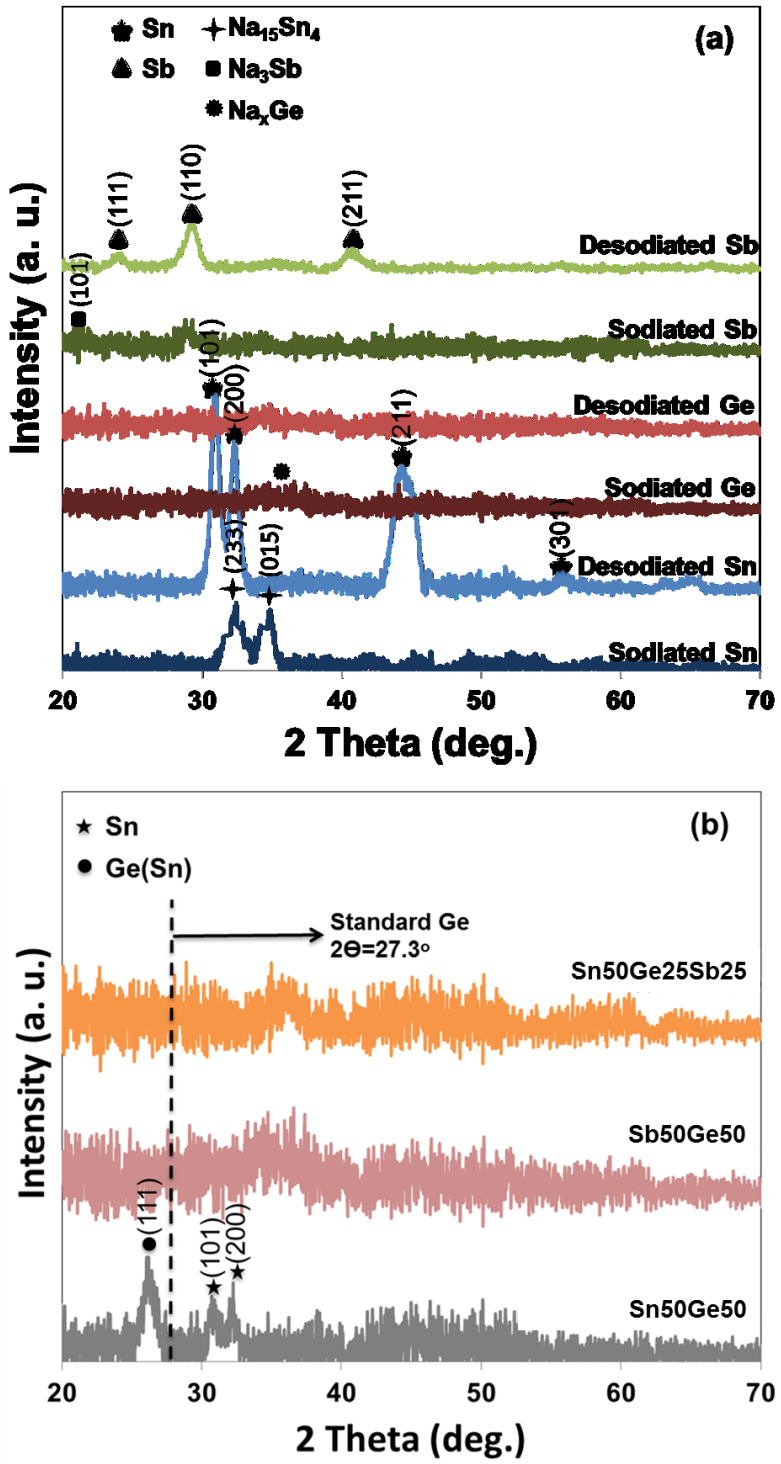

Figure 3.8: (a): Indexed XRD patterns of sodiated and desodiated elemental thin films. (b): XRD patterns of desodiated binary Sn50Ge50 and Sb50Ge50 and ternary Sn50Ge25Sb25 alloys.

Figure 3.9 shows the voltage *versus* capacity behavior for the binary and the ternary alloys, which were tested at 85 mAg^{-1}. The constant current (CC) voltage profile of Sn50Ge50, shown in Figure 3.9(a), reveals three sloping sodiation plateaus near approximately 0.28, 0.19, and 0.03 V. The system displays two sloping desodiation plateaus near 0.16 and 0.6 V. The voltage profiles, particularly for desodiation, are nearly identical for cycle 1-10 indicating a stable microstructure. For the second to tenth cycle, coulombic efficiency (CE) is nearly 100 %, with a reversible capacity of 713 $mAhg^{-1}$. This is substantially more than what is expected based on a weighted average (the alloy is Sn-38%Ge by weight) of theoretical capacities of the elemental films (665 $mAhg^{-1}$). The voltage profiles of Sb50Ge50 are shown in Figure 3.9(b). The reversible capacity is 551 $mAhg^{-1}$, which is close to a rule of mixtures prediction (the alloy is Sb-37%Ge by weight) based on either the experimental or the theoretical values for Sb and Ge. The stable cycling voltage behavior of this alloy demonstrates a single broad monotonically decreasing slope between 0.8 and 0.2 V upon discharge, and between 0.6 to 1.2 V upon charge. The absence of sharply defined plateaus indicates that there are no two-phase regions with each phase being energetically distinct. Rather there is a continuing variation in occupational site energies, as would be expected for a solid solution with a continuously varying Na content or with nanocrystals where a second phase is difficult to nucleate due to size effects.

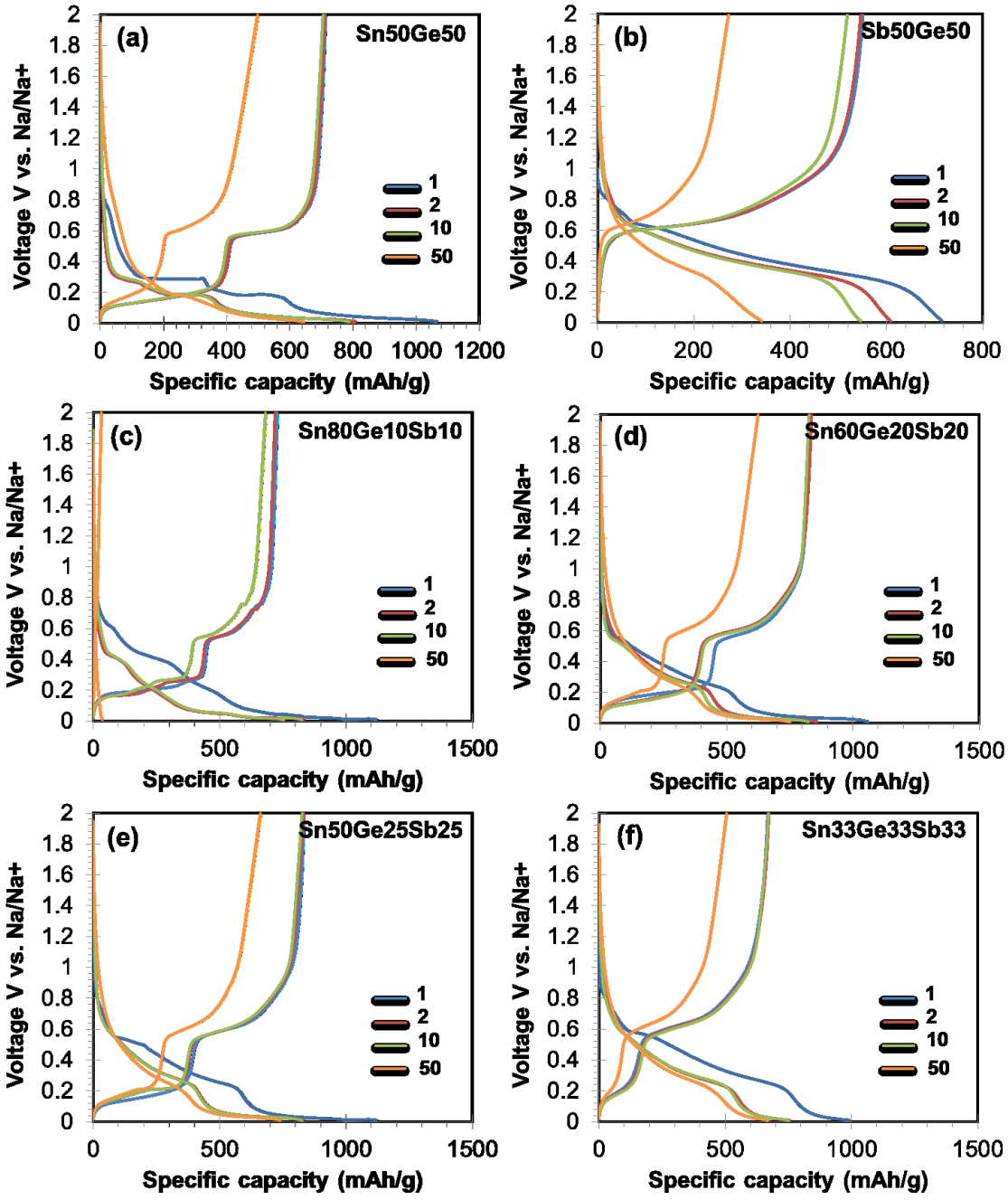

Figure 3.9: Constant current voltage profiles of binary and ternary alloys. All systems were tested at 85 mAg^{-1}.

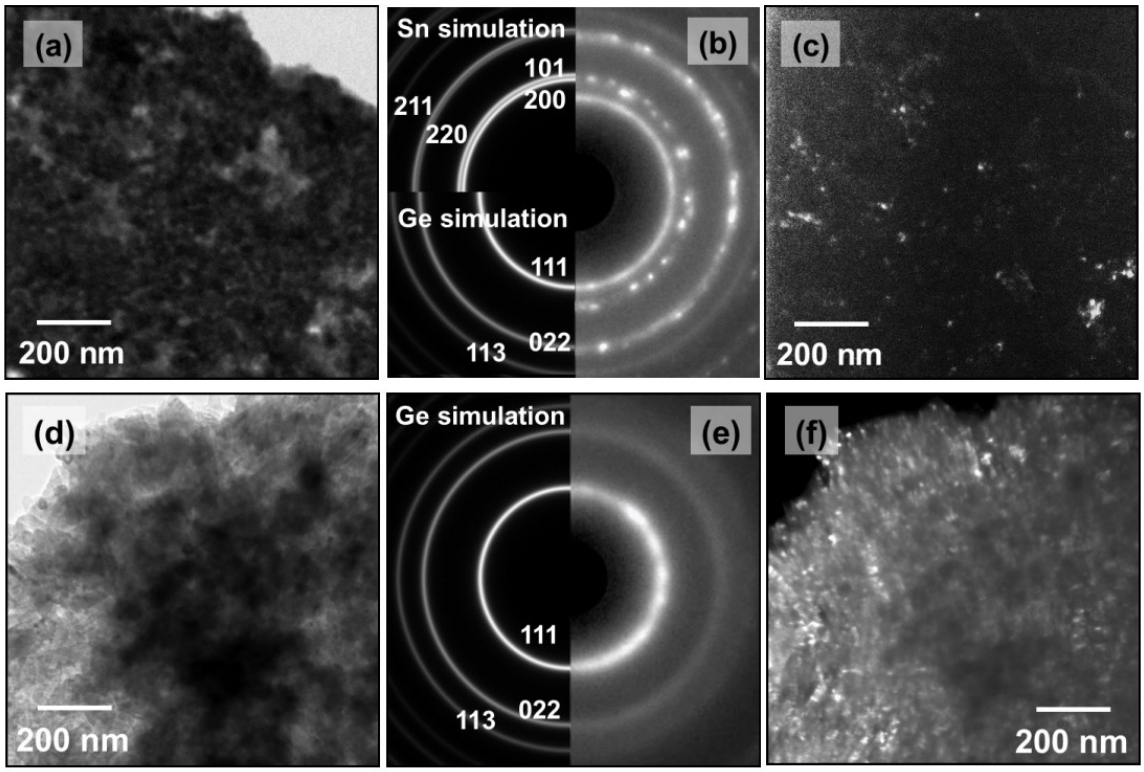

Figure 3.10: (a) - (c) Stable cycled microstructures (10 cycles). Desodiated Sn50Ge50, bright field image, indexed SAD pattern and dark field image taken using a portion of the Sn (200) (101) and Ge (111) ring patterns. In (b) the Sn-induced expansion of the Ge lattice parameter has been taken into account. (d) - (f) Desodiated Sb50Ge50. The dark field image in (d) was taken using a portion of the Ge (111) ring.

The constant current voltage profiles for the Sn-Ge-Sb alloys are presented in Figures 3.9(c)-(f). At least three voltage plateaus, each with a distinct flat or a sloping profile, are observed both upon charge and upon discharge in every alloy. Qualitatively the voltage-capacity profiles of the ternary systems are more similar to that of Sn-Ge than to Sb-Ge. Moreover the position and the slope of the plateaus evolve with alloy composition. The measured reversibly capacities of Sn80Ge10Sb10, Sn60Ge20Sb20, Sn50Ge25Sb25, and Sn33Ge33Sb33 are 728, 829, 833 and 669 $mAhg^{-1}$, respectively. This is an intriguing finding since the values for Sn60Ge20Sb20 and Sn50Ge25Sb25 are considerably above the weighted average

combination of the elemental capacities. For instance one can assume the known theoretical capacity of Sn (847 $mAhg^{-1}$) and of Sb (660 $mAhg^{-1}$), and a 1:1 Na/Ge ratio (369 $mAhg^{-1}$). In that case alloys Sn80Ge10Sb10 (Sn-6wt%Ge-10Sb), Sn60Ge20Sb20 (Sn-13wt%Ge-22Sb), Sn50Ge25Sb25 (Sn-17wt%Ge-28Sb) and Sn33Ge33Sb33 (Sn-23wt%Ge-39Sb) should be 800, 743, 714 and 664 $mAhg^{-1}$, respectively.

As the TEM micrographs in Figure 3.10(a) - (c) demonstrate, the cycled microstructure of Sn50Ge50 contains both Sn and Ge nanocrystallites. The dark field image in Figure 3.10(c) highlights the nanocrystalline nature of the cycled material. The Ge nanocrystals still contain solutionized Sn, with the Ge diffraction rings being closer than the equilibrium spacing (Sn would expand the Ge lattice). From the (111) reflection, the lattice constant is estimated as approximately 5.92 Å, which is 4.77% larger than elemental Ge (5.65 Å). From measurements of the nearest-neighbor distance in Ge-20at%Sn films, 2.7 Å, [58] it can be inferred that Sn strongly expands the Ge lattice and that the amount of dissolved Sn in the Ge phase is at maximum 10 at.% or less. Figure 3.8 shows the XRD patterns of desodiated binary Sn-Ge and Sb-Ge and ternary Sn50Ge25Sb25 alloys. It is confirmed that Ge contains Sn in substitutional solid solution, with a comparable contraction in the 2θ values of the (111) Ge XRD Bragg peaks. As is marked in the figure, the equilibrium position of the Ge (111) reflection (the film is highly textured) should be at $2\theta = 27.30°$, whereas it is located at $2\theta = 26.04°$, corresponding to a 4.8 % shift in the lattice parameter. The broad background intensity in the TEM SAD indicates that there is also substantial presence of an amorphous phase. This is reasonable as the initially fully amorphous alloy is expected to decompose relatively slowly at room temperature, especially concomitantly with the insertion/extraction of Na ions. As Figures 3.10(d) - (f) demonstrate the desodiated Sb50Ge50 microstructure consists of a dense distribution of Ge nanocrystallites

embedded in an amorphous matrix. For the case of Sb-Ge, the Ge crystallites, they have a lattice parameter at the equilibrium value, demonstrating negligible solutionizing of Sb. This is the key difference between the Sn-Ge and Sb-Ge, where in the latter case the Sb atoms are unable to remain in Ge substitutional solid solution during cycling, which leads us to conclude that that observed Ge lattice expansion in the Sn-Ge-Sb alloy is likewise due to the effect of Sn.

Figures 3.11(a) presents the SAD pattern of a steady-state microstructure of the desodiated Sn50Ge25Sb25 alloy after 10 cycles. Although the sample was X-ray amorphous (Figure 3.8(b)), it was possible to resolve the crystallites in the electron diffraction patterns. The desodiated Sn50Ge25Sb25 is a multi-phase nanocomposite. According to the indexed SAD pattern shown in Figure 3.11(a), nanocrystalline Sn is present in the material as evidenced by the (200), (101), and (220)/(211) Sn rings. Well-identifiable ring patterns ascribed to (111), (220) and (311) Ge are present in the SAD as well, giving proof to the presence of nanocrystalline Ge. However from a comparison of the experimental SAD pattern with a simulation, there is no evidence for crystalline Sb. Figure 3.11(b) – (c) display HRTEM images of this alloy in the desodiated state after 10 cycles. The Sn and Ge nanocrystallites are densely dispersed in an amorphous matrix. As confirmed by EDX spectroscopy, shown in Figure 3.12, the amorphous matrix is a ternary alloy composed of Sn, Ge, and Sb elements. The amorphous matrix may act as a mechanically buffering phase, allowing for repeated expansion/contraction with reduced levels of localized fracture.

While such effects have been achieved through intelligent design by careful chemical synthesis,[59,64] here it may occur in situ through a natural microstructural evolution. Figure 3.11d shows this alloy in the sodiated state, highlighting the nonspherical morphology of $Na_{15}Sn_4$ intermetallics. Figures 3.11e and f show HRTEM analysis of the post 10 cycles sodiated

Sn80Ge10Sb10. The material contains coarser and largely spherical Na15Sn4 particles, two representative crystallites being shown by arrows. There is no evidence of a separate Ge phase either from the HRTEM images or from the indexed SADs of the post-cycled material (not shown). However an amorphous matrix was also observed in this specimen.

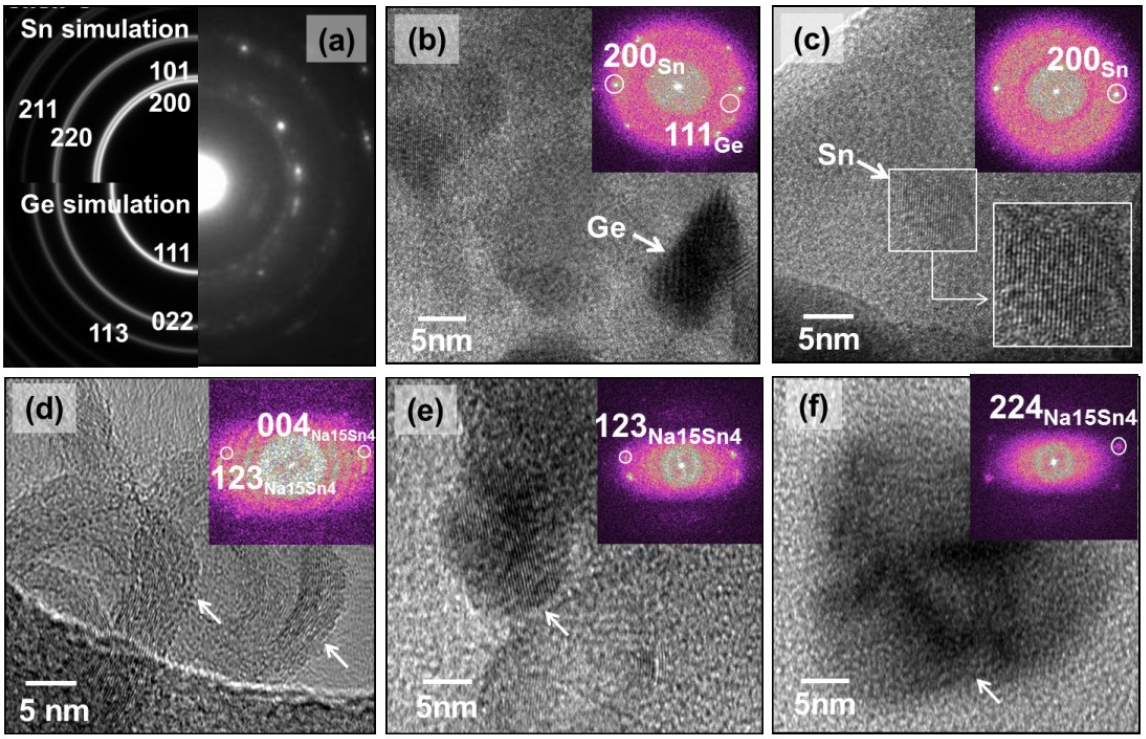

Figure 3.11: (a) - (c) Desodiated Sn-25Ge-25Sb. HRTEM analysis in (b) and (c) highlights the ~ 5 nm diameter Sn and Ge nanocrystallites dispersed within an amorphous matrix. Figure 4(d) shows this alloy in the sodiated state, highlighting the non-spherical morphology of $Na_{15}Sn_4$ intermetallics. (e) - (f) Sodiated Sn-10Ge-10Sb, which contains coarser and more spherical $Na_{15}Sn_4$ particles and no evidence of a separate Ge phase.

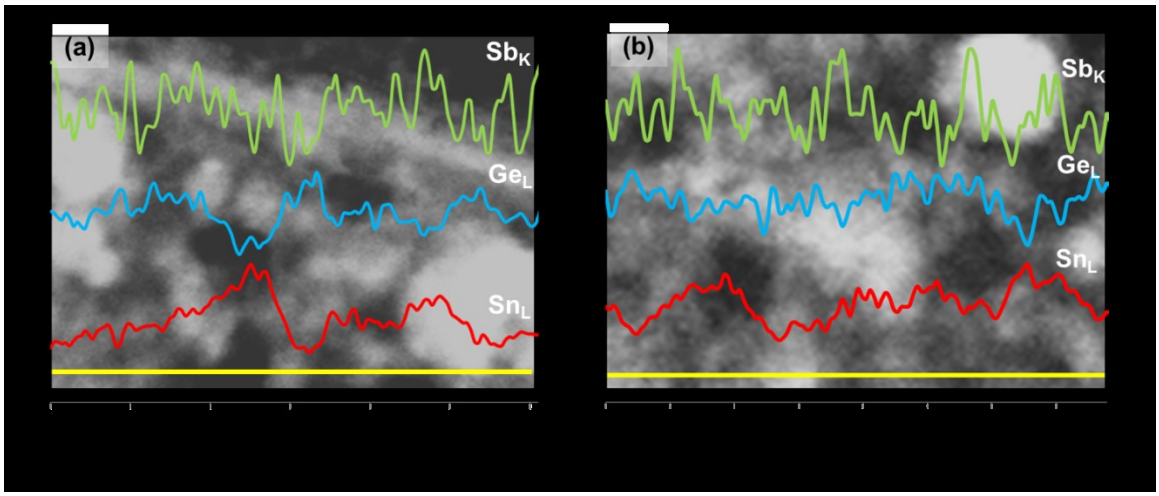

Figure 3.12: (a) - (b) TEM EDX line scans overlaid on HAADF images of desodiated Sn50Ge25Sb25 alloy electrode after 2 cycles, showing Sn_L, Ge_L, and Sb_K signal variation along the yellow line.

Revisiting the extraordinary results shown in Figure 3.9 - we may begin to understand the origin of the excess capacity beyond the theoretical rule of mixtures by first considering which alloys demonstrate it and which do not. The phenomenon is observed in Sn50Ge50 and in ternary Sn-Ge-Sb alloys of richer Ge content. It is neither observed in Sb50Ge50 nor in Sn80Ge10Sb10. It is unlikely that the extra capacity comes from the Sn nanocrystallites since they form the standard terminal $Na_{15}Sn_4$ intermetallics in all the sodiated samples. An amorphous structure per se would not produce such a capacity enhancement either: Sb50Ge50 and Sn80Ge10Sb10 also contain a large volume fraction of an amorphous phase, and yet show no excess capacity beyond the rule of mixtures prediction. We demonstrated that in Sn50Ge50 and in Sn50Ge25Sb25, the Ge nanocrystals contain solutionized Sn throughout cycling, with the lattice parameter of Ge being expanded far beyond the equilibrium. Conversely, in cycled Sn80Ge10Sb10 the Ge nanocrystals are absent, while in cycled Sb50Ge50 the Ge crystallites have a lattice parameter near the equilibrium value.

We therefore propose that the measured remarkable capacity enhancement in Sn50Ge50 and in the alloy-rich ternaries is due to the ability of Ge nanocrystallites alloyed with Sn to sodiate beyond the 1:1 Ge:Na (369 $mAhg^{-1}$) ratio previously reported for pure Ge electrodes. While a size-dependence of phase transitions is experimentally well-established for numerous other materials, [65-68] the lack of capacity enhancement in Sb50Ge50, or in the nanocolumnar pure Ge electrode employed in the previous study, [48] suggests that size alone will not drive Ge:Na far beyond 1:1. The equilibrium Ge-Na phase diagram contains an essentially pure Ge phase, a Ge_4Na intermetallic line compound, a GeNa intermatallic line compound, and a $GeNa_3$ intermatallic line compound whose crystal structure is not known. [29] The last phase, which should thermodynamically exist after full discharge, corresponds to a capacity of 1107 $mAhg^{-1}$. The fact that the capacity of pure Ge never approaches this value may be a kinetic limitation, normally associated with slow diffusion and/or insurmountable nucleation barriers during room temperature solid-state phase transformations. [69]

The cycling charge-discharge curves for the ternary alloys show well-defined voltage plateaus that have to be attributed to energetically distinct two-phase regions. However it is unlikely that the individual ~ 10 nm nanocrystallites are able to accommodate a phase boundary per se. Thus the two-phase voltage plateau may correspond to a crystallographic dependence of the individual crystallites fully transforming to their sodiated structure. In other words, at a given time the particles with the favorable surface crystal faces/directions will be fully sodiated, while the rest will be unsodiated. A nanocrystalline Ge precipitate with Sn in substitutional solid solution may allow for facile nucleation of one or several Na_xGe_y phases that are inaccessible in the pure state, even if is not possible to fully reach the 1:3 stoichiometry. Moreover the surrounding amorphous matrix may provide a fast ion diffusion path during

sodiation/desodiation, markedly accelerating the kinetics and thus allowing the system to adsorb/release more sodium for a given charge cycle. Such a dependence of the total reversible capacity on rate kinetics is known for hydrogen storage materials, where the same hydride but with an improved catalyst will actually store more hydrogen per sorption cycle. [70-72]

The absolute value of the reversible capacity of all the materials examined, as a function of cycle number, is shown in Figure 3.13(a). The capacity retention as a fraction of the initial value is shown in Figure 3.14(a), while the associated coulombic efficiencies are shown in Figure 3.14(b). Elemental Sn, Sb and Ge, along with the initially crystalline Sn80Ge10Sb10 alloy degrade by far the fastest. Conversely, the more alloyed systems Sn60Ge20Sb20, Sn50Ge25Sb25 and Sn33Ge33Sb33 all cycle fairly well. Table 3.3 shows the coulombic efficiency for all alloy electrodes after 1st and 50th cycles at 85 mAg^{-1}. For the case of Sn50Ge25Sb25 the coulombic efficiency remains close to 100 % during cycles 1-30, listed in Table 3.4, but begins to decrease afterward, approaching 90% at cycle 50. Such CE values are on par with values reported by others for Sn and Sb elemental and alloy thin films and for Ge films.[42,48,52] The cycling behavior of the Sn60Ge20Sb20 and Sn50Ge25Sb25 is analogous, with both alloys demonstrating similar initial and cycle 50 capacity. Likewise, the Sn33Ge33Sb33 alloy is stable, but has an overall lower specific capacity.

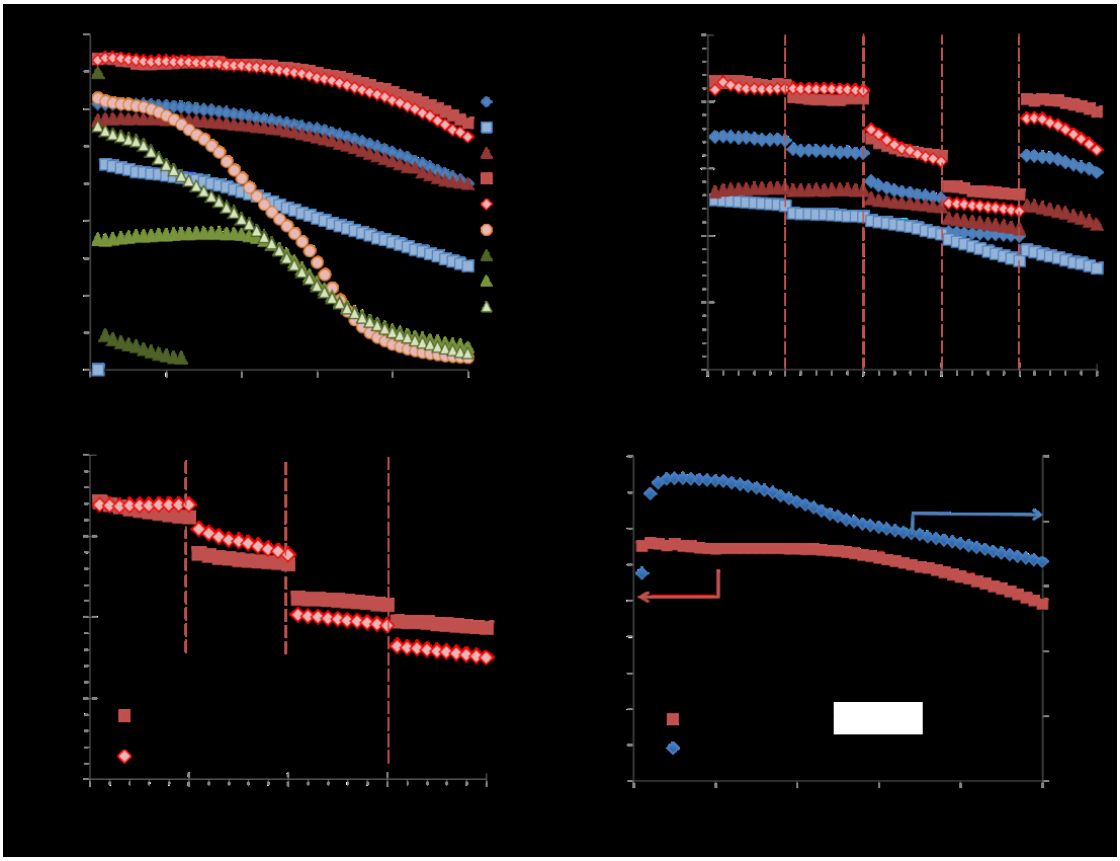

Figure 3.13: (a) Specific capacity *vs.*cycle number for all materials. Alloys were tested at same rates as data in Figure 3.8 and Figures 3.6. (b) – (c) Rate capability of binary and ternary alloys. Electrodes in (b) received 50 charge/discharge cycles (data shown in previous panel) prior to the sequential rate testing displayed, while electrodes in (c) were activated for only several cycles and then immediately ramped to 850 mAg^{-1}. (d) Specific capacity and coulombic efficiency *vs.* cycle number for Sn50Ge25Sb25 electrode cycled at 425 mAg^{-1} (~0.5C).

Table 3.3: Coulombic efficiency (CE) of all alloy thin films after 1st and 50th cycles at 85 mAg^{-1}.

Sample	Initial coulombic efficiency	Coulombic efficiency at 50th cycle
Sn50Ge50	0.6697	0.7722
Sb50Ge50	0.7698	0.7982
Sn33Ge33Sb33	0.6757	0.7612
Sn50Ge25Sb25	0.8369	0.9021
Sn60Ge20Sb20	0.7890	0.8323
Sn80Ge10Sb10	0.7000	-

Table 3.4: Coulombic efficiency of Sn50Ge25Sb25 thin film electrode for the first 30 cycles at 85 mAg^{-1}.

Cycle number	Coulombic efficiency
1	0.8369
2	0.9996
3	0.9988
4	0.9984
5	0.9989
6	0.9984
7	0.9979
8	0.9978
9	0.9987
10	0.9987
11	0.9977
12	0.9983
13	0.9977
14	0.9988
15	0.9979
16	0.9983
17	0.9985
18	0.9981
19	0.9989
20	0.9988
21	0.9979
22	0.9988
23	0.9988
24	0.9987
25	0.9981
26	0.9985
27	0.9988
28	0.9969
29	0.9961
30	0.9934

Electrode failure may be related to several mechanisms. Failure of sodiated Ge electrodes is not well-document in literature. However for the elemental systems such as Sn and Sb a common source of failure is the occurrence of repeated crystallization events. This leads to an anisotropic stress at two-phase boundaries, especially at the substrate/electrode interface. Of Ge, Sn and Sb elements, Sn is more likely to undergo such transitions. In addition, Sn has the largest

volume expansion, with ~ 425 % upon complete sodiation to $Na_{15}Sn_4$.[37] The related stresses would drive the delamination of the electrode from the support for a variety of current collector geometries.

Another contributor to loss of electrical contact is a potential chemical segregation induced weakening of the electrode - current collector interface. Authors recently reported calculations demonstrating that sodiation of pure Sn phases leads to elastic softening corresponding to a 75 % deterioration of the elastic moduli. [73] Moreover, for the case of lithium ion battery anodes, failure of similar "film-on-support" type architectures (Si on Cu) has been both experimentally and theoretically proven to be critically related to a weakening of the mutual interface, in turn due to Li segregation and a change in bonding. [74] The results shown in Figure 3.15 are the first direct experimental confirmation of this phenomenon in regard to sodiated (rather than lithiated) systems. Figure 3.15(a) shows a TOF-SIMS depth profile of Na and Fe concentration through the thickness of sodiated Sn50Ge25Sb25 alloy film on stainless steel substrate after the 2nd sodiation cycle. Clear Na segregation to the film - steel current collector interface is observed. The HAADF image and thickness-corrected EELS elemental line scan of Na in Sn50Ge25Sb25 after 2nd sodiation again clearly confirms these segregation phenomena (Figure 3.15(b)). Figure 3.15 also shows FIB cross-section SEM images of (c) pure Sn and (d) Sn50Ge25Sb25 alloy electrodes after 50 cycles. Both films show some delamination from the current collector, but with the case for pure Sn being substantially more severe. In fact according to the FIB image shown almost the entire pure Sn film is lifted off the current collector, with only the rightmost section in the image making electrical contact.

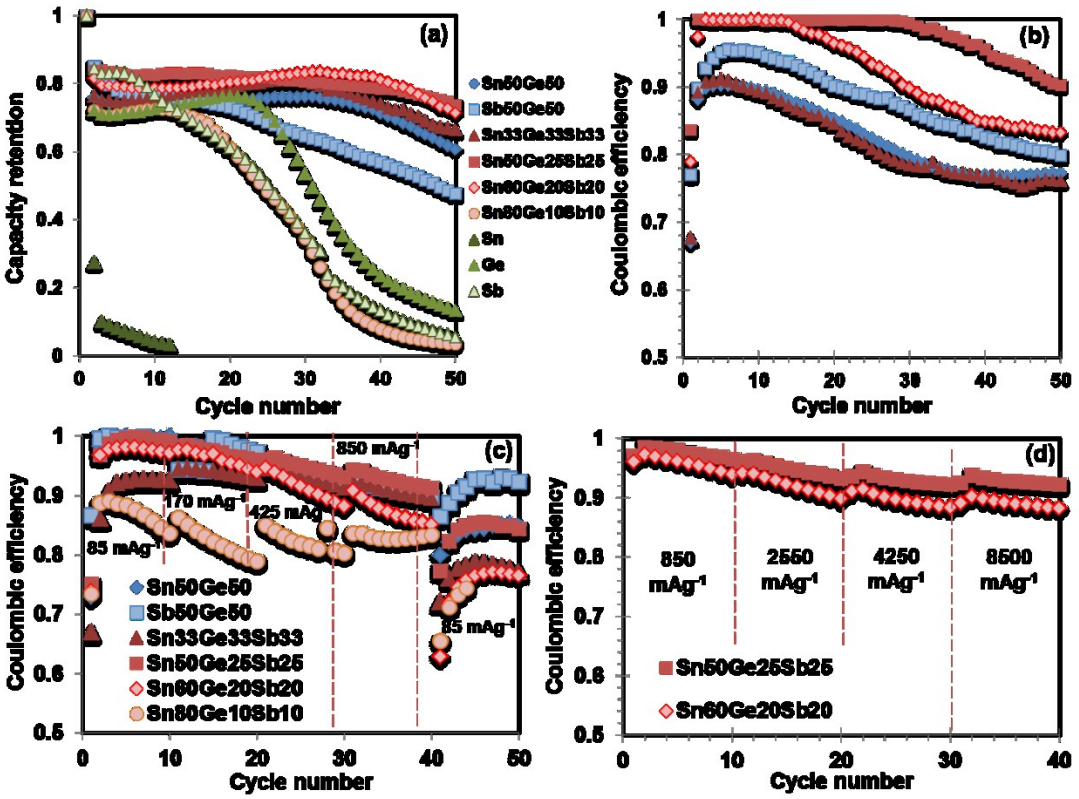

Figure 3.14: (a) Capacity retention as a fraction of the initial value and (b) coulombic efficiency as a function of cycle number for all materials. Figure 3.14 (c) and (d) coulombic efficiency associated with the rate capability results presented in Figure 3.13.

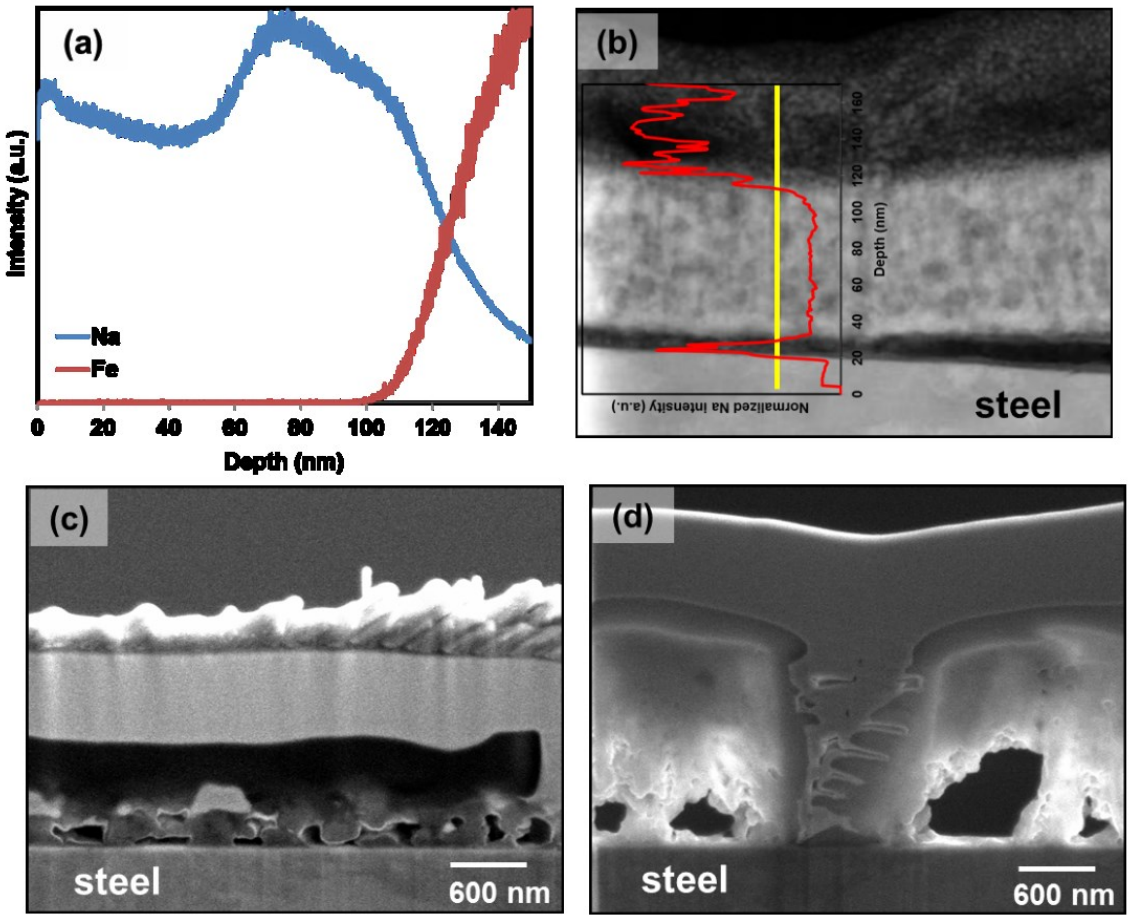

Figure 3.15: (a) TOF-SIMS depth profile of Na and Fe concentration through the thickness of sodiated Sn50Ge25Sb25 alloy film on stainless steel substrate after the 2nd sodiation. (b) HAADF image and thickness-corrected EELS elemental line scan of Na in Sn50Ge25Sb25 after 2nd sodiation. (c) and (d) FIB cross-section SEM images of (c) pure Sn and (d) Sn50Ge25Sb25 alloy electrodes after 50 cycles.

Upon sodiation the ternary alloys all undergo an expansion of roughly 300 – 400 %, depending on their total capacity. The alloys have the following approximate characteristics: Sn33Sb33Ge33: 103.3 g mol^{-1} atoms, max reversible capacity 669 $mAhg^{-1}$, 2.6 Na $atom^{-1}$; Sn50Sb25Ge25: 108.0 g mol^{-1} atoms, max reversible capacity 833 $mAhg^{-1}$, 3.4 Na $atom^{-1}$; Sn60Sb20Ge20: 110.1 g mol^{-1} atoms, max reversible capacity 829 $mAhg^{-1}$, 3.4 Na $atom^{-1}$; Sn80Sb10Ge10: 114.4 g mol^{-1} atoms, max reversible capacity 728 $mAhg^{-1}$, 3.1 Na $atom^{-1}$. From

a calculation based on the molar volume of each alloy and the molar volume of Na (23.78 cm^3mol^{-1}) the following expansion values are obtained: Sn33Sb33Ge33 - 280%; Sn50Sb25Ge25 - 380%; Sn60Sb20Ge20 - 380%; Sn80Sb10Ge10 - 340%. Thus, it can be concluded that the alloys with the highest capacity also undergo the largest expansion upon sodiation and that the cycling lifetime does not depends on minimizing the volume changes. This leads us to hypothesize that the heavily alloyed systems actually suffer less from Na-induced interfacial-softening tendency despite the fact that Na segregation still occurs. Classic metallurgical alloy design would rather attribute substitutional solid solution strengthening, an increased resistance to crystallization and a multiphase nanocomposite microstructure that gives both strength and ductility, leading to the observed increased resistance to interfacial delamination.

One successful way to improve the cycling stability of materials with exceptionally large sodiation/lithiation expansion is to form nanocomposites with lower-expansion materials such amorphous carbon, [38,75] empty space, [61-79] Cu,[37] or nano-scale films of Al and atomic-scale films of TiO_2 and TiN. [80-82] These either buffer the massive volume changes (carbon, empty space), or mechanically scaffold (Cu, Al, TiO_2, TiN) the primary active material, thus preventing its disintegration. For the case of the cyclically stable ternary Sn-Ge-Sb alloys, the amorphous matrix may accomplish a similar goal, surrounding the highly Na-active Sn-alloyed Ge and unalloyed Sn nanocrystallites, and mechanically preventing their loss of electrical contact with the current collector.

The electrolyte solvents used in studies of NIB anodes are generally the same as for LIB and in our case consisted of a mixture of EC and DEC. The operating potential of a NIB anode is slightly more positive than for LIB but still well below the onset potential of electrolyte

reduction for this type of cyclic carbonate compounds forming a so called solid electrolyte interphase (SEI) which is very similar for Na or Li electrolyte salts. [17] Since reduction of the solvent molecules to Na_2CO_3, Na alkyl carbonates and Na alkoxides consumes electrons irreversibly, this will reduce the coulombic efficiency. Indeed, the first cycle CE that we found was generally around 60-70%. Formation of an SEI layer will also increase the charge transfer resistance and thereby increase the overpotential [83-85] and reduce the capacity that can be extracted at a given current density. For materials that exhibit high expansion upon cycling, the SEI will fracture and expose fresh material to the electrolyte leading to build-up of an ever thicker surface layer. SEI accumulation in cracks or voids can lead to detachment of active material from the rest of the active mass and/or delamination from a substrate. [74,75,86] For thin films this problem is somewhat alleviated as expansion is confined to the direction perpendicular to the substrate. Indeed, we found CE close to 100% for Sn50Sb25Ge25 in cycle 2-30. However, expansion is so severe for NIB alloying anodes, up to a factor 5.2 for pure Sn and comparable expansion ratios were estimated based on our measured capacities, that beyond cycle 30 the CE and reversible capacity start to drop.

Modifications to the electrolyte have been highly successful in extending the lifetime of some high-expansion electrode materials. It has been shown that Si nanowires can be cycled thousands of times without significant degradation in electrolyte solvents that are highly resistant to reduction such as 1,3 dioxolane, despite 280% volume expansion. [87] Alternatively, addition of fluoro ethylene carbonate to conventional electrolyte mixtures has also been found to increase electrode lifetime [40-41,88] and modify the SEI layer. [89-90] Compared to standard carbonate mixtures, SEI formed from FEC is found to be very thin and contain large amounts of a polyene compound [83] that can passivate the electrode surface. High polymeric content would make the

SEI more elastic compared to one composed entirely of Li salts and less prone to fracture. This is especially important for materials that expand by extremely large amounts such as Sn and Sn-based alloys that we studied here. We would expect that the CE and cycling performance of our materials could be much improved by electrolyte modification.

Binary and ternary alloy electrodes were subjected to rate-capability tests with the results being shown in Figures 3.13(b) and 3.13(c). Capacity retention as a fraction of the measured capacities is plotted in Figure 3.14(a). Samples in Figures 3.13(b) received 50 charge/discharge cycles (shown in Figure 3.13(a)) prior to the rate testing, while alloys in 3.13(c) were activated at 85 mAg^{-1} for only several cycles and then rate tested. The degradation incurred in cycles 1-50 explains the capacity discrepancy at 850 mAg^{-1} between the two plots. Both Sn50Ge25Sb25 and Sn60Ge20Sb20 show excellent rate capability, with capacities of 381 $mAhg^{-1}$ and 313 $mAhg^{-1}$ being retained at a charge/discharge rate near 10C. As shown in Figure 3.13(d), Sn50Ge25Sb25 electrode revealed an initial reversible specific capacity of 653 $mAhg^{-1}$ and 491 $mAhg^{-1}$ after 50 charge - discharge cycles at 425 mAg^{-1}, indicting excellent cycling performance of this alloy at a relatively high cycling rate of ~0.5C.

The electrochemical impedance spectra (EIS) Nyquist plots of Sn50Ge25Sb25 alloy in as-synthesized state and after 50 cycles at 85 mAg^{-1} are shown in Figure 3.16. As indicated in Figure 3.16(b), cycled Sn50Ge25Sb25 has a low equivalent series resistance but that is generally on par with the elemental electrodes. This implies that the fast rate capability of the alloy is attributable to the facile phase transformation kinetics, rather than to an enhanced electrical conductivity of the material per se. It is instructive to compare the performance of the Sn-Ge-Sb electrodes with the best systems reported in scientific literature. Table 3.5 compares our results

with the state-of-the-art in previously published research on Sn-based NIB anode materials. It can be concluded that Sn50Ge25Sb25 and Sn60Ge20Sb20 electrodes exhibit one of the most promising capacity - rate capability combinations, with performance at 10C being especially desirable.

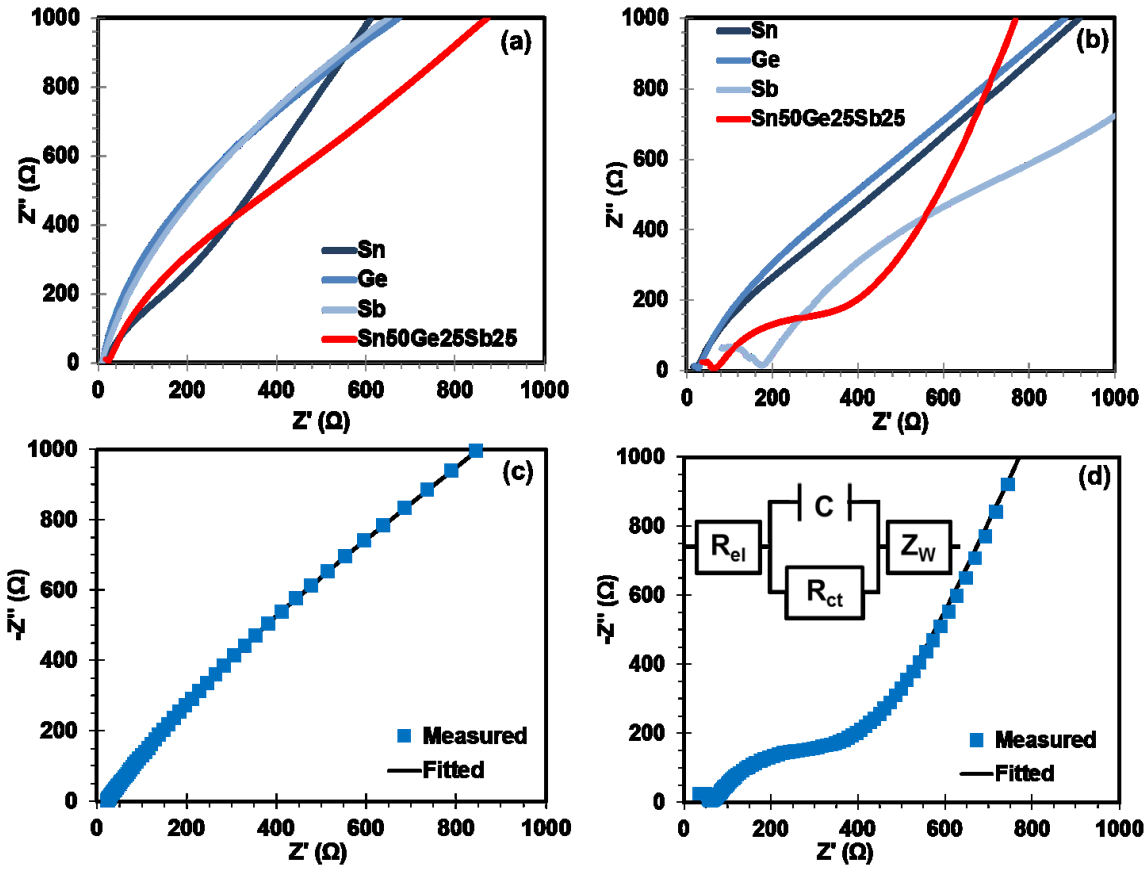

Figure 3.16: Impedance spectra of elemental and alloy Sn50Ge25Sb25 thin film electrodes in (a) as-made state and (b) cycled state after 50 cycles. Impedance spectra of Sn50Ge25Sb25 in (c) as-made state and (d) cycled state with corresponding simulation based on the equivalent circuit shown in insets.

Table 3.5: Comparison of our best-performing materials with previously published Sn-, Sb-, and Ge-based NIB anodes, as well as some carbon nanostructures, in terms of capacity and rate capability.

Electrodes	Cycling Capacity $mAhg^{-1}$ (current density)			Rate Capability $mAhg^{-1}$ (current density)	
	1st	10th	50th		
Sn50Ge25Sb25	*833*	*821*	*662*	*658*	*381*
Sn60Ge20Sb20	*829*	*826*	*625*	*675*	*313*
	(85 mAg^{-1})	*(85 mAg^{-1})*	*(85 mAg^{-1})*	*(850 mAg^{-1})*	*(8500 mAg^{-1})*
	(55 $mAcm^{-2}$)	*(55 $mAcm^{-2}$)*	*(55$mAcm^{-2}$)*	*(550 $mAcm^{-2}$)*	*(5500 $mAcm^{-2}$)*
	(0.1C)	*(0.1C)*	*(0.1C)*	*(1C)*	*(10C)*
Sn/C Nanocomposite[75]	470	270	N/A	N/A	N/A
	(50 mAg^{-1})	(50 mAg^{-1})			
Sn-Cu Nanocomposite[37]	~250	~420	~460	182	126
	(169 mAg^{-1})	(169 mAg^{-1})	(169 mAg^{-1})	(847 mAg^{-1})	(1694 mAg^{-1})
Sn-SnS-C Composite[38]	~430	~425	~450	~350	N/A
	(100 mAg^{-1})	(100 mAg^{-1})	(100 mAg^{-1})	(800 mAg^{-1})	
Sn-C Composite[38]	~240	~280	~220	~150	N/A
	(100 mAg^{-1})	(100 mAg^{-1})	(100 mAg^{-1})	(800 mAg^{-1})	
Nanocolumnar Germanium Thin Films[48]	~480	~470	~460	380	170
	(74 mAg^{-1})	(74 mAg^{-1})	(74 mAg^{-1})	(370 mAg^{-1})	(10000 mAg^{-1})
Sb/C Fibers[41]	~450	~400	~420	~300	~100

	(100 mAg^{-1})	(100 mAg^{-1})	(100 mAg^{-1})	(1000 mAg^{-1})	(6000 mAg^{-1})
Tin-Coated Viral Nanoforests[56]	~770 (50 mAg^{-1})	~580 (50 mAg^{-1})	~470 (50 mAg^{-1})	N/A	N/A
Sn Nanoparticles with Al_2O_3 Nanoglue [91]	~ 620 (N/A)	~ 680 (N/A)	N/A	N/A	N/A
Sn-film electrode in NaFSA KFSA[30]	~330 (0.6 $mAcm^{-2}$)	~300 (0.6$mAcm^{-2}$)	N/A	N/A	N/A
Mesoporous C/Sn Composite [5]	~300 (20 mAg^{-1})	~250 (20 mAg^{-1})	N/A	~70 (800 mAg^{-1})	~60 (1000 mAg^{-1})
Sn @ Wood Fibers[31]	~350 (84 mAg^{-1})	~220 (84 mAg^{-1})	~250 (84 mAg^{-1})	~75 (840 mAg^{-1})	N/A
SnSb/C Nanocomposite[4]	~570 (100 mAg^{-1})	~520 (100 mAg^{-1})	435 (100 mAg^{-1})	~280 (1000 mAg^{-1})	N/A
Hollow Carbon Nanowires[15]	251 (50 mAg^{-1})	~250 (50 mAg^{-1})	~240 (50 mAg^{-1})	149 (500 mAg^{-1})	N/A
Carbon Nanofibers[16]	~200 (200 mAg^{-1})	~180 (200 mAg^{-1})	175 (200 mAg^{-1})	~80 (500 mAg^{-1})	~60 (2000 mAg^{-1})
Sb-C Nanocomposite[40]	~610 (100 mAg^{-1})	~600 (100 mAg^{-1})	~600 (100 mAg^{-1})	~500 (1000 mAg^{-1})	~300 (2000 mAg^{-1})

Cu_2Sb Thin Films[44]	~280	~270	~50	~230	N/A
	(100 μAcm^{-2})	(100 μAcm^{-2})	(100 μAcm^{-2})	(100 μAcm^{-2})	
AlSb Thin Films[45]	~490	~350	~250	~100	N/A
	(40 μAcm^{-2})	(40 μAcm^{-2})	(40 μAcm^{-2})	(40 μAcm^{-2})	
Mo_3Sb_7 thin Films[46]	~330	~340	~300	~300	~110
	(0.6 $mAcm^{-2}$)	(0.6 $mAcm^{-2}$)	(0.6 $mAcm^{-2}$)	(0.6 $mAcm^{-2}$)	(18 $mAcm^{-2}$)
Sb/MWCNT Nanocomposite[47]	~ 500	~ 500	~ 450	~ 350	~ 250
	(100 mAg^{-1})	(100 mAg^{-1})	(100 mAg^{-1})	(1000 mAg^{-1})	(2000 mAg^{-1})
SnO_2@MWCNT Nanocomposite [92]	~500	~450	~380	~310	N/A
	(N/A)	(N/A)	(N/A)	(N/A)	
	(0.1C)	(0.1C)	(0.1C)	(0.5C)	
Sb_2O_4 Thin Films [93]	~980	~500	N/A	N/A	N/A
	(N/A)	(N/A)			
	(0.1C)	(0.1C)			
$Sn_{0.3}Co_{0.3}C_{0.4}$ Nanocomposite[34]	~400	~200	N/A	N/A	N/A
	(N/A)	(N/A)			
	(0.04C)	(0.04C)			
Porous Sb/Cu_2Sb anode[42]	~617	~600	~550	~470	~280
	(N/A)	(N/A)	(N/A)	(N/A)	(N/A)
	(0.1C)	(0.1C)	(0.1C)	(1C)	(5C)

SnO_2–RGO Nanocomposite [94]	407	~500	~400	~200	~120
	(100 mAg^{-1})	(100 mAg^{-1})	(100 mAg^{-1})	(500 mAg^{-1})	(1000 mAg^{-1})
Cu_6Sn_5 [36]	160	75	N/A	N/A	N/A
	(7.9 $mAcm^{-2}$)	(7.9$mAcm^{-2}$)			
$Sn_{25}Cu_{31}C_{44}$ [36]	135	120	117	N/A	N/A
	(0.1C)	(0.1C)	(0.1C)	N/A	N/A
$Sn_{39}Cu_{46}C_{15}$ [35]	350	330	160	465	337
	(0.1C)	(0.1C)	(0.1C)	(600 mAg^{-1})	(3000 mAg^{-1})
Sb-C nanofibers [95]	495	~500	~500	N/A	N/A
	(200 mAg^{-1})	(200 mAg^{-1})	(200 mAg^{-1})		
ALD-Al_2O_3 coated Sn nanoparticles [96]	625	650	N/A	N/A	N/A
	(N/A)	(N/A)			

Finally it is important to point out that while physical vapor co-deposition (co-sputtering) of alloy films represents a repeatable and compositionally accurate method for rapidly screening new materials, the microstructures discovered in this study are attainable through more "bulk" methods as well. High-energy mechanical alloying and rapid solidification are two well-known techniques for achieving a range of non-equilibrium microstructures that are in-practice stable during service. Co-milling is especially effective for the relatively soft metallic systems, such as those based on Sn or Sb, that undergo significant cold-welding and interdiffusion rather than pulverizing. For instance, metastable Ge-12at.% Sn [97] and 34at.% Ge [98] substitutional solid

solutions have already been synthesized by high-energy mechanical milling, though the authors did not employ the resultant structures for electrochemical purposes. Rapid solidification (melt spinning) has also been recently employed to produce metastable SnTe-Se thermoelectric alloys, [99] as well as Sn-Ge lithium ion battery anodes with exceptional charge storage capacities and cycling stability. [100] Neither co-milling nor rapid solidification methods suffer from practical engineering concerns of limited mass loadings or the need for planar geometries, and are therefore readily scalable to the desired battery application. In order to limit phase segregation in larger structures, a fourth element possessing a strong affinity for Sn, Sb and Ge may also be added. This was successfully achieved through the addition of S or Se into the non-equilibrium microstructures of Sn-Co-C nanocomposites, which were then sufficiently stable in bulk form as to be utilized for cycleable sodium ion battery anodes. [34]

3.4. References

1. Slater, M. D.; Kim, D.; Lee, E.; Johnson, C. S. Sodium Ion Batteries, *Adv. Funct. Mater.*, **2013**, 23, 947-958.
2. Ellis, B. L.; Nazar, L. F. Sodium and Sodium-Ion Energy Storage Batteries, *Curr. Opin. Solid St. Mater. Sci.*, **2012**, 16, 168-177.
3. Palomares, V.; Serras, P.; Villaluenga, I.; Hueso, K. B.; Carretero-Gonzalez, J.; Rojo, T. Na Ion Batteries, Recent Advances and Challenges to Become Low Cost Energy Storage Systems, *Energ. Environ. Sci.*, **2012**, 5, 5884-5901.
4. Xiao, L. F.; Cao, Y. L.; Xiao, J.; Wang, W.; Kovarik, L.; Nie, Z. M.; Liu, J. High Capacity, Reversible Alloying Reactions in SnSb/C Nanocomposites for Na-Ion Battery Applications, *Chem. Comm.*, **2012**, 48, 3321-3323.
5. Xu, Y. H.; Zhu, Y. J.; Liu, Y. H.; Wang, C. S. Electrochemical Performance of Porous Carbon/Tin Composite Anodes for Sodium-Ion and Lithium-Ion Batteries, *Adv. Energ. Mater.*, **2013**, 3, 128-133.

6. Kim, S. W.; Seo, D. H.; Ma, X. H.; Ceder G.; Kang, K. Electrode Materials for Rechargeable Sodium-Ion Batteries: Potential Alternatives to Current Lithium-Ion Batteries, *Adv. Energ. Mater.*, **2012**, 2, 710-721.

7. Palomares, V.; Casas-Cabanas, M.; Castillo-Martinez, E.; Han M. H.; Rojo, T. Update on Na-Based Battery Materials. A growing Research Path, *Energ. Environ. Sci.*, **2013**, 6, 2312-2337.

8. Chevrier, V. L.; Ceder, G. Challenges for Na-Ion Negative Electrodes, *J. Electrochem. Soc.*, **2011**, 158, A1011-A1014.

9. Pan, H. L.; Hu Y. S.; Chen, L. Q. Room-Temperature Stationary Sodium-Ion Batteries for Large-Scale Electric Energy Storage, *Energ. Environ. Sci*., **2013**, 6, 2338-2360.

10. Pourbaix, M. Atlas of Electrochemical Equilibria in Aqueous Solutions, National Association of Corrosion Engineers, **1974**.

11. Wibowo, R.; Aldous, L.; Jones, S. E. W.; Compton, R. G. The Electrode Potentials of the Group I Alkali Metals in The Ionic Liquid N-butyl-N-methylpyrrolidinium bis(trifluoromethylsulfonyl)imide. *Chem. Phys. Lett.* **2010**, 492, 276-280.

12. Ha, K-H.; Woo, S. H.; Mok, D.; Choi, N-S.; Park, Y.; Oh, S. M.; Kim, Y.; Kim, J.; Lee, J.; Nazar, L. F.; Lee, K. T. $Na_{4-\alpha}M_{2+\alpha/2}(P_2O_7)_2$ ($2/3 \leq \alpha \leq 7/8$, M = Fe, $Fe_{0.5}Mn_{0.5}$, Mn): A Promising Sodium Ion Cathode for Na-Ion Batteries, *Adv. Energ. Mater.*, **2013**, 3, 770-776.

13. Tripathi, R.; Gardiner, G. R.; Islam, M. S.; Nazar, L. F. Alkali-Ion Conduction Paths in $LiFeSO_4F$ and $NaFeSO_4F$ Tavorite-Type Cathode Materials, *Chem. Mater.*, **2011**, 23, 2278-2284.

14. Metrot, A.; Guerard, D.; Billaud, D.; Herold, A. New Results about The Sodium-Graphite System, *Synth. Met.*, **1979/80**, 1, 363.

15. Cao, Y.; Xiao, L.; Sushko, M. L.; Wang, W.; Schwenzer, B.; Xiao, J.; Nie, Z.; Saraf, L. V.; Yang, Z.; Liu, J. Sodium Ion Insertion in Hollow Carbon Nanowires for Battery Applications, *Nano Lett.* **2012**, 12, 3783.

16. Luo, W.; Schardt, J.; Bommier, C.; Wang, B.; Razink, J.; Simonsen, J.; Ji, X. Carbon Nanofibers Derived from Cellulose Nanofibers as a Long-Life Anode Material for Rechargeable Sodium-Ion Batteries, *J. Mat. Chem. A*, **2013**, 1, 10662.

17. Komaba, S.; Murata, W.; Ishikawa, T.; Yabuuchi, N.; Ozeki, T.; Nakayama, T.; Ogata, A.; Gotoh, K.; Fujiwara, K. Electrochemical Na Insertion and Solid Electrolyte Interphase for Hard-Carbon Electrodes and Application to Na-Ion Batteries, *Adv. Funct. Mater.* **2011**, 21, 3859.

18. Ding, J.; Wang, H.; Li, Z.; Kohandehghan, A.; Cui, K.; Xu, Z.; Zahiri, B.; Tan, X.; Memarzadeh, E.; Olsen, B. C.; Mitlin, D. Carbon Nanosheet Frameworks Derived from Peat Moss as High Performance Sodium Ion Battery Anodes, *ACS Nano* **2013**, in-press, DOI: 10.1021/nn404640c.

19. Shao, Y. Y.; Xiao, J.; Wang, W.; Engelhard, M.; Chen, X. L.; Nie, Z. M.; Gu, M.; Saraf, L. V.; Exarhos, G.; Zhang J. G.; Liu, J. Surface-Driven Sodium Ion Energy Storage in Nanocellular Carbon Foams, *Nano Lett.* 2013, 13, 3909-3914.

20. Ponrouch, A.; Goni, A. R.; Palacin, M. R. High Capacity Hard Carbon Anodes for Sodium Ion Batteries in Additive Free Electrolyte. *Electrochem. Commun*. **2013**, 27, 85-88.

21. Senguttuvan, P.; Rousse, G.; Seznec, V.; Tarascon, J. M.; Palacin, M. R. $Na_2Ti_3O_7$: Lowest Voltage Ever Reported Oxide Insertion Electrode for Sodium Ion Batteries. *Chem. Mater*. **2011**, 23, 4109-4111.

22. Zhao, L.; Pan, H. L.; Hu, Y. S.; Li, H.; Chen, L. Q. Spinel Lithium Titanate ($Li_4Ti_5O_{12}$) as Novel Anode Material for Room-temperature Sodium-ion Battery. *Chinese Phys. B.* **2012**, 21.

23. Pan, H. L.; Lu, X.; Yu, X. Q.; Hu, Y. S.; Li, H.; Yang, X. Q.; Chen, L. Q. Sodium Storage and Transport Properties in Layered Na2Ti3O7 for Room-Temperature Sodium-Ion Batteries. *Adv. Energ. Mater*. **2013**, 3, 1186-1194.

24. Rudola, A.; Saravanan, K.; Mason, C. W.; Balaya, P. $Na_2Ti_3O_7$: an Intercalation Based Anode for Sodium-ion Battery Applications. J. Mat. Chem. A **2013**, 1, 2653-2662.

25. Xu, Y.; Lotfabad, E. M.; Wang, H. L.; Farbod, B.; Xu, Z. W.; Kohandehghan, A.; Mitlin, D. Nanocrystalline Anatase TiO_2: a New Anode Material for Rechargeable Sodium Ion Batteries. Chem. Commun. **2013**, 49, 8973-8975.

26. Kim, K-T.; Ali. G.; Chung, K.Y.; Yoon, C.S.; Yashiro, H.; Sun, Y.K.; Sun, Y-K.; Lu, J.; Amine, K.; Myung, S-T. Anatase Titania Nanorods as an Intercalation Anode Material for Rechargeable Sodium Batteries, *Nano Lett.*, **2014**, 14, 2, 416–422.

27. Wu, L.; Buchholz, D.; Bresser, D.; Chagas, L.G.; Passerini, S. Anatase TiO_2 Nanoparticles for High Power Sodium-ion Anodes, J. Power Sources., **2014**, 251, 379–385.

28. Kim, H.; Jeong, G.; Kim, Y-U.; Kim, J-H.; Park, C-M.; Sohn, H-J. Metallic Anodes for Next Generation Secondary Batteries, *Chem. Soc. Rev.*, **2013**, 42, 9011-9034.

29. Okamoto, H. Desk Handbook of Phase Diagrams for Binary Alloys, ASM International, **2000**.

30. Yamamoto, T.; Nohira, T.; Hagiwara, R.; Fukunaga, A.; Sakai, S.; Nitta, K.; Inazawa, S. Charge-discharge Behavior of Tin Negative Electrode for a Sodium Secondary Battery Using Intermediate Temperature Ionic Liquid Sodium Bis(Fluorosulfonyl) Amide-Potassium Bis(fluorosulfonyl)amide, *J. Power Sources*, **2012**, 217, 479-484.

31. Zhu, H.L.; Jia, Z.; Chen, Y.C.; Weadock, N.; Wan, J.Y.; Vaaland, O.; Han, X.G.; Li, T.; Hu, L.B. Tin Anode for Sodium-Ion Batteries Using Natural Wood Fiber as a Mechanical Buffer and Electrolyte Reservoir, *Nano Lett.* **2013**, 13, 3093-3100.

32. Ellis, L. D.; Hatchard, T. D.; Obrovac, M. N. Reversible Insertion of Sodium in Tin, *J. Electrochem. Soc*. **2012**, 159, 11, A1801-A1805.

33. Baggetto, L.; Ganesh, P.; Meisner, R. P.; Unocic, R. R.; Jumas, J. C.; Bridges, C. A.; Veith, G. M. Characterization of Sodium Ion Electrochemical Reaction with Tin Anodes: Experiment and Theory. *J. Power Sources* **2013**, 234, 48-59.

34. Ellis, L. D.; Ferguson, P. P.; Obrovac, M. N. Sodium Insertion into Tin Cobalt Carbon Active/Inactive Nanocomposite, *J. Electrochem. Soc.*, **2013**, 160, A869-A872.

35. Thorne, J. S.; Dunlap, R. A.; Obrovac, M. N. $(Cu_6Sn_5)_{(1-x)}C_x$ Active/inactive Nanocomposite Negative Electrodes for Na-ion Batteries. *Electrochimica Acta* **2013**, 112, 133-137.

36. Baggetto, L.; Jumas, J.C.; Górka, J.; Bridges C.A.; Veith, G.M. Predictions of Particle Size and Lattice Diffusion Pathway Requirements for Sodium-ion Anodes Using η-Cu_6Sn_5 Thin Films as a Model System, Phys. *Chem. Chem. Phys.,* **2013**,15, 10885-10894.

37. Lin, Y.-M.; Abel, P. R.; Gupta, A.; Goodenough, J. B.; Heller, A.; Mullins, C. B. Sn-Cu Nanocomposite Anodes for Rechargeable Sodium-Ion Batteries, *ACS Appl. Mater. Interfaces*, **2013**, 5, 8273-8277.

38. Wu, L.; Hu, X. H.; Qian, J. F.; Pei, F.; Wu, F. Y.; Mao, R. J.; Ai, X. P.; Yang, H. X.; Cao, Y. L. A Sn-SnS-C Nanocomposite as Anode Host Materials for Na-Ion Batteries, *J. Mat. Chem. A*, **2013**, 1, 7181-7184.

39. Darwiche, A.; Marino, C.; Sougrati, M. T.; Fraisse, B.; Stievano, L.; Monconduit, L. Better Cycling Performances of Bulk Sb in Na-Ion Batteries Compared to Li-Ion Systems: An Unexpected Electrochemical Mechanism, *J. Am. Chem. Soc.*, **2012**, 134, 20805-20811.

40. Qian, J. F.; Chen, Y.; Wu, L.; Cao, Y. L.; Ai, X. P.; Yang, H. X. High Capacity Na-Storage and Superior Cyclability of Nanocomposite Sb/C Anode for Na-Ion Batteries, *Chem. Commun.* **2012**, 48, 7070-7072.

41. Zhu, Y. J.; Han, X. G.; Xu, Y. H.; Liu, Y. H.; Zheng, S. Y.; Xu, K.; Hu, L. B.; Wang, C. S. Electrospun Sb/C Fibers for a Stable and Fast Sodium-Ion Battery Anode, *ACS Nano*, **2013**, 7, 6378-6386.

42. Nam, D-H.; Hong, K-S.; Lim, S-J.; Kwon, H-S. Electrochemical Synthesis of a Three-Dimensional Porous Sb/Cu_2Sb Anode for Na-ion Batteries, *J. Power Sources*, **2014**, 247, 423-427.

43. Baggetto, L.; Ganesh, P.; Sun, C. N.; Meisner, R. A.; Zawodzinski, T. A.; Veith, G. M. Intrinsic Thermodynamic and Kinetic Properties of Sb Electrodes for Li-Ion and Na-Ion Batteries: experiment and theory, *J. Mat. Chem. A*, **2013**, 1, 7985-7994.

44. Baggetto, L.; Allcorn, E.; Manthiram A.; Veith, G. M. Cu_2Sb Thin Films as Anode for Na-Ion Batteries, *Electrochem. Commun*. **2013**, 27, 168-171.

45. Baggetto, L.; Marszewski, M.; Gorka, J.; Jaroniec, M.; Veith, G. M. AlSb Thin Films as Negative Electrodes for Li-Ion and Na-Ion Batteries, *J. Power Sources*, **2013**, 243, 699-705.

46. Baggetto, L.; Allcorn, E.; Unocic, R. R.; Manthiram A.; Veith, G. M. Mo_3Sb_7 as a Very Fast Anode Material for Lithium-Ion and Sodium-Ion Batteries, *J. Mat. Chem. A,* 2013, 1, 11163-11169.

47. Zhou, X.; Dai, Z.; Bao J.; Guo, Y. G. Wet Milled Synthesis of an Sb/MWCNT Nanocomposite for Improved Sodium Storage, *J. Mat. Chem. A,* **2013**, 1, 13727-13731.

48. Abel, P. R.; Lin, Y.-M.; de Souza, T.; Chou, C.-Y.; Gupta, A.; Goodenough, J. B.; Hwang, G. S.; Heller, A.; Mullins, C. B. Nanocolumnar Germanium Thin Films as a High-Rate Sodium-Ion Battery Anode Material, *J. Phys. Chem. C*, **2013**, 117, 18885-18890.

49. Baggetto, L.; Keum, J. K.; Browning J. F.; Veith, G. M. Germanium as Negative Electrode Material for Sodium-Ion Batteries, *Electrochem. Commun.* 2013, 34, 41-44.

50. Zhang, L.; Holt, C.M.B.; Luber, E.; Olsen, B.C.; Wang, H.; Danaie, M.; Cui, X.; Tan, X.; Lui, V.; Kalisvaart, W.P.; Mitlin, D. High Rate Electrochemical Capacitors from Three-Dimensional Arrays of Vanadium Nitride-Functionalized Carbon Nanotubes, *J. Phys. Chem. C* **2011**, 115, 24381–24393.

51. Nimisha, C. S.; Venkatesh, G.; Rao, K. Y.; Rao, G. M.; Munichandraiah, N. Morphology Dependent Electrochemical Performance of Sputter Deposited Sn Thin Films, *Materials Research Bulletin*, **2012**, 47, 1950-1953.

52. Dichi, E.; Wojakowska, A.; Legendre, B. Study of the Ternary System Germanium-Antimony-Tin: Experimental Phase Diagram, *J. Alloys Compd.*, **2001**, 320, 218-223.

53. Kim, B. G.; Bae, J.; Jeong, S.; Choi, S.; Lee, H. Crystallization Properties of $Ge_{1-x}Sb_x$ Thin Films (x=0.58-0.88). *Jpn. J. Appl. Phys.* **2011**, 50, 045805.

54. Chizmeshya, A. V. G.; Bauer, M. R.; Kouvetakis, J. Experimental and Theoretical Study of Deviations From Vegard's Law in The Sn_xGe_{1-x} System. *Chem. Mater.* **2003**, 15, 2511-2519.

55. Rao, F.; Song, Z. T.; Ren, K.; Li, X. L.; Wu, L. C.; Xi, W.; Liu, B. $Sn_{12}Sb_{88}$ Material For Phase Change Memory. *Appl. Phys. Lett.* **2009**, 95.

56. Liu, Y. H.; Xu, Y. H.; Zhu, Y. J.; Culver, J. N.; Lundgren, C. A.; Xu K.; Wang, C. S. Tin-Coated Viral Nanoforests as Sodium-Ion Battery Anodes, *ACS Nano* **2013**, 7, 3627-3634.

57. Wang, J. W.; Liu, X. H.; Mao, S. X.; Huang, J. Y. Microstructural Evolution of Tin Nanoparticles During in Situ Sodium Insertion and Extraction, *Nano Lett.* **2012**, 12, 5897-5902.

58. Wong, S. S.; He, G.; Nikzad, S.; Ahn, C. C.; Atwater, H. A. Local Order Measurement in SnGe Alloys and Monolayer Sn Films on Si with Reflection Electron Energy Loss Spectrometry, *J. Vac. Sci. Tech. A* **1995**, 13, 216-220.

59. Wang, Z. Y.; Wang, Z. C.; Wu, H. B.; Lou, X. W. Mesoporous Single- crystal CoSn(OH)(6) Hollow Structures with Multilevel Interiors. *Scientific Reports* **2013**, 3, 8.

60. Liu, J.; Qiao, S. Z.; Chen, J. S.; Lou, X. W.; Xing, X. R.; Lu, G. Q. Yolk/shell Nanoparticles: New Platforms for Nanoreactors, Drug Delivery and Lithium-ion Batteries. *Chem. Commun.* **2011**, 47, 12578-12591.

61. Song, H. W.; Li, N.; Cui, H.; Wen, X.; Wei, X. L.; Wang, C. X. Significantly Improved High-rate Li-ion Batteries Anode by Encapsulating Tin Dioxide Nanocrystals into Mesotunnels. *Cryst.Eng.Comm.* **2013**, 15, 8537-8543.

62. Hong, Y. J.; Son, M. Y.; Kang, Y. C. One-Pot Facile Synthesis of Double-Shelled SnO2 Yolk-Shell-Structured Powders by Continuous Process as Anode Materials for Li-ion Batteries. Adv. Mater. **2013**, 25, 2279-2283.

63. Ni, W.; Wang, Y. B.; Xu, R. Formation of Sn@C Yolk-Shell Nanospheres and Core-Sheath Nanowires for Highly Reversible Lithium Storage. *Part. Part. Syst. Charact.* **2013**, 30, 873-880.

64. Li, J. P.; Wu, P.; Ye, Y.; Wang, H.; Zhou, Y. M.; Tang, Y. W.; Lu, T. H. Designed Synthesis of SnO2@C Yolk-shell Spheres for High-performance Lithium Storage. *Cryst. Eng.comm.* **2014**, 16, 517-521.

65. Wagemaker, M.; Borghols, W. J. H.; Mulder, F. M. Large Impact of Particle Size on Insertion Reactions. A Case for Anatase Li_xTiO_2, *J. Am. Chem. Soc.*, **2007**, 129, 4323-4327.

66. Ichitsubo, T.; Doi, T.; Tokuda, K.; Matsubara, E.; Kida, T.; Kawaguchi, T.; Yagi, S.; Okada, S.; Amaki, J-I. What Determines the Critical Size for Phase Separation in $LiFePO_4$ in Lithium Ion Batteries?, *J. Mat. Chem. A*, **2013**, 1, 14532-14537.

67. Ma, Z.; Li, T.; Huang, Y. L.; Liu, J.; Zhou, Y.; Xue, D. Critical Silicon-Anode Size for Averting Lithiation-Induced Mechanical Failure of Lithium-Ion Batteries, *RSC Adv.*, **2013**, 3, 7398-7402.

68. Vermeulen, P.; Ledovskikh, A.; Danilov, D.; Notten, P. H. L. The Impact of the Layer Thickness on the Thermodynamic Properties of Pd Hydride Thin Film Electrodes, *J. Phys. Chem. B*, **2006**, 110, 20350-20353.

69. Porter, D. A.; Easterling, K. E.; Sherif M.Y. Phase Transformations in Metals and Alloys, Third Edition (Revised Reprint), CRC Press, **2009**.

70. Tan, X. H.; Harrower, C. T.; Amirkhiz B. S.; Mitlin, D. Nano-Scale Bi-Layer Pd/Ta, Pd/Nb, Pd/Ti and Pd/Fe Catalysts for Hydrogen Sorption in Magnesium Thin Films, *Int. J. Hydrogen Energy*, **2009**, 34, 7741-7748.

71. Zahiri, B.; Harrower, C.T.; Shalchi Amirkhiz, B.; Mitlin, D. Rapid and Reversible Hydrogen Sorption in Mg–Fe–Ti Thin Films, *Appl. Phys. Lett.* **2009**, 95, 103114-103114-3.

72. Zahiri, B.; Amirkhiz, B.S.; Mitlin, D. Hydrogen Storage Cycling of MgH2 Thin Film Nanocomposites Catalyzed By Bimetallic Cr-Ti, *Appl. Phys. Lett.*, 2010, 97, 083106-083106-3.

73. Mortazavi, M.; Deng, J. K.; Shenoy V. B.; Medhekar, N. V. Elastic Softening of Alloy Negative Electrodes for Na-Ion Batteries, *J. Power Sources*, **2013**, 225, 207-214.

74. Stournara M. E.; Xiao, X.; Qi, Y.;, Johari, P.; Lu, P.; Sheldon B. W., Gao, H.; Shenoy, V.B. Li Segregation Induces Structure and Strength Changes at the Amorphous Si/Cu Interface, *Nano Lett.* **2013**, 13, 4759−4768.

75. Datta, M. K.; Epur, R.; Saha, P.; Kadakia, K.; Park, S. K.; Kumta, P. N. Tin and Graphite Based Nanocomposites: Potential Anode For Sodium Ion Batteries, *J. Power Sources*, **2013**, 225, 316-322.

76. Karki, K.; Zhu, Y.; Liu, Y.; Sun, C.-F.; Hu, L.; Wang, Y.; Wang, C.; Cumings, J. Hoop-Strong Nanotubes for Battery Electrodes, *ACS Nano*, **2013**, 7, 8295–8302.

77. Song, T.; Cheng, H.; Choi, H.; Lee, J.-H.; Han, H.; Hyun Lee, D.; Su Yoo, D.; Kwon, M.-S.; Choi, J.-M..; Gwang Doo, S.; Chang, H.; Xiao, J.; Huang, Y.; Park, W. I.; Chung, Y.-C.; Kim, H.; Rogers, J. A.; Paik, U. Si/Ge Double-Layered Nanotube Array as a Lithium Ion Battery Anode, *ACS Nano*, **2012**, 6, 303–309.

78. Liu, N.; Wu, H.; McDowell, M. T.; Yao, Y.; Wang, C.; Cui, Y. A Yolk-Shell Design for Stabilized and Scalable Li-Ion Battery Alloy Anodes, Nano Lett. **2012**, 12, 3315−3321.

79. Yao, Y.; McDowell, M. T.; Ryu, I.; Wu, H.; Liu, N. A.; Hu, L. B.; Nix, W. D.; Choi, J. W.; Cui, Y. Interconnected Silicon Hollow Nanospheres for Lithium-Ion Battery Anodes with Long Cycle Life, *Nano Lett.*, **2011**, 11, 2949-2954.

80. Memarzadeh, E.; Kalisvaart, W. P.; Cui, K.; Kohandehghan, A.; Kupsta, M.; Olsen, B. C.; Mitlin, D. ALD TiO_2 Coated Silicon Nanowires for Lithium Ion Battery Anodes with Enhanced Cycling Stability and Coulombic Efficiency, *Phys. Chem. Chem. Phys.*, **2013**, 15, 13646-13657.

81. Kohandehghan, A.; Kalisvaart, W. P.; Cui, K.; Kupsta, M.; Memarzadeh, E.; Mitlin, D. Silicon Nanowire Lithium-Ion Battery Anodes with ALD Deposited TiN Coatings Demonstrate a Major Improvement in Cycling Performance, *J. Mater. Chem. A*, **2013**, 1, 12850-12861.

82. McDowell, M. T.; Lee, S. W.; Ryu, I.; Wu, H.; Nix, W. D.; Choi, J. W.; Cui, Y. Novel Size and Surface Oxide Effects in Silicon Nanowires as Lithium Battery Anodes, *Nano Lett.*, **2011**, 11, 4018-4025.

83. Aurbach, D.; Markovsky, B.; Levi, M. D.; Levi, E.; Schechter, A.; Moshkovich, M.; Cohen, Y. New Insights into the Interactions Between Electrode Materials and Electrolyte Solutions for Advanced Nonaqueous Batteries. *J. Power Sources* **1999**, 81, 95-111.

84. Aurbach, D. Review of Selected Electrode-solution Interactions which Determine the Performance of Li and Li Ion Batteries. *J. Power Sources* **2000**, 89, 206-218.

85. Levi, M. D.; Aurbach, D. Simultaneous Measurements and Modeling of the Electrochemical Impedance and the Cyclic Voltammetric Characteristics of Graphite Electrodes Doped with Lithium. *J. Phys. Chem. B* **1997**, 101, 4630-4640.

86. Kohandehghan, A.; Kalisvaart, P.; Kupsta, M.; Zahiri, B.; Amirkhiz, B. S.; Li, Z. P.; Memarzadeh, E. L.; Bendersky, L. A.; Mitlin, D. Magnesium and Magnesium-silicide Coated Silicon Nanowire Composite Anodes for Lithium-ion Batteries. *J. Mat. Chem. A* **2013**, 1, 1600-1612.

87. Etacheri, V.; Geiger, U.; Gofer, Y.; Roberts, G. A.; Stefan, I. C.; Fasching, R.; Aurbach, D. Exceptional Electrochemical Performance of Si-Nanowires in 1,3-Dioxolane Solutions: A Surface Chemical Investigation. *Langmuir* **2012**, 28, 6175-6184.

88. Oh, S. M.; Myung, S. T.; Jang, M. W.; Scrosati, B.; Hassoun, J.; Sun, Y. K. An Advanced Sodium-ion Rechargeable Battery Based on a Tin-carbon Anode and a Layered Oxide Framework Cathode. *Phys. Chem. Chem. Phys.* **2013**, 15, 3827-3833.

89. Nakai, H.; Kubota, T.; Kita, A.; Kawashima, A. Investigation of the Solid Electrolyte Interphase Formed by Fluoroethylene Carbonate on Si Electrodes. *J. Electrochem. Soc.* **2011**, 158, A798-A801.

90. Etacheri, V.; Haik, O.; Goffer, Y.; Roberts, G. A.; Stefan, I. C.; Fasching, R.; Aurbach, D. Effect of Fluoroethylene Carbonate (FEC) on the Performance and Surface Chemistry of Si-Nanowire Li-Ion Battery Anodes. *Langmuir* **2012**, 28, 965-976.

91. Han, X.; Liu, Y.; Jia, Z.; Chen, Y.-C.; Wan, J.; Weadock, N.; Gaskell, K.J.; Li, T.; Hu, L. Atomic-Layer-Deposition Oxide Nano-Glue for Sodium Ion Batteries, Nano let., 2014, 14, 139–147.

92. Wang, Y.; Su, D. W.; Wang, C. Y.; Wang, G. X. SnO2@MWCNT Nanocomposite as a High Capacity Anode Material for Sodium-Ion Batteries, *Electrochem. Commun.* 2013, 29, 8-11.

93. Sun, Q.; Ren, Q. Q.; Li H.; Fu, Z. W. High Capacity Sb2O4 Thin Film Electrodes for Rechargeable Sodium Battery, *Electrochem. Commun.* **2011**, 13, 1462-1464.

94. Wang, Y.-X.; Lim, Y.-G.; Park, M.-S.; Chou, S.-L.; Kim, J. H.; Liu, H.-K.; Dou, S.-X.; Kim, Y-J. Ultrafine SnO2 Nanoparticle Loading onto Reduced Graphene Oxide as Anodes for Sodium-Ion Batteries with Superior Rate and Cycling Performances, *J. Mat. Chem. A*, 2014, 2, 529–534.

95. Wu, L.; Hu, X. H.; Qian, J. F.; Pei, F.; Wu, F. Y.; Mao, R. J.; Ai, X. P.; Yang, H. X.; Cao, Y. L. Sb-C Nanofibers with Long Cycle Life as an Anode Material for High-performance Sodium-ion Batteries. *Energ. Environ. Sci.* **2014**, 7, 323-328.

96. Han, X. G.; Liu, Y.; Jia, Z.; Chen, Y. C.; Wan, J. Y.; Weadock, N.; Gaskell, K. J.; Li, T.; Hu, L. B. Atomic-Layer-Deposition Oxide Nanoglue for Sodium Ion Batteries. *Nano Lett.* **2014**, 14, 139-147.

97. Boolchand, P.; Koch, C. C. Moessbauer Spectroscopy Study of Nanoscale Ge-Sn Dispersions Prepared by Ball Milling, *J. Mat. Res.* **1992**, 7, 2876-2883.

98. Rebelo, Q. H. F.; Cotta, E. A.; de Souza, S. M.; Trichês, D. M.; Machado, K. D.; de Lima, J. C.; Grandi, T. A.; Poffo, C. M.; Manzato, L. Structural and Vibrational Investigations on $Ge_{34}Sb_{66}$ Solid Solutions Produced by Mechanical Alloying, *J. Alloy Compd.*, **2013**, 575, 80-85.

99. Tan, L.P.; Sun, T.; Fan, S.; Ramanujan, R.V.; Hng, H.H. Facile Precipitation of Two Phase Alloys in $SnTe_{0.75}Se_{0.25}$ with Improved Power Factor, *J. Alloy Compd,* **2014**, 587, 420-427.

100. Fan, S.F.; Lim, L.Y.; Tay, Y.Y.; Pramana, S.S.; Rui, X.H.; Samani, M.K.; Yan, Q.Y.; Tay, B.K.; Toney, M.F.; Hng, H.H. Rapid Fabrication of a Novel Sn-Ge Alloy: Structure-Property Relationship and its Enhanced Lithium Storage Properties, *J. Mat. Chem. A*, **2013**, 1, 14577-14585.

4. Conclusions

In this thesis the electrochemical performance of germanium nanowires (GeNWs) as anode for lithium-ion batteries (LIBs) and tin-germanium-antimony (Sn-Ge-Sb) thin films as anode for sodium-ion batteries (NIBs) have been investigated.

In order to find the optimum geometry and mass loading of GeNWs which offer the best electrochemical performance, we investigated diverse germanium nanowire arrays, in chapter 2, synthesized by VLS growth for 2, 5 and 10 minutes at 320°C or 360°C. We demonstrate a strong empirical correlation between the mass loading and the electrodes' electrochemical performance, which converged the 320°C and 360°C results into one relatively narrow band. There is a degradation of cycling capacity retention, coulombic efficiency and rate capability with higher mass loading and with coarser array geometry (mean nanowire diameter, mean thickness of the parasitic Ge films at the current collector - array interface). The inferior cycling capacity retention and CE is correlated with increasing levels of Li segregation to the current collector interface, and to preferential SEI formation and macroscopic cracking in that region. The inferior rate capability is likely caused by the longer Li diffusion distances associated with the larger diameters of the nanowires, and with the thicker Ge films at the bottom of the arrays. Our findings may serve as a useful design tool for fabricating high performance 1-D nanostructured anodes for Li ion storage applications.

Our study in chapter 3 reports the electrochemical charge/discharge cycling behavior Sn-Ge-Sb, Sn-Ge and Sb-Ge alloy thin films for the use as sodium ion battery anodes, testing pure Sn, Ge and Sb films as well. The measured reversibly capacities of Sn80Ge10Sb10,

Sn60Ge20Sb20, Sn50Ge25Sb25, and Sn33Ge33Sb33 are 728, 829, 833 and 669 $mAhg^{-1}$. With the exception of Sn80Ge10Sb10, these values are considerably above than the weighted average combination of the elemental capacities, which should be 800, 743, 714 and 664 $mAhg^{-1}$, respectively. Of all the compositions investigated, Sn50Ge25Sb25 demonstrates the best overall cycling performance, with 662 $mAhg^{-1}$ of capacity remaining after 50 cycles. The alloy also offers exquisite rate capability, delivering a stable cycling capacity of 658 and 381 $mAhg^{-1}$ at 850 and 8500 mAg^{-1}, respectively. We employ conventional TEM and HRTEM to investigate the materials' cycling microstructures, the optimum system being a composite of 10-15 nm Sn and Ge(Sn) crystals nanodispersed in an amorphous matrix. A hypothesis put fourth is that the capacity enhancement is due to the unique ability of Ge nanocrystallites that are heavily alloyed with Sn to sodiate beyond the 1:1 Ge:Na (369 $mAhg^{-1}$) ratio previously reported for pure Ge electrodes.

References

J. M. Tarascon, *Philosophical Transactions of the Royal Society a-Mathematical Physical and Engineering Sciences*, 2010, **368**, 3227.

M. Armand, J. M. Tarascon, *Nature,* 2008, **451**, 652.

M. M. Thackeray, C. Wolverton, E. D. Isaacs, *Energy & Environmental Science,* 2012, **5**, 7854.

V. Etacheri, R. Marom, R. Elazari, G. Salitra, D. Aurbach, *Energy & Environmental Science,* 2011, **4**, 3243.

J. B. Goodenough, *Accounts of Chemical Research,* 2013, **46**, 1053.

N.-S. Choi, Z. Chen, S. A. Freunberger, X. Ji, Y.-K. Sun, K. Amine, G. Yushin, L. F. Nazar, J. Cho, P. G. Bruce , *Angewandte Chemie International Edition,* 2012, **51**, 9994.

A. Patil, V. Patil, D. W. Shin, J.-W. Choi, D.-S. Paik, S.-J. Yoon, *Materials Research Bulletin,* 2008, **43**, 1913.

J. M. Tarascon, M. Armand, *Nature,* 2001, **414**, 359 .

M.R. Zamfir, H.T. Nguyen, E. Moyen,Y.H. Lee, D. Pribat, *Journal of Materials Chemistry A*, 2013, **1**, 9566.

B. Xu, D. Qian, Z. Wang, Y. S. Meng, *Materials Science and Engineering: R: Reports,* 2012, **73**, 51.

M. I. Hoffert, K. Caldeira, G. Benford, D. R. Criswell, C. Green, H. Herzog, A. K. Jain, H. S. Kheshgi, K. S. Lackner, J. S. Lewis, H. D. Lightfoot, W. Manheimer, J. C. Mankins, M. E Mauel, L. J. Perkins, M. E. Schlesinger, T. Volk, T. M. L. Wigley, *Science*, 2002, **298**, 981.

J. R. Szczech, S. Jin, *Energy & Environmental Science*, 2011, **4**, 56-72.

J.-M. Tarascon, M. Armand, *Nature*, 2001, **414**, 359-367.

M. Wakihara, O. Yamamoto, Wiley-VCH, Japan, 1998.

H. Takeshita, *Proceedings of the American Power Conference*, 2000, San Diego.

K. Caldeira, A. K. Jain, M. I. Hoffert, *Science,* 2003, **299**, 2052.

C. K. Chan, X. F. Zhang and Y. Cui, *Nano Letters*, 2008**, 8**, 307.

B. Laforge, L. Levan-Jodin, R. Salot and A. Billard, *Journal of the Electrochemical Society*, 2008, **155**, A181.

T. Song, J. L. Xia, J. H. Lee, D. H. Lee, M. S. Kwon, J. M. Choi, J. Wu, S. K. Doo, H. Chang, W. Il Park, D. S. Zang, H. Kim, Y. G. Huang, K. C. Hwang, J. A. Rogers and U. Paik, *Nano Letters*, 2010, **10**, 1710–1716.

W.J. Zhang, *Journal of Power Sources*, 2011, **196**, 877-885.

D. Linden, T.B. Reddy, *Handbook of Batteries;* 3 ed.; McGraw-Hill: New York, 2001.

W. H. Liu et al., "In Situ TEM Experiments of Electrochemical Lithiation and Delithiation of Individual Nanostructures", Advanced Energy Materials, 2012, **2**, 722–741.

J. Graetz, C. C. Ahn, R. Yazami and B. Fultz, *Journal of the Electrochemical Society*, 2004, **151**, A698.

S. Yoon, C. M. Park and H. J. Sohn, *Electrochemical and Solid State Letters*, 2008, **11**, A42.

X. H. Liu, S. Huang, S. T. Picraux, J. Li, T. Zhu and J. Y. Huang, *Nano Letters*, 2011, **11**, 3991.

L. P. Tan, Z. Y. Lu, H. T. Tan, J. X. Zhu, X. H. Rui, Q. Y. Yan and H. H. Hng, *Journal of Power Sources*, 2012, **206**, 253.

M. H. Park, Y. Cho, K. Kim, J. Kim, M. L. Liu and J. Cho, *Angewandte Chemie-International Edition*, 2011, **50**, 9647.

H. Adhikari, A. F. Marshall, C. E. D. Chidsey and P. C. McIntyre, *Nano Letters*, 2006, **6**, 318.

Y. D. Ko, J. G. Kang, G. H. Lee, J. G. Park, K. S. Park, Y. H. Jin and D. W. Kim, *Nanoscale*, 2011, **3**, 3371.

L. C. Yang, Q. S. Gao, L. Li, Y. Tang and Y. P. Wu, *Electrochemistry Communications*, 2010, **12**, 418-421.

M. H. Seo, M. Park, K. T. Lee, K. Kim, J. Kim and J. Cho, *Energy & Environmental Science*, 2011, **4**, 425.

R. A. DiLeo, S. Frisco, M. J. Ganter, R. E. Rogers, R. P. Raffaelle and B. J. Landi, *J. Phys. Chem. C*, 2011, **115**, 22609-22614.

J. S. Cheng and J. Du, *Crystengcomm*, 2012, **14**, 397.

Y. Hwa, C. M. Park, S. Yoon and H. J. Sohn, *Electrochimica Acta*, 2010, **55**, 3324-3329.

L. Baggetto, E. J. M. Hensen and P. H. L. Notten, *Electrochimica Acta*, 2010, **55**, 7074-7079.

S. Fang, L. Shen, P. Nie, G. Xu, J. Wang and X. Zhang, *Journal of Materials Science*, 2014, **49**, 2279.

L. Baggetto and P. H. L. Notten, *J. Electrochem. Soc.*, 2009, **156**, A169-A175.

R. Huang and J. Zhu, *Materials Chemistry and Physics*, 2010, **121**, 519.

E. L. Memarzadeh, W. P. Kalisvaart, A. Kohandehghan, B. Zahiri, C. M. B. Holt and D. Mitlin, *J. Mater. Chem.*, 2012, **22**, 6655-6668.

S. Misra, N. Liu, J. Nelson, S. S. Hong, Y. Cui and M. F. Toney, *Acs Nano*, 2012, **6**, 5465.

S. V. Thombare, A. F. Marshall and P. C. McIntyre, *Journal of Applied Physics*, 2012, **112**.

C. B. Li, K. Usami, H. Mizuta and S. Oda, *Journal of Applied Physics*, 2009, 106.

H. Adhikari, P. C. McIntyre, A. F. Marshall and C. E. D. Chidsey, *Journal of Applied Physics*, 2007, **102**.

M. Simanullang, K. Usami, T. Kodera, K. Uchida and S. Oda, *Japanese Journal of Applied Physics*, 2011, **50**.

S. Kodambaka, J. Tersoff, M. C. Reuter and F. M. Ross, *Science*, 2007, **316**, 729.

M. S. Song, J. H. Jung, Y. Kim, Y. Wang, J. Zou, H. J. Joyce, Q. Gao, H. H. Tan and C. Jagadish, *Nanotechnology*, 2008, **19**.

I. R. Musin and M. A. Filler, *Nano Letters*, 2012, **12**, 3363.

H. Adhikari, A. F. Marshall, I. A. Goldthorpe, C. E. D. Chidsey and P. C. McIntyre, *ACS Nano*, 2007, **1**, 415-422.

C. Renard, R. Boukhicha, C. Gardes, F. Fossard, V. Yam, L. Vincent, D. Bouchier, S. Hajjar, J. L. Bubendorff, G. Garreau and C. Pirri, *Thin Solid Films*, 2012, **520**, 3314-3318.

T. I. Kamins, X. Li and R. S. Williams, *Nano Letters*, 2004, **4**, 503.

M. D. Slater, D. Kim, E. Lee and C. S. Johnson, Advanced Functional Materials, 2013, **23**, 947-958.

B. L. Ellis and L. F. Nazar, Current Opinion in Solid State & Materials Science, 2012, **16**, 168-177.

V. Palomares, P. Serras, I. Villaluenga, K. B. Hueso, J. Carretero-Gonzalez and T. Rojo, Energy & Environmental Science, 2012, **5**, 5884-5901.

L. F. Xiao, Y. L. Cao, J. Xiao, W. Wang, L. Kovarik, Z. M. Nie and J. Liu, Chemical Communications, 2012, **48**, 3321-3323.

Y. H. Xu, Y. J. Zhu, Y. H. Liu, C. S. Wang, *Advanced Energy Materials*, 2013, **3**, 128-133.

S. W. Kim, D. H. Seo, X. H. Ma, G. Ceder and K. Kang, Advanced Energy Materials, 2012, **2**, 710-721.

V. Palomares, M. Casas-Cabanas, E. Castillo-Martinez, M. H. Han and T. Rojo, Energy & Environmental Science, 2013**, 6**, 2312-2337.

V. L. Chevrier and G. Ceder, Journal of the Electrochemical Society, 2011, **158**, A1011-A1014.

H. L. Pan, Y. S. Hu and L. Q. Chen, Energy & Environmental Science, 2013, **6,** 2338-2360.

Pourbaix, M. Atlas of Electrochemical Equilibria in Aqueous Solutions, National Association of Corrosion Engineers, 1974.

R. Wibowo, L. Aldous, S. E. W. Jones, R. G. Compton, Chemical Physical Letters, 2010, **492**, 276-280.

K-H. Ha, S. H. Woo, D. Mok, N-S. Choi, Y. Park, S. M. Oh, Y. Kim, J. Kim, J. Lee, L. F. Nazar, K. T. Lee, *Advanced Energy Materials*, 2013, **3**, 770-776.

R. Tripathi, G. R. Gardiner, M. S. Islam and L. F. Nazar, *Chemistry of Materials*, 2011, **23**, 2278-2284.

A. Metrot, D. Guerard, D. Billaud and A. Herold, *Synthetic Metals*, 1980, **1**, 363-369.

Y. L. Cao, L. F. Xiao, M. L. Sushko, W. Wang, B. Schwenzer, J. Xiao, Z. M. Nie, L. V. Saraf, Z. G. Yang and J. Liu, *Nano Letters*, 2012, **12**, 3783-3787.

W. Luo, J. Schardt, C. Bommier, B. Wang, J. Razink, J. Simonsen and X. L. Ji, *Journal of Materials Chemistry A*, 2013, **1**, 10662-10666.

S. Komaba, W. Murata, T. Ishikawa, N. Yabuuchi, T. Ozeki, T. Nakayama, A. Ogata, K. Gotoh and K. Fujiwara, *Advanced Functional Materials*, 2011, **21**, 3859-3867.

J. Ding, H. Wang, Z. Li, A. Kohandehghan, K. Cui, Z. Xu, B. Zahiri, X. Tan, E. M. Lotfabad, B. C. Olsen and D. Mitlin, *Acs Nano*, 2013, **7**, 11004.

Y. Y. Shao, J. Xiao, W. Wang, M. Engelhard, X. L. Chen, Z. M. Nie, M. Gu, L. V. Saraf, G. Exarhos, J. G. Zhang and J. Liu, *Nano Letters*, 2013, **13**, 3909-3914.

A. Ponrouch, A. R. Goni, M. R. Palacin, *Electrochemical Communication*, 2013, **27**, 85-88.

P. Senguttuvan, G. Rousse, V. Seznec, J. M. Tarascon, M. R. Palacin, *Chemistry of Materils,* 2011, **23**, 4109-4111.

L. Zhao, H. L. Pan, Y. S. Hu, H. Li, L. Q. Chen, *Chinese Physics B*., 2012, **21**, 028201.

H. L. Pan, X. Lu, X. Q. Yu, Y. S. Hu, H. Li, X. Q. Yang, L. Q. Chen, *Advanced Energy Materials*, 2013, **3**, 1186-1194.

A. Rudola, K. Saravanan, C. W. Mason, P. Balaya, *Journal of Materials Chemistry A*, 2013, **1**, 2653-2662.

Y. Xu, E. M. Lotfabad, H. L. Wang, B. Farbod, Xu, W. Z. A. Kohandehghan, D. Mitlin, *Chemical Communication*, 2013, **49**, 8973-8975.

K-T. Kim, G. Ali. K.Y. Chung, C.S. Yoon, H. Yashiro, Y.K. Sun, Y-K. Sun, J. Lu, K. Amine, S-T. Myung, *Nano Letters*, 2014, 14, **2**, 416–422.

L. Wu, D. Buchholz, D. Bresser, L.G. Chagas, S. Passerini, *Journal of Power Sources.*, 2014, **251**, 379–385.

H. Kim, G. Jeong, Y-U. Kim, J-H. Kim, C-M. Park, H-J. Sohn, *Chemical Society Reviews*, 2013,**42**, 9011-9034.

H. Okamoto, Desk Handbook "Phase Diagrams for Binary Alloys", *ASM International*, 2000.

T. Yamamoto, T. Nohira, R. Hagiwara, A. Fukunaga, S. Sakai, K. Nitta and S. Inazawa, *Journal of Power Sources*, 2012, **217**, 479-484.

H.L. Zhu, Z. Jia, Y.C. Chen, N. Weadock, J.Y. Wan, O. Vaaland, X.G. Han, T. Li, L.B. Hu, *Nano Letters*, 2013, **13**, 3093-3100.

L. D. Ellis, T. D. Hatchard, M. N. Obrovac, *Journal of Electrochemical Society*, 2012, **159**, A1801-A1805.

L. Baggetto, P. Ganesh, R.P. Meisner, R.R. Unocic, J.C. Jumas, C.A. Bridges, G.M. Veith, *Journal of Power Sources*, 2013, **234**, 48-59.

L. D. Ellis, P. P. Ferguson and M. N. Obrovac, *Journal of the Electrochemical Society*, 2013, **160**, A869-A872.

J. S. Thorne, R. A. Dunlap, M. N. Obrovac, *Electrochimica Acta*, 2013, **112**, 133-137.

L. Baggetto, J.C. Jumas, J. Górka, C.A. Bridges, G. M. Veith, *Physical Chemistry Chemical Physics*, 2013,**15**, 10885-10894.

Y.-M. Lin, P. R. Abel, A.Gupta, J. B. Goodenough, A. Heller, C. B. Mullins, *ACS Applied Materials Interfaces*, 2013, **5**, 8273-8277.

L. Wu, X. H. Hu, J. F. Qian, F. Pei, F. Y. Wu, R. J. Mao, X. P. Ai, H. X. Yang and Y. L. Cao, *Journal of Materials Chemistry A*, 2013, **1**, 7181-7184.

A. Darwiche, C. Marino, M. T. Sougrati, B. Fraisse, L. Stievano and L. Monconduit, *Journal of the American Chemical Society*, 2012, **134**, 20805-20811.

J. F. Qian, Y. Chen, L. Wu, Y. L. Cao, X. P. Ai and H. X. Yang, *Chemical Communications*, 2012, **48**, 7070-7072.

Y. J. Zhu, X. G. Han, Y. H. Xu, Y. H. Liu, S. Y. Zheng, K. Xu, L. B. Hu and C. S. Wang, *ACS Nano*, 2013, **7**, 6378-6386.

D-H. Nam, K-S. Hong, S-J. Lim, H-S. Kwon, *Journal of Power Sources*, 2014**, 247**, 423-427.

L. Baggetto, P. Ganesh, C. N. Sun, R. A. Meisner, T. A. Zawodzinski and G. M. Veith, *Journal of Materials Chemistry A*, 2013, **1**, 7985-7994.

L. Baggetto, E. Allcorn, A. Manthiram and G. M. Veith, *Electrochemistry Communications*, 2013, **27**, 168-171.

L. Baggetto, M. Marszewski, J. Gorka, M. Jaroniec and G. M. Veith, *Journal of Power Sources*, 2013, **243**, 699-705.

L. Baggetto, E. Allcorn, R. R. Unocic, A. Manthiram and G. M. Veith, *Journal of Materials Chemistry A*, 2013, **1**, 11163-11169.

X. Zhou, Z. Dai, X., J. Bao and Y. G. Guo, *Journal of Materials Chemistry A*, 2013, **1**, 13727-13731.

P. R. Abel, Y.-M. Lin, T. d. Souza, C.-Y. Chou, A. Gupta, J. B. Goodenough, G. S Hwang, A. Heller and C. B. Mullins, *Journal of Physical Chemistry C*, 2013, **117**, 18885-18890.

L. Baggetto, J. K. Keum, J. F. Browning and G. M. Veith, *Electrochemistry Communications*, 2013, **34**, 41-44.

B. Dunn, H. Kamath and J. M. Tarascon, *Science*, 2011, **334**, 928-935.

P. V. Braun, J. Cho, J. H. Pikul, W. P. King and H. G. Zhang, *Curr. Opin. Solid State Mater. Sci.*, 2012, **16**, 186-198.

N. Ding, J. Xu, Y. X. Yao, G. Wegner, X. Fang, C. H. Chen and I. Lieberwirth, *Solid State Ionics*, 2009, **180**, 222-225.

K. H. Seng, M.-h. Park, Z. P. Guo, H. K. Liu and J. Cho, *Nano Lett.*, 2013, **13**, 1230-1236.

M. I. Bodnarchuk, K. V. Kravchyk, F. Krumeich, S. Wang and M. V. Kovalenko, *ACS nano*, 2014, **8**, 2360-2368.

B. Liu, A. Abouimrane, M. Balasubramanian, Y. Ren and K. Amine, *J. Phys. Chem. C*, 2014, **118**, 3960-3967.

A. M. Chockla, K. C. Klavetter, C. B. Mullins and B. A. Korgel, *Acs Appl. Mater. & Interfaces*, 2012, **4**, 4658-4664.

C. S. Fuller and J. C. Severiens, *Phys. Rev.*, 1954, **96**, 21-24.

D. J. Xue, S. Xin, Y. Yan, K. C. Jiang, Y. X. Yin, Y. G. Guo and L. J. Wan, *J. Am. Chem. Soc.*, 2012, **134**, 2512-2515.

Y. J. Cho, H. S. Im, H. S. Kim, Y. Myung, S. H. Back, Y. R. Lim, C. S. Jung, D. M. Jang, J. Park, E. H. Cha, W. Il Cho, F. Shojaei and H. S. Kang, *Acs Nano*, 2013, **7**, 9075-9084.

Y.Yu, C.Yue, S. Sun, W. Lin, H. Su, B. Xu, J. Li, S. Wu, J. Li, and J. Kang, *ACS Appl. Mater. Interfaces*, 2014, **6(8)**, 5884-90.

C. K. Chan, H. L. Peng, G. Liu, K. McIlwrath, X. F. Zhang, R. A. Huggins and Y. Cui, *Nature Nanotech.*, 2008, **3**, 31-35.

A. H. Whitehead, K. Edstrom, N. Rao and J. R. Owen, *J. Power Sources*, 1996, **63**, 41-45.

N. G. Rudawski, B. L. Darby, B. R. Yates, K. S. Jones, R. G. Elliman and A. A. Volinsky, *Appl. Phys. Lett.*, 2012, **100**.

P. R. Abel, A. M. Chockla, Y.-M. Lin, V. C. Holmberg, J. T. Harris, B. A. Korgel, A. Heller and C. B. Mullins, *Acs Nano*, 2013, **7**, 2249-2257.

X. Liu, J. Zhao, J. Hao, B.-L. Su and Y. Li, *J. Mater. Chem. A*, 2013, **1**, 15076-15081.

Y. Son, M. Park, J. S. Lee, J. H. Jang, Y. Kim and J. Cho, *Nano Lett.*, 2014, **14**, 1005-1010.

T. Song, Y. Jeon, M. Samal, H. Han, H. Park, J. Ha, D. K. Yi, J.-M. Choi, H. Chang, Y.-M. Choi and U. Paik, *Energ. Environ. Sci.*, 2012, **5**, 9028-9033.

W. Li, Z. Yang, J. Cheng, X. Zhong, L. Gu, Y. Yu, *Nanoscale*, 2014, **6**, 4532.

W. Li, J. Zheng, T. Chen, T. Wang, X. Wang and X. Li, *Chem. Commun.*, 2014, **50**, 2052-2054.

C. Zhong, J.-Z. Wang, X.-W. Gao, D. Wexler and H.-K. Liu, *J. Mater. Chem. A*, 2013, **1**, 10798-10804.

J.-G. Ren, Q-H. Wu, H. Tang, G. Hong, W. Zhang, and S.-T. Lee*, J. Mater. Chem. A*, 2013, **1**, 1821.

S. Fan, L. Y. Lim, Y. Y. Tay, S. S. Pramana, X. Rui, M. K. Samani, Q. Yan, B. K. Tay, M. F. Toney and H. H. Hng, *J. Mater. Chem. A*, 2013, **1**, 14577-14585.

Y. J. Cho, C. H. Kim, H. S. Im, Y. Myung, H. S. Kim, S. H. Back, Y. R. Lim, C. S. Jung, D. M. Jang, J. Park, S. H. Lim, E. H. Cha, K. Y. Bae, M. S. Song and W. Il Cho, *Phys. Chem. Chem. Phys.*, 2013, **15**, 11691-11695.

T. Song, H. Cheng, K. Town, K. Park, R. W. Black, S. Lee, W. Park, Y. Huang, J. A. Rogers, L. F. Nazar, and U. Paik. *Adv. Funct. Mater.,* 2014, **24**, 1458–1464.

T. Kennedy, E. Mullane, H. Geaney, M. Osiak, C. O'Dwyer and K. M. Ryan, *Nano Lett.*, 2014, **14**, 716-723.

C. Wang, J. Ju, Y. Yang, Y. Tang, J. Lin, Z. Shi, R. P. S. Han and F. Huang, *J. Mater. Chem. A*, 2013, **1**, 8897-8902.

D. D. Vaughn and R. E. Schaak, *Chem. Soc. Rev.*, 2013, **42**, 2861-2879.

F. W. Yuan, H. J. Yang and H. Y. Tuan, *Acs Nano*, 2012, **6**, 9932-9942.

A. M. Chockla, M. G. Panthani, V. C. Holmberg, C. M. Hessel, D. K. Reid, T. D. Bogart, J. T. Harris, C. B. Mullins and B. A. Korgel, *J. Phys. Chem. C*, 2012, **116**, 11917-11923.

Y. Liu, S. Zhang and T. Zhu, *Chem.Electro. Chem.,* 2014*,* **1**, 817.

B. A. Korgel, *J. Phys. Chem. Lett.*, 2014, **5**, 749-750.

W. J. Zhang, *J. Power Sources*, 2011, **196**, 13-24.

D. Aurbach, B. Markovsky, G. Salitra, E. Markevich, Y. Talyossef, M. Koltypin, L. Nazar, B. Ellis and D. Kovacheva, *J. Power Sources*, 2007, **165**, 491-499.

Y. Matsumura, S. Wang and J. Mondori, *J. Electrochem. Soc.*, 1995, **142**, 2914-2918.

A. Kohandehghan, P. Kalisvaart, M. Kupsta, B. Zahiri, B. S. Amirkhiz, Z. P. Li, E. L. Memarzadeh, L. A. Bendersky and D. Mitlin, *J. Mater. Chem. A*, 2013, **1**, 1600-1612.

H. Wu, G. Chan, J. W. Choi, I. Ryu, Y. Yao, M. T. McDowell, S. W. Lee, A. Jackson, Y. Yang, L. B. Hu and Y. Cui, *Nature Nanotech.*, 2012, **7**, 309-314.

B. R. Long, J. L. Goldman, R. G. Nuzzo and A. A. Gewirth, *J. Solid State Electrochem.*, 2013, **17**, 3015-3020.

Y. Liu, X. H. Liu, B.-M. Nguyen, J. Yoo, J. P. Sullivan, S. T. Picraux, J. Y. Huang and S. A. Dayeh, *Nano Lett.*, 2013, **13**, 4876-4883.

X. H. Liu and J. Y. Huang, *Energ. Environ. Sci.*, 2011, **4**, 3844-3860.

X. H. Liu, H. Zheng, L. Zhong, S. Huan, K. Karki, L. Q. Zhang, Y. Liu, A. Kushima, W. T. Liang, J. W. Wang, J. H. Cho, E. Epstein, S. A. Dayeh, S. T. Picraux, T. Zhu, J. Li, J. P. Sullivan, J. Cumings, C. S. Wang, S. X. Mao, Z. Z. Ye, S. L. Zhang and J. Y. Huang, *Nano Lett.*, 2011, **11**, 3312-3318.

S. H. Woo, S. J. Choi, J. H. Park, W. S. Yoon, S. W. Hwang and D. Whang, *J. Electrochem. Soc.*, 2013, **160**, A112-A116.

Y. Yao, M. T. McDowell, I. Ryu, H. Wu, N. A. Liu, L. B. Hu, W. D. Nix and Y. Cui, *Nano Letters*, 2011, **11**, 2949-2954.

N. S. Choi, Y. Yao, Y. Cui and J. Cho, *Journal of Materials Chemistry*, 2011, **21**, 9825-9840.

J. H. Cho and S. T. Picraux, *Nano Lett.*, 2013, **13**, 5740-5747.

A. Rath, J. K. Dash, R. R. Juluri, A. Ghosh, T. Grieb, M. Schowalter, F. F. Krause, K. Muller, A. Rosenauer and P. V. Satyam, *Cryst. Eng. Comm*, 2014, **16**, 2486-2490.

J. L. Taraci, T. Clement, J. W. Dailey, J. Drucker and S. T. Picraux, *Nucl. Instrum. Methods Phys. Res., Sect. B -Beam Interactions with Materials and Atoms*, 2006, **242**, 205-208.

Y. Sierra-Sastre, S. A. Dayeh, S. T. Picraux and C. A. Batt, *Acs Nano*, 2010, **4**, 1209-1217.

M. E. Stournara, X. Xiao, Y. Qi, P. Johari, P. Lu, and B. W. Sheldon, *Nano Lett.*, 2013, **13**, 4759−4768.

D. Santhanagopalan, D. Qian, T. McGilvray, Z. Y. Wang, F. Wang, F. Camino, J. Graetz, N. Dudney and Y. S. Meng, *Journal of Physical Chemistry Letters*, 2014, **5**, 298.

J.-T. Li, J. Swiatowska, A. Seyeux, L. Huang, V. Maurice, S.-G. Sun and P. Marcus, *Journal of Power Sources*, 2010, **195**, 8251.

J.-T. Li, J. Swiatowska, V. Maurice, A. Seyeux, L. Huang, S.-G. Sun and P. Marcus, *Journal of Physical Chemistry C*, 2011, **115**, 7012.

B.Farbod, C. Kai, W. P. Kalisvaart, M. Kupsta, B. Zahiri, A. Kohandehghan, E. Memarzadeh, Z. Li, E. J. Luber, and D. Mitlin, ACS Nano, 2014, DOI: 10.1021/nn4063598.

L. Zhang, C. M. B. Holt, E. Luber, B. C. Olsen, H. Wang, M. Danaie, X. Cui, X. Tan, V. Lui, W. P. Kalisvaart, and D. Mitlin, *J. Phys. Chem. C,* 2011, **115**, 24381–24393.

C. O'Regan, S. Biswas, N. Petkov and J. D. Holmes, *J. Mater. Chem. C*, 2014, **2**, 14-33.

S. Kodambaka, J. Tersoff, M. C. Reuter and F. M. Ross, *Science*, 2007, **316**, 729-732.

J. B. Hannon, S. Kodambaka, F. M. Ross and R. M. Tromp, *Nature*, 2006, **440**, 69-71.

J. H. Kim, S. R. Moon, Y. Kim, Z. G. Chen, J. Zou, D. Y. Choi, H. J. Joyce, Q. Gao, H. H. Tan and C. Jagadish, *Nanotech.*, 2012, **23**.

J. Z. Wang, N. Du, H. Zhang, J. X. Yu and D. R. Yang, *J. Mater. Chem.*, 2012, **22**, 1511-1515.

E.L. Memarzadeh, P. Kalisvaart, K. Cui, A. Kohandehghan, M. Kupsta, B. Olsen, D. Mitlin, *Phys. Chem. Chem. Phys.*, 2013, p. **13646**.

A. Mukhopadhyay and B. W. Sheldon, *Progress in Mater. Sci.,* 2014, **63**, 58–116.

X. Su, Q. L. Wu, J. C. Li, X. C. Xiao, A. Lott, W. Q. Lu, B. W. Sheldon and J. Wu, *Adv. Energ. Mater.*, 2014, **4**.

X. H. Liu, L. Zhong, S. Huang, S. X. Mao, T. Zhu and J. Y. Huang, *Acs Nano*, 2012, **6**, 1522-1531.

H. Kim, M. Seo, M. H. Park and J. Cho, *Angewandte Chemie-International Edition*, 2010, **49**, 2146-2149.

M. T. McDowell, S. W. Lee, J. T. Harris, B. A. Korgel, C. M. Wang, W. D. Nix and Y. Cui, *Nano Lett.*, 2013, **13**, 758-764.

I. Ryu, J. W. Choi, Y. Cui and W. D. Nix, *J. Mech. Phys. Solids*, 2011, **59**, 1717-1730.

S. W. Lee, M. T. McDowell, L. A. Berla, W. D. Nix and Y. Cui, *Proceedings of the National Academy of Sciences of the United States of America*, 2012, **109**, 4080-4085.

X. Xiao, P. Liu, M. W. Verbrugge, H. Haftbaradaran and H. Gao, *J. Power Sources*, 2011, **196**, 1409-1416.

S. K. Soni, B. W. Sheldon, X. C. Xiao and A. Tokranov, *Scripta Materialia*, 2011, **64**, 307-310.

H. Haftbaradaran, X. C. Xiao, M. W. Verbrugge and H. J. Gao, *J. Power Sources*, 2012, **206**, 357-366.

H. Haftbaradaran and H. J. Gao, *Appl. Phys. Lett.*, 2012, **100**.

H. Haftbaradaran, X. C. Xiao and H. J. Gao, *Modell. Simul. Mater. Sci. Eng.*, 2013, **21**.

W. Liang, H. Yang, F. Fan, Y. Liu, X. H. Liu, J. Y. Huang, T. Zhu and S. Zhang, *Acs Nano*, 2013, **7**, 3427-3433.

E. M. Lotfabad, P. Kalisvaart, A. Kohandehghan, K. Cui, M. Kupsta, B. Farbod and D. Mitlin, *J. Mater. Chem. A*, 2014, **2**, 2504-2516.

A. Kohandehghan, P. Kalisvaart, K. Cui, M. Kupsta, E. Memarzadeh and D. Mitlin, *J. Mater. Chem. A*, 2013, **1**, 12850-12861.

C. M. Hwang and J. W. Park, *Thin Solid Films*, 2010, **518**, 6590-6597.

S. T. Boles, A. Sedlmayr, O. Kraft and R. Monig, *Appl. Phys. Lett.*, 2012, **100**.

T. T. Fister, J. L. Goldman, B. R. Long, R. G. Nuzzo, A. A. Gewirth and P. A. Fenter, *Appl. Phys. Lett.*, 2013, **102**.

S. P. V. Nadimpalli, V. A. Sethuraman, S. Dalavi, B. Lucht, M. J. Chon, V. B. Shenoy and P. R. Guduru, *J. Power Sources*, 2012, **215**, 145-151.

R. Deshpande, Y. T. Cheng and M. W. Verbrugge, *J. Power Sources*, 2010, **195**, 5081-5088.

M. D. Levi and D. Aurbach, J. *Phys. Chem. B*, 1997, **101**, 4630-4640.

V. Etacheri, U. Geiger, Y. Gofer, G. A. Roberts, I. C. Stefan, R. Fasching and D. Aurbach, *Langmuir*, 2012, **28**, 6175-6184.

E. Pollak, G. Salitra, V. Baranchugov and D. Aurbach, *J. Phys. Chem. C*, 2007, **111**, 11437-11444.

K. Xu, *Chem. Rev.*, 2004, **104**, 4303-4417.

J. C. Guo, A. Sun, X. L. Chen, C. S. Wang and A. Manivannan, *Electrochimica Acta*, 2011, **56**, 3981-3987.

N. Ding, J. Xu, Y. X. Yao, G. Wegner, I. Lieberwirth and C. H. Chen, *J. Power Sources*, 2009, **192**, 644-651.

B. Philippe, R. Dedryvère, M. Gorgoi, H. Rensmo, D. Gonbeau, and K. Edström. Chem. Mater., 2013, **25**, 394–404.

D. Aurbach, B. Markovsky, M. D. Levi, E. Levi, A. Schechter, M. Moshkovich and Y. Cohen, *J. Power Sources*, 1999, **81**, 95-111.

K. W. Schroder, H. Celio, L. J. Webb and K. J. Stevenson, *J. Phys. Chem. C*, 2012, **116**, 19737-19747.

D. Aurbach, E. Zinigrad, Y. Cohen and H. Teller, *Solid State Ionics*, 2002, **148**, 405-416.

M. E. Stournara, P. R. Guduru and V. B. Shenoy, *J. Power Sources*, 2012, **208**, 165-169.

V. B. Shenoy, P. Johari and Y. Qi, *J. Power Sources*, 2010, **195**, 6825-6830.

I-S. Hwang, J-C. Kim,b S-D. Seo, S. Lee, J-H. Lee and D-W. Kim, *Chem. Commun.,* 2012, 48, 7061–7063.

J. Zhang, Z. Xie, W. Li, S. Dong and M. Qu, *Carbon*, 2014, 74, 153.

Z. Wang, Y. Fu, Z. Zhang, S. Yuan, K. Amine, V. Battaglia and G. Liu, *Journal of Power Sources*, 2014, 260, 57.

D. Beneventi, D. Chaussy, D. Curtil, L. Zolin, E. Bruno, R. Bongiovanni, M. Destro, C. Gerbaldi, N. Penazzi and S. Tapin-Lingua, *Chemical Engineering Journal*, 2014, 243, 372.

L. Yao, X. Hou, S. Hua, X. Tang, X. Liu and Q. Ru, *Journal of Alloys and Compounds*, 2014, 585, 398.

Y. S. Park, E. S. Oh and S. M. Lee, *Journal of Power Sources*, 2014, 248, 1191.

Y. X. Lin, Z. H. Huang, X. L. Yu, W. C. Shen, Y. P. Zheng and F. Y. Kang, *Electrochimica Acta*, 2014, 116, 170.

A. P. Cohn, L. Oakes, R. Carter, S. Chatterjee, A. S. Westover, K. Share and C. L. Pint, *Nanoscale*, 2014, 6, 4669.

M. L. Lee, Y. H. Li, S. C. Liao, J. M. Chen, J. W. Yeh and H. C. Shih, *Electrochimica Acta*, 2013, 112, 529.

J. Yi, J. Key, F. Wang, Y. G. Wang, C. X. Wang and Y. Y. Xia, *Electrochimica Acta*, 2013, 106, 534.

L. Gan, H. J. Guo, Z. X. Wang, X. H. Li, W. J. Peng, J. X. Wang, S. L. Huang and M. R. Su, *Electrochimica Acta*, 2013, 104, 117.

B. B. Wu, T. Liu, Q. B. Xia and X. D. Wu, *Journal of the Electrochemical Society*, 2013, 160, A1720.

Pourbaix, M. Atlas of Electrochemical Equilibria in Aqueous Solutions, National Association of Corrosion Engineers, **1974**.

Metrot, A.; Guerard, D.; Billaud, D.; Herold, A., *Synth. Met.*, **1979/80**, 1, 363.

Ding, J.; Wang, H.; Li, Z.; Kohandehghan, A.; Cui, K.; Xu, Z.; Zahiri, B.; Tan, X.; Memarzadeh, E.; Olsen, B. C.; Mitlin, D., *ACS Nano* **2013***,* in-press, DOI: 10.1021/nn404640c.

Zhao, L.; Pan, H. L.; Hu, Y. S.; Li, H.; Chen, L. Q.. *Chinese Phys. B.* **2012**, 21.

Okamoto, H. Desk Handbook of Phase Diagrams for Binary Alloys, ASM International, **2000**.

Zhang, L.; Holt, C.M.B.; Luber, E.; Olsen, B.C.; Wang, H.; Danaie, M.; Cui, X.; Tan, X.; Lui, V.; Kalisvaart, W.P.; Mitlin, D., *J. Phys. Chem. C* **2011**, 115, 24381–24393.

Nimisha, C. S.; Venkatesh, G.; Rao, K. Y.; Rao, G. M.; Munichandraiah, N., *Materials Research Bulletin*, **2012**, 47, 1950-1953.

Dichi, E.; Wojakowska, A.; Legendre, B., *J. Alloys Compd.*, **2001**, 320, 218-223.

Kim, B. G.; Bae, J.; Jeong, S.; Choi, S.; Lee, H. *Jpn. J. Appl. Phys.* **2011**, 50, 045805.

Chizmeshya, A. V. G.; Bauer, M. R.; Kouvetakis, J. *Chem. Mater.* **2003**, 15, 2511-2519.

Rao, F.; Song, Z. T.; Ren, K.; Li, X. L.; Wu, L. C.; Xi, W.; Liu, B. *Appl. Phys. Lett.* **2009**, 95.

Liu, Y. H.; Xu, Y. H.; Zhu, Y. J.; Culver, J. N.; Lundgren, C. A.; Xu K.; Wang, C. S., *ACS Nano* **2013**, 7, 3627-3634.

Wang, J. W.; Liu, X. H.; Mao, S. X.; Huang, J. Y., *Nano Lett.* **2012**, 12, 5897-5902.

Wong, S. S.; He, G.; Nikzad, S.; Ahn, C. C.; Atwater, H. A., *J. Vac. Sci. Tech. A* **1995**, 13, 216-220.

Wang, Z. Y.; Wang, Z. C.; Wu, H. B.; Lou, X. W. *Scientific Reports* **2013**, 3, 8.

Liu, J.; Qiao, S. Z.; Chen, J. S.; Lou, X. W.; Xing, X. R.; Lu, G. Q. *Chem. Commun.* **2011**, 47, 12578-12591.

Song, H. W.; Li, N.; Cui, H.; Wen, X.; Wei, X. L.; Wang, C. X. *Cryst.Eng.Comm.* **2013**, 15, 8537-8543.

Hong, Y. J.; Son, M. Y.; Kang, Y. C. Adv. Mater. **2013**, 25, 2279-2283.

Ni, W.; Wang, Y. B.; Xu, R. *Part. Part. Syst. Charact.* **2013**, 30, 873-880.

Li, J. P.; Wu, P.; Ye, Y.; Wang, H.; Zhou, Y. M.; Tang, Y. W.; Lu, T. H. *Cryst. Eng.comm.* **2014**, 16, 517-521.

Wagemaker, M.; Borghols, W. J. H.; Mulder, F. M. *J. Am. Chem. Soc.*, **2007**, 129, 4323-4327.

Ichitsubo, T.; Doi, T.; Tokuda, K.; Matsubara, E.; Kida, T.; Kawaguchi, T.; Yagi, S.; Okada, S.; Amaki, J-I., *J. Mat. Chem. A*, **2013**, 1, 14532-14537.

Ma, Z.; Li, T.; Huang, Y. L.; Liu, J.; Zhou, Y.; Xue, D., *RSC Adv.*, **2013**, 3, 7398-7402.

Vermeulen, P.; Ledovskikh, A.; Danilov, D.; Notten, P. H. L., *J. Phys. Chem. B*, **2006**, 110, 20350-20353.

Porter, D. A.; Easterling, K. E.; Sherif M.Y. Phase Transformations in Metals and Alloys, Third Edition (Revised Reprint), CRC Press, **2009**.

Tan, X. H.; Harrower, C. T.; Amirkhiz B. S.; Mitlin, D., *Int. J. Hydrogen Energy*, **2009**, 34, 7741-7748.

Zahiri, B.; Harrower, C.T.; Shalchi Amirkhiz, B.; Mitlin, D., *Appl. Phys. Lett.* **2009**, 95, 103114-103114-3.

Zahiri, B.; Amirkhiz, B.S.; Mitlin, D., *Appl. Phys. Lett.*, 2010, 97, 083106-083106-3.

Mortazavi, M.; Deng, J. K.; Shenoy V. B.; Medhekar, N. V., *J. Power Sources*, **2013**, 225, 207-214.

Stournara M. E.; Xiao, X.; Qi, Y.;, Johari, P.; Lu, P.; Sheldon B. W., Gao, H.; Shenoy, V.B., *Nano Lett.* **2013**, 13, 4759−4768.

Datta, M. K.; Epur, R.; Saha, P.; Kadakia, K.; Park, S. K.; Kumta, P. N., *J. Power Sources*, **2013**, 225, 316-322.

Karki, K.; Zhu, Y.; Liu, Y.; Sun, C.-F.; Hu, L.; Wang, Y.; Wang, C.; Cumings, J., *ACS Nano*, **2013**, 7, 8295–8302.

Song, T.; Cheng, H.; Choi, H.; Lee, J.-H.; Han, H.; Hyun Lee, D.; Su Yoo, D.; Kwon, M.-S.; Choi, J.-M..; Gwang Doo, S.; Chang, H.; Xiao, J.; Huang, Y.; Park, W. I.; Chung, Y.-C.; Kim, H.; Rogers, J. A.; Paik, U., *ACS Nano*, **2012**, 6, 303–309.

Liu, N.; Wu, H.; McDowell, M. T.; Yao, Y.; Wang, C.; Cui, Y., Nano Lett. **2012**, 12, 3315−3321.

Yao, Y.; McDowell, M. T.; Ryu, I.; Wu, H.; Liu, N. A.; Hu, L. B.; Nix, W. D.; Choi, J. W.; Cui, Y., *Nano Lett.*, **2011**, 11, 2949-2954.

McDowell, M. T.; Lee, S. W.; Ryu, I.; Wu, H.; Nix, W. D.; Choi, J. W.; Cui, Y., *Nano Lett*., **2011**, 11, 4018-4025.

Aurbach, D.; Markovsky, B.; Levi, M. D.; Levi, E.; Schechter, A.; Moshkovich, M.; Cohen, Y.. *J. Power Sources* **1999**, 81, 95-111.

Aurbach, D.. *J. Power Sources* **2000**, 89, 206-218.

Levi, M. D.; Aurbach, D., *J. Phys. Chem. B* **1997**, 101, 4630-4640.

Kohandehghan, A.; Kalisvaart, P.; Kupsta, M.; Zahiri, B.; Amirkhiz, B. S.; Li, Z. P.; Memarzadeh, E. L.; Bendersky, L. A.; Mitlin, D., *J. Mat. Chem. A* **2013**, 1, 1600-1612.

Etacheri, V.; Geiger, U.; Gofer, Y.; Roberts, G. A.; Stefan, I. C.; Fasching, R.; Aurbach, D. *Langmuir* **2012**, 28, 6175-6184.

Oh, S. M.; Myung, S. T.; Jang, M. W.; Scrosati, B.; Hassoun, J.; Sun, Y. K.. *Phys. Chem. Chem. Phys.* **2013**, 15, 3827-3833.

Nakai, H.; Kubota, T.; Kita, A.; Kawashima, *J. Electrochem. Soc.* **2011**, 158, A798-A801.

Etacheri, V.; Haik, O.; Goffer, Y.; Roberts, G. A.; Stefan, I. C.; Fasching, R.; Aurbach, D. *Langmuir* **2012**, 28, 965-976.

Han, X.; Liu, Y.; Jia, Z.; Chen, Y.-C.; Wan, J.; Weadock, N.; Gaskell, K.J.; Li, T.; Hu, L., Nano let., 2014, 14, 139–147.

Wang, Y.; Su, D. W.; Wang, C. Y.; Wang, G. X., *Electrochem. Commun.* 2013, 29, 8-11.

Sun, Q.; Ren, Q. Q.; Li H.; Fu, Z. W., *Electrochem. Commun.* **2011**, 13, 1462-1464.

Wang, Y.-X.; Lim, Y.-G.; Park, M.-S.; Chou, S.-L.; Kim, J. H.; Liu, H.-K.; Dou, S.-X.; Kim, Y-J., *J. Mat. Chem*. *A*, 2014, 2, 529–534.

Wu, L.; Hu, X. H.; Qian, J. F.; Pei, F.; Wu, F. Y.; Mao, R. J.; Ai, X. P.; Yang, H. X.; Cao, Y. L., *Energ. Environ. Sci.* **2014**, 7, 323-328.

X. G. Han, Y. Liu, Z. Jia, Y. C. Chen, J. Y. Wan, N. Weadock, K. J. Gaskell, T. Li, L. B. Hu, *Nano Lett.* **2014**, 14, 139-147.

P. Boolchand, C. C. Koch, *J. Mat. Res.* **1992**, 7, 2876-2883.

Q. H. F. Rebelo, E. A. Cotta, S. M. de Souza, D. M. Trichês, K. D. Machado, J. C. de Lima, T. A. Grandi, C. M. Poffo, L. Manzato, *J. Alloy Compd.*, **2013**, 575, 80-85.

L.P. Tan, T. Sun, S. Fan, R.V. Ramanujan, H.H. Hng, *J. Alloy Compd,* **2014**, 587, 420-427.

S. F. Fan, L. Y. Lim, Y. Y. Tay, S. S. Pramana, X. H. Rui, M. K. Samani, Q. Y. Yan, B. K. Tay, M. F. Toney, H. H. Hng, *J. Mat. Chem. A*, **2013**, 1, 14577-14585.